

CONTRACT REPORT ARBRL-CR-00404

TWO DIMENSIONAL CONVECTIVE FLAMESPREADING
IN PACKED BEDS OF GRANULAR PROPELLANT

Prepared by

Paul Gough Associates, Inc
P. O. Box 1614
Portsmouth, NH 03801

July 1979



US ARMY ARMAMENT RESEARCH AND DEVELOPMENT COMMAND
BALLISTIC RESEARCH LABORATORY
ABERDEEN PROVING GROUND, MARYLAND

Approved for public release; distribution unlimited.

19970930 045

DTIC QUALITY INSPECTED 1

Destroy this report when it is no longer needed.
Do not return it to the originator.

Secondary distribution of this report by originating
or sponsoring activity is prohibited.

Additional copies of this report may be obtained
from the National Technical Information Service,
U.S. Department of Commerce, Springfield, Virginia
22161.

The findings in this report are not to be construed as
an official Department of the Army position, unless
so designated by other authorized documents.

*The use of trade names or manufacturers' names in this report
does not constitute indorsement of any commercial product.*

UNCLASSIFIED

SECURITY CLASSIFICATION OF THIS PAGE (When Data Entered)

REPORT DOCUMENTATION PAGE		READ INSTRUCTIONS BEFORE COMPLETING FORM
1. REPORT NUMBER CONTRACT REPORT ARBRL-CR-00404	2. GOVT ACCESSION NO.	3. RECIPIENT'S CATALOG NUMBER
4. TITLE (and Subtitle) Two Dimensional Convective Flamespreading in Packed Beds of Granular Propellant		5. TYPE OF REPORT & PERIOD COVERED Final Report November 1977 - February 1979
		6. PERFORMING ORG. REPORT NUMBER PGA-TR-79-1
7. AUTHOR(s) Paul S. Gough		8. CONTRACT OR GRANT NUMBER(s) DAAK11-78-C-0003
9. PERFORMING ORGANIZATION NAME AND ADDRESS Paul Gough Associates, Inc. P.O. Box 1614 Portsmouth, NH 03801		10. PROGRAM ELEMENT, PROJECT, TASK AREA & WORK UNIT NUMBERS RDT&E 1L161102AH43
11. CONTROLLING OFFICE NAME AND ADDRESS USA Armament Research and Development Command Ballistic Research Laboratory ATTN: DRDAR-BL Aberdeen Proving Ground, MD 21005		12. REPORT DATE JULY 1979
14. MONITORING AGENCY NAME & ADDRESS (If different from Controlling Office)		13. NUMBER OF PAGES 150
		15. SECURITY CLASS. (of this report) Unclassified
15a. DECLASSIFICATION/DOWNGRADING SCHEDULE		
16. DISTRIBUTION STATEMENT (of this Report) Approved for public release; distribution unlimited.		
17. DISTRIBUTION STATEMENT (of the abstract entered in Block 20, if different from Report)		
18. SUPPLEMENTARY NOTES		
19. KEY WORDS (Continue on reverse side if necessary and identify by block number) Interior Ballistics Solid Propellant Gun Two Phase Flow Flamespread Computer Code		
20. ABSTRACT (Continue on reverse side if necessary and identify by block number) A theoretical model is described for the digital simulation of flamespreading and pressure-wave propagation in axisymmetric, two dimensional propelling charges. The approach recognizes explicitly the presence of internal boundaries defined by jumps in porosity and allows for treatment of the influence of bag materials, liners, and additives on flamespreading. As one step toward the implementation of this model, a technique of numerical solution is presented for a geometrically complex region of two dimensional, two phase flow. Solutions are presented for three problems based on nominal data.		

Foreword

Contract DAAK11-78-C-0003 has consisted of three Tasks which have successively contributed to the formulation, development and documentation of an axisymmetric two dimensional model of flamespreading in granular charges of gun propellant. The findings of the first two tasks have been previously documented in interim reports.

The earlier findings have been consolidated herein so that the interim reports may now be regarded as obsolete.

Technical cognizance for the subject contract has been provided by Mr. A.W. Horst, Jr., U.S. Army Ballistic Research Laboratory, DRDAR-BLP.

Summary

We describe a theoretical model for the digital simulation of flame-spreading and pressure wave propagation in axisymmetric two dimensional propelling charges. Because longitudinal pressure waves are known to be strongly influenced by the distribution of ullage around the charge, we describe an approach which recognizes explicitly all internal boundaries defined by jumps in porosity. Likewise, the formulation of the analysis of the internal boundaries enables the explicit recognition of the influence on flamespreading of bag material, liners and additives.

An important milestone in respect to the numerical implementation of this model is the development of a technique of numerical solution for a geometrically complex region of two dimensional two phase flow. We present a solution technique based on an equipotential map of the physical domain onto a square and an update of the state variables by an explicit two step marching technique. A characteristic formulation of the equations is used at the boundaries.

Stable solutions are presented for three problems based on nominal data. All three problems recognize the hemispherical shape of the breech closure plug and the taper of the tube. The third problem considers the projectile to have a boattail which intrudes into the propelling charge.

TABLE of CONTENTS

	Page
Foreword	i
Summary	ii
Table of Contents	iii
List of Illustrations	iv
1.0 INTRODUCTION	1
1.1 Objectives and Scope of Present Study	1
1.2 Background	2
1.3 Summary of Approach and Findings	7
2.0 GOVERNING EQUATIONS	15
2.1 Systems of Balance Equations	16
2.1.1 Two Dimensional Two Phase Flow	16
2.1.2 Quasi-One-Dimensional Two Phase Flow	18
2.1.3 Two Dimensional Single Phase (Gas) Flow	19
2.1.4 Quasi-One-Dimensional Single Phase (Gas) Flow	19
2.1.5 Lumped Parameter Single Phase (Gas) Flow	20
2.2 Constitutive Laws	22
2.2.1 Equation of State of Gas	22
2.2.2 Granular Stress Law	22
2.2.3 Propellant Form Functions	23
2.2.4 Interphase Drag	24
2.2.5 Interphase Heat Transfer	26
2.2.6 Solid Phase Surface Temperature	26
2.2.7 Ignition and Combustion	27
2.2.8 Primer Stimulus	27
2.3 Initial and Boundary Conditions	28
2.3.1 Jump Conditions at a Discontinuity in Two Phase Flow	28
2.3.2 External Boundaries	31
2.3.3 Gas Permeable Internal Boundaries	32
2.3.4 Impermeable Internal Boundaries	32
2.4 Characteristic Analysis of Balance Equations	34
2.4.1 Formulation of Characteristic Analysis	34
2.4.2 Illustration: Homentropic Flow	37
2.4.3 Single Phase Two Dimensional Unsteady Flow	39
2.4.4 Two Phase Two Dimensional Unsteady Flow	46
3.0 TWO DIMENSIONAL CONVECTIVE FLAMESPREADING IN A CLOSED CHAMBER	55
3.1 Method of Integration	55
3.1.1 Coordinate Transformations	55
3.1.2 Integration at Interior Mesh Points	57
3.1.3 Integration at Boundary Points	58
3.1.4 Integration at Corner Points	59
3.1.5 Numerical Devices	60
3.2 Numerical Results	60
3.2.1 Discussion of Data Bases	61
3.2.2 Zero Intrusion Projectile with Reversible Granular Stress Law	65
3.2.3 Zero Intrusion Projectile with Irreversible Granular Stress Law	66
3.2.4 Long Intrusion Projectile	69
4.0 CONCLUDING REMARKS	71
References	137
Nomenclature	142

LIST OF ILLUSTRATIONS

<u>Figure</u>	<u>Title</u>	<u>Page</u>
1.2.1	Configuration of 5-inch/54 caliber case ammunition	3
1.2.2	Configuration of typical center core ignition bag charge	3
3.2.1.1	Initial mesh distributions for simulation of zero intrusion and long intrusion projectiles	73
3.2.2.1	Distribution of porosity at 0.2 msec in case of zero intrusion projectile with reversible granular stress law	74
3.2.2.2	Distribution of porosity at 0.4 msec in case of zero intrusion projectile with reversible granular stress law	75
3.2.2.3	Distribution of porosity at 1.0 msec in case of zero intrusion projectile with reversible granular stress law	76
3.2.2.4	Distribution of pressure at 0.2 msec in case of zero intrusion projectile with reversible granular stress law	77
3.2.2.5	Distribution of pressure at 0.4 msec in case of zero intrusion projectile with reversible granular stress law	78
3.2.2.6	Distribution of pressure at 1.0 msec in case of zero intrusion projectile with reversible granular stress law	79
3.2.2.7	Distribution of granular stress at 1.0 msec in case of zero intrusion projectile with reversible granular stress law	80
3.2.3.1	Distribution of porosity at 1.0 msec in case of zero intrusion projectile with irreversible granular stress law	81
3.2.3.2	Distribution of porosity at 1.3 msec in case of zero intrusion projectile with irreversible granular stress law	82
3.2.3.3	Distribution of pressure at 0.2 msec in case of zero intrusion projectile with irreversible granular stress law	83
3.2.3.4	Distribution of pressure at 0.4 msec in case of zero intrusion projectile with irreversible granular stress law	84
3.2.3.5	Distribution of pressure at 1.0 msec in case of zero intrusion projectile with irreversible granular stress law	85
3.2.3.6	Distribution of pressure at 1.3 msec in case of zero intrusion projectile with irreversible granular stress law	86
3.2.3.7	Distribution of solid phase surface temperature at 0.1 msec in case of zero intrusion projectile with irreversible granular stress law	87
3.2.3.8	Distribution of solid phase surface temperature at 0.2 msec in case of zero intrusion projectile with irreversible granular stress law	88
3.2.3.9	Distribution of solid phase surface temperature at 0.3 msec in case of zero intrusion projectile with irreversible granular stress law	89
3.2.3.10	Distribution of solid phase surface temperature at 0.4 msec in case of zero intrusion projectile with irreversible granular stress law	90
3.2.3.11	Distribution of solid phase surface temperature at 1.0 msec in case of zero intrusion projectile with irreversible granular stress law	91

3.2.3.12	Distribution of density of gas at 0.2 msec in case of zero intrusion projectile with irreversible granular stress law	92
3.2.3.13	Distribution of density of gas at 0.4 msec in case of zero intrusion projectile with irreversible granular stress law	93
3.2.3.14	Distribution of density of gas at 1.0 msec in case of zero intrusion projectile with irreversible granular stress law	94
3.2.3.15	Distribution of density of gas at 1.3 msec in case of zero intrusion projectile with irreversible granular stress law	95
3.2.3.16	Distribution of temperature of gas at 1.3 msec in case of zero intrusion projectile with irreversible granular stress law	96
3.2.3.17	Distribution of granular stress at 0.1 msec in case of zero intrusion projectile with irreversible granular stress law	97
3.2.3.18	Distribution of granular stress at 0.2 msec in case of zero intrusion projectile with irreversible granular stress law	98
3.2.3.19	Distribution of granular stress at 0.3 msec in case of zero intrusion projectile with irreversible granular stress law	99
3.2.3.20	Distribution of granular stress at 0.6 msec in case of zero intrusion projectile with irreversible granular stress law	100
3.2.3.21	Distribution of granular stress at 1.0 msec in case of zero intrusion projectile with irreversible granular stress law	101
3.2.3.22	Distribution of granular stress at 1.3 msec in case of zero intrusion projectile with irreversible granular stress law	102
3.2.3.23	Distribution of axial component of solid phase velocity at 0.6 msec in case of zero intrusion projectile with irreversible granular stress law	103
3.2.3.24	Distribution of axial component of solid phase velocity at 1.0 msec in case of zero intrusion projectile with irreversible granular stress law	104
3.2.3.25	Distribution of radial component of solid phase velocity at 0.6 msec in case of zero intrusion projectile with irreversible granular stress law	105
3.2.3.26	Distribution of radial component of solid phase velocity at 1.0 msec in case of zero intrusion projectile with irreversible granular stress law	106
3.2.3.27	Distribution of axial component of gas phase velocity at 0.6 msec in case of zero intrusion projectile with irreversible granular stress law	107
3.2.3.28	Distribution of axial component of gas phase velocity at 1.0 msec in case of zero intrusion projectile with irreversible granular stress law	108
3.2.3.29	Distribution of radial component of gas phase velocity at 0.2 msec in case of zero intrusion projectile with irreversible granular stress law	109
3.2.3.30	Distribution of radial component of gas phase velocity at 0.6 msec in case of zero intrusion projectile with irreversible granular stress law	110
3.2.3.31	Distribution of radial component of gas phase velocity at 1.0 msec in case of zero intrusion projectile with irreversible granular stress law	111
3.2.3.32	Distribution of radial component of gas phase velocity at 1.1 msec in case of zero intrusion projectile with irreversible granular stress law	112

3.2.3.33	Distribution of radial component of gas phase velocity at 1.3 msec in case of zero intrusion projectile with irreversible granular stress law	113
3.2.4.1	Distribution of porosity at 1.4 msec in case of long intrusion projectile	114
3.2.4.2	Distribution of pressure at 0.2 msec in case of long intrusion projectile	115
3.2.4.3	Distribution of pressure at 0.4 msec in case of long intrusion projectile	116
3.2.4.4	Distribution of pressure at 1.0 msec in case of long intrusion projectile	117
3.2.4.5	Distribution of pressure at 1.4 msec in case of long intrusion projectile	118
3.2.4.6	Distribution of density of gas at 1.4 msec in case of long intrusion projectile	119
3.2.4.7	Distribution of temperature of gas at 1.4 msec in case of long intrusion projectile	120
3.2.4.8	Distribution of solid phase surface temperature at 0.2 msec in case of long intrusion projectile	121
3.2.4.9	Distribution of solid phase surface temperature at 0.4 msec in case of long intrusion projectile	122
3.2.4.10	Distribution of solid phase surface temperature at 1.0 msec in case of long intrusion projectile	123
3.2.4.11	Distribution of solid phase surface temperature at 1.4 msec in case of long intrusion projectile	124
3.2.4.12	Distribution of granular stress at 0.3 msec in case of long intrusion projectile	125
3.2.4.13	Distribution of granular stress at 1.0 msec in case of long intrusion projectile	126
3.2.4.14	Distribution of granular stress at 1.3 msec in case of long intrusion projectile	127
3.2.4.15	Distribution of axial component of gas phase velocity at 0.6 msec in case of long intrusion projectile	128
3.2.4.16	Distribution of axial component of gas phase velocity at 1.0 msec in case of long intrusion projectile	129
3.2.4.17	Distribution of axial component of gas phase velocity at 1.4 msec in case of long intrusion projectile	130
3.2.4.18	Distribution of radial component of gas phase velocity at 0.6 msec in case of long intrusion projectile	131
3.2.4.19	Distribution of radial component of gas phase velocity at 1.0 msec in case of long intrusion projectile	132
3.2.4.20	Distribution of radial component of gas phase velocity at 1.4 msec in case of long intrusion projectile	133
3.2.4.21	Distribution of axial component of solid phase velocity at 1.0 msec in case of long intrusion projectile	134
3.2.4.22	Distribution of radial component of solid phase velocity at 1.0 msec in case of long intrusion projectile	135
4.1	Two Possible Mesh Distributions for 105mm Howitzer with XM622 Projectile.	136

1.0 INTRODUCTION

This report presents details of the formulation and partial development of a model of the macroscopic, two dimensional, two phase, unsteady, reacting flow occurring in a gun.

The objectives of our enquiry and the scope of the present study are described in section 1.1. In section 1.2 we provide some background information which coordinates the present study with previous work. Finally, in section 1.3 of this introduction, we summarize our approach and present findings.

1.1 Objectives and Scope of Present Study

We describe first of all, the goals of our research as a whole. Although the present document constitutes a final contract report, it is, in a sense, an interim report. For this reason we shall try to clarify, as much as possible, the extent to which the scope of the present study permits us to reach our overall goals and to identify those aspects of the model which are deferred for future study.

In the general area of interior ballistic phenomena in medium caliber guns we may identify three topics of importance to the charge designer. These are:

- (a) The central problem of classical interior ballistics¹; namely, to obtain a desired muzzle velocity within a specified pressure limitation. Of course, the designer must also take into account problems of systems compatibility and other constraints, but we are concerned here only with the problems which have some hydrodynamic content.
- (b) The minimization of tube erosion and of muzzle blast.
- (c) The elimination of ignition anomalies which appear, in their mildest form, as longitudinal pressure waves and, in their worst form, as catastrophic overpressures of the gun.

It is this last problem which is addressed by our enquiry as a whole. Of particular interest are the important roles played by the detailed distribution of ullage, the igniter discharge characteristics and the flow inhibition due to the presence of bag materials together with the liners and additives used to control erosion and wear.

The scope of the present study is as follows. We provide the details of a model of the macroscopic, two dimensional, two phase unsteady reacting flow in a gun. The discussion includes details of the governing equations and the method of solution. Numerical solutions are generated for the problem of two dimensional convective flamespreading in a packed bed of granular propellant in an ullage free, but geometrically complex, container with stationary impermeable walls.

In its present state of numerical implementation, the model is therefore useful for the investigation of flamespreading in ullage-free case ammunition in which the projectile intrusion due to the boattail or afterbody

¹. Corner, J "Theory of the Interior Ballistics of Guns"
New York, John Wiley and Son, Inc.

may be significant. However, the application of the model to bag charges, for which ullage is present, and to the sequence of events following the start of the motion of the projectile, is the subject of future work.

1.2 Background

The ideal propelling charge is thought to be one in which ignition occurs simultaneously at all points so that all exposed surfaces are burning uniformly from the initial instant. A limiting form of this ideal involves the instantaneous combustion of the entire charge. From a theoretical point of view, the hydrodynamical model of such an interior ballistic cycle involves the study of a single phase substance expanding from a quiescent but energetic initial state. Such was the problem considered by Lagrange and later, in greater detail, by Pidduck and Kent¹.

From a practical point of view, however, a charge which burns instantaneously is one which subjects the tube to a certain level of stress while propelling the projectile at much lower average value. Accordingly, charges are designed to release their energy gradually, producing gas at a rate which compensates for the motion of the projectile. In this fashion system "cost" which is related to the maximum stress is better aligned with system "effectiveness" which is related to the average stress. An obvious theoretical consequence of this procedure is that a properly posed model of interior ballistic phenomena must now consider the coupled motion of both the gas and solid phases. By treating the motion as that of a well stirred mixture subjected to an independently determined pressure gradient to represent the response to projectile motion, one may establish a lumped parameter model of interior ballistic phenomena².

In fact, the mixture is far from well stirred except possibly quite late in the interior ballistic cycle as burnout is approached. Since many modern charges produce burning almost throughout the entire propulsion event, the assumption of well stirredness is rather limiting.

In order to understand the lack of equilibrium between the phases we refer to figures 1.2.1 and 1.2.2 which respectively illustrate a typical cased ammunition charge and a typical bag charge. It is apparent that inhomogeneity exists in the combustion chamber from the initial instant due to the presence of spaces around the charge. These spaces are referred to as ullage. Then, when the igniter begins to function, further inhomogeneities arise as the charge is not ignited uniformly. Rather, a spreading process occurs which involves a front referred to as a convective flame. Hot pressurized gas penetrates the charge, an aggregate of regularly formed grains. The penetration is accompanied by intense convective heat transfer which ignites the charge, and also by momentum transfer which accelerates the charge. Because of the impermeability of the charge, the pressures at two stations in the chamber may differ by tens of MPa during flamespreading.

It should be noted that the ignition system depends inherently on a principle of inhomogeneous venting since the heat transfer rates associated with

². Baer, P.G. and Frankle, J.M. "The Simulation of Interior Ballistics Performance of Guns by Digital Computer Program" BRL Report 1183 1962
AD 299980

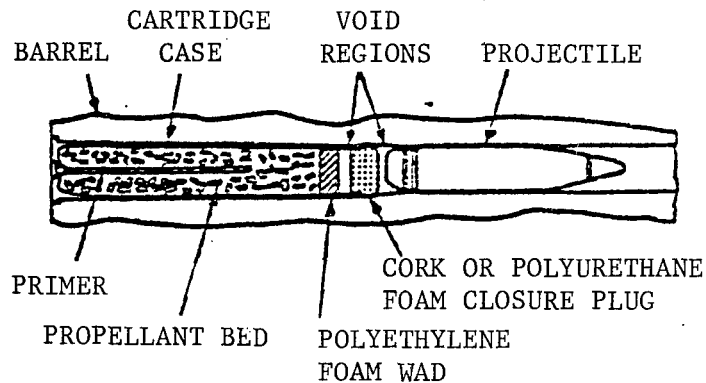


Figure 1.2.1 Configuration of 5 inch/54 caliber case ammunition

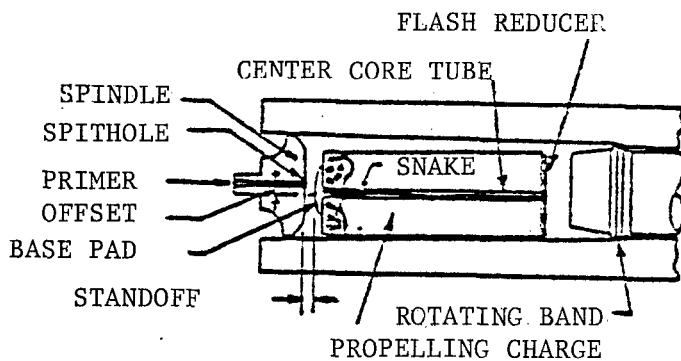


Figure 1.2.2 Configuration of typical center core ignition bag charge

linear conduction and radiation are several orders of magnitude less than those associated with convection. Yet, the pressure gradients associated with inhomogeneous venting can produce pronounced wave phenomena which are superimposed upon the ideal pressurization history. Significantly, the existence of longitudinal pressure waves has been correlated in many cases with weapon malfunction due to overpressurization³. Therefore, the ignition train is frequently designed so that, as shown in figures 1.2.1 and 1.2.2, venting occurs as close to simultaneously as possible over the length of the center line. The inhomogeneity is therefore concentrated in the radial direction and the tendency to produce longitudinal waves is minimized.

The importance of igniter location and of the distribution of ullage has been known since the time of Kent⁴ and of Hedden & Nance⁵. Kent showed, in the context of bag charges, that ullage around the charge was most influential in reducing the overall longitudinal pressure gradient during flame-spreading. This is easy to understand since the ullage around the charge provides a low impedance path for the flow of gas from the high pressure sections to the low pressure sections. Hedden and Nance demonstrated the strong influence exerted by longitudinal ullage on wave amplitude. More recently, several papers have appeared in which the dependence of the pressure wave amplitude on primer/propellant interface^{6,7}, charge permeability^{8,9} and charge configuration or ullage distribution^{9,10} has been explored.

-
3. Budka, A.J. and Knapton, J.D. "Pressure Wave Generation in Gun Systems - A Survey" BRL Memorandum Report 2567, AD B008893L 1975
 4. Kent, R.H. "Study of Ignition of 155-mm Gun" BRL Report 22, AD 494703 1935
 5. Hedden, S.E. and Nance, G.A. "An Experimental Study of Pressure Waves in Gun Chambers" NPG Report 1534 1957
 6. Horst, A.W., Jr. and Smith, T.C. "The Influence of Propelling Charge Configuration on Gun Environment Pressure - Time Anomalies" Proc. 12th Jannaf Combustion Meeting 1975
 7. May, I.W., Clarke, E.V. and Hassmann, H. "A Case History: Gun Ignition Related Problems and Solutions for the XM-198 Howitzer" BRL Interim Memorandum Report 150 1973
 8. Rocchio, J., Ruth, C. and May, I. "Grain Geometry Effects on Wave Dynamics in Large Caliber Guns" Proc. 13th Jannaf Combustion Meeting 1976
 9. Horst, A.W., Smith, T.C. and Mitchell, S.E. "Key Design Parameters in Controlling Gun - Environment Pressure Wave Phenomena - Theory versus Experiment" Proc. 13th Jannaf Combustion Meeting 1976
 10. Horst, A.W., Jr. and Gough, P.S. "Influence of Propellant Packaging on Performance of Navy Case Gun Ammunition" J. Ballistics v.1 No.3 1977

More or less concurrently with these experimental studies, the modeling of interior ballistic phenomena according to an unsteady, two-phase, continuum approach has been developed to the point of being able, in certain cases, to predict the structure and amplitude of the longitudinal pressure waves. While relatively limited flamespreading models were advanced by several authors¹¹⁻¹⁴, the models of Gough¹⁴⁻¹⁸ and of Fisher¹⁹⁻²² have reflected increasing attention to the detailed configuration of the charge.

The NOVA code developed by Gough¹⁴⁻¹⁸ effects a quasi-one-dimensional representation of the charge with precise attention to the axial distribution of ullage. This code has shown good correlation with observations of case ammunition^{9,10,16} as well as with certain simpler configurations¹⁶. The CALSPAN code developed by Fisher¹⁹⁻²² goes beyond the NOVA code in terms of phenomenological completeness. A two dimensional capacity exists, although the code is customarily run as a quasi-two-dimensional model in which one dimensional flow is considered in three concentric ducts corresponding to the center core igniter, the main charge and the external ullage. In spite of the greater completeness of modeling of the configuration of the bag charge, in

-
11. East, J.L. and McClure, D.R. "Projectile Motion Predicted by a Solid/Gas Flow Interior Ballistic Model" Proc. 10th Janna Combustion Meeting 1973
 12. Krier, H., Van Tassel, W.F., Rajan, S. and Vershaw, J. "Model of Flame Spreading and Combustion Through Packed Beds of Propellant Grains" Tech. Rept. AAE74-1, University of Illinois at Urbana-Champaign 1974
 13. Kuo, K.K., Koo, J.H., Davis, T.R. and Coates, G.R. "Transient Combustion in Mobile, Gas-Permeable Propellants" Acta Astron. v.3, No.7-8 pp.574-591 1976
 14. Gough, P.S. and Zwarts, F.J. "Theoretical Model for Ignition of Gun Propellant" Final Report, Part II, Contract N00174-72-C-0223 1972
 15. Gough, P.S. "Fundamental Investigation of the Interior Ballistics of Guns" Final Report, Contract N00174-73-C-0501 1974
 16. Gough, P.S. "The Flow of a Compressible Gas Through an Aggregate of Mobile, Reacting Particles" Ph.D. Thesis McGill University 1974
 17. Gough, P.S. "Computer Modelling of Interior Ballistics" Final Report Contract N00174-75-C-0131 1975
 18. Gough, P.S. "Numerical Analysis of a Two-Phase Flow with Explicit Internal Boundaries" Final Report Contract N00174-75-C-0259 1977
 19. Fisher, E.B. and Graves, K.W. "Mathematical Model of Double Base Propellant Ignition and Combustion in the 81mm Mortar" CAL Report No. DG-3029-D-1 1972
 20. Fisher, E.B. and Trippe, A.P. "Mathematical Model of Center Core Ignition in the 175mm Gun" Calspan Report No. VQ-5163-D-2 1974
 21. Fisher, E.B. "Propellant Ignition and Combustion in the 105mm Howitzer" Calspan Report No. VQ-5524-D-1 1975
 22. Fisher, E.B. and Trippe, A.P. "Development of a Basis for Acceptance of Continuously Produced Propellant" Calspan Report No. VQ-5163-D-1 1973

the CALSPAN code, the NOVA code has been shown to agree better with a standard 155mm center core configuration²³. However, neither code has successfully been able to predict the anomalous behaviour of a high zone base ignited 155mm charge except by ad hoc manipulation of the data base²⁴ or by assuming grain fracture due to impact of the charge on the base of the projectile²⁵.

In order to determine the extent to which the quasi-one-dimensional assumption fundamental to the NOVA code might limit its predictive capacity with respect to bag charges, we recently performed a limited theoretical study²⁶. By modifying the code to accept coupled one dimensional models of the base ignited bag charge and the external ullage we found that a completely different flamespreading path could be produced from that predicted by the one dimensional code in its usual form. Primer gas, produced in the breech, can initiate flamespreading in the rear portion of the charge and, by flowing around the bag, initiate a flame at the front so that the charge is ignited by two flame sheets.

Thus it was concluded that predictions of flamespreading in bag charges may be seriously in error unless careful attention is paid to the precise distribution of all ullage. It was also noted that, depending on its permeability, the bag material may play an extremely influential role in respect to flamespreading. Naturally, the history of the longitudinal pressure wave cannot be predicted unless the flamespreading path is accurately captured.

We may summarize the situation thus. The behaviour and amplitude of longitudinal pressure waves are of interest because of their correlation with catastrophic charge malfunction and also because they are believed to be correlated with performance variability²⁷. Factors known to influence the wave structure are the igniter venting characteristics, the permeability and progressivity of the charge and the detailed distribution of axial and radial ullage. It is also thought that the bag material and liners may be influential. One dimensional modeling has been quite successful in respect to the performance of case charges but is demonstrably deficient in respect to bag charges.

Accordingly, the prediction of pressure wave structure in bag charges requires at least a quasi-two-dimensional approach with careful attention given to the ullage distribution and the influence of the bag and liner. The

²³. Nelson, C. "Comparison of Predictions of Three Two-Phase Flow Codes"
BRL Memorandum Report 2729, AD 037348 1977

²⁴. Horst, A., Nelson, C. and May, I. "Flame Spreading in Granular Propellant Beds: A Diagnostic Comparison of Theory to Experiment"
Proc. AIAA/SAE 13th Joint Propulsion Conference 1977

²⁵. Horst, A.W., May, I.W. and Clarke, E.V., Jr. "The Missing Link Between Pressure Waves and Breechblows"
Proc. 14th Jannaf Combustion Meeting 1977

²⁶. Gough, P.S. "Theoretical Study of Two-Phase Flow Associated with Granular Bag Charges" Final Report, Contract DAAK11-77-C-0028 1978

²⁷. Clarke, E.V., Jr. and May, I.W. "Subtle Effects of Low-Amplitude Pressure Wave Dynamics on the Ballistic Performance of Guns"
Proc. 11th Jannaf Combustion Meeting 1974

CALSPAN model does admit a quasi-two-dimensional formulation. However, the radial expansion of the bed due to the center core igniter blast is not considered and the influence of the bag is neglected. We regard these as serious physical omissions. In addition, the numerical analysis contained in the CALSPAN code is based on a highly diffusive, and therefore inaccurate scheme. Finally, the axial distribution of ullage is represented implicitly and a finite difference scheme is applied in spite of the presence of discontinuities in the porosity. This can be expected to lead to further inaccuracy.

Our purpose is to produce an axisymmetric two dimensional code which corrects these deficiencies and permits a significant advance in our ability to predict the pressure wave amplitudes associated with bag charges. It should be clearly understood, however, that while our investigation into multi dimensional effects will be a major undertaking, it will not close all gaps between theory and experiment. There is strong evidence that many malfunctions^{25,28} may involve grain fracture, a process which has not yet been seriously addressed by anyone in the gun modeling community.

The present report addresses the formulation of the model, its governing equations and the method of solution. Furthermore, we encode the model to the point of enabling the determination of numerical solutions for a single two phase flow region of complex two dimensional shape.

1.3 Summary of Approach and Findings

We will first summarize both our overall approach and the findings of the present study. Subsequently, we will provide a more detailed discussion of the factors which have influenced the approach chosen here as well as some of the implications and limitations of our approach.

Our analytical approach may be summarized as follows. We divide the combustion chamber into disjoint regions in each of which all the flow variables may be regarded as continuously differentiable. In particular, one such region is allocated for each charge increment and the mixture boundaries always coincide with the region boundaries. Accordingly, a precise representation is made of the ullage. The flow inhibition associated with the bag material and its various liners may be embedded accurately as boundary conditions linking the flow in one region with that in its neighbors. For flexibility and economy we consider that the flow in a given region may be any one of two dimensional two phase, two dimensional single phase, quasi-one-dimensional two phase, quasi-one-dimensional single phase or lumped parameter single phase.

The governing equations for each of these types of regions consist of balance equations, which have been previously derived^{16,26}, and constitutive laws for which it is necessary, in some cases, to extrapolate from previous one dimensional laws. The approach used to generate numerical solutions is essentially a marching technique based on an explicit two step scheme. All physical regions are mapped, in a time dependent manner, onto a regular computational figure, either a unit line or a unit square.

²⁸. Olenick, P.J.Jr., "Investigation of the 76mm/62 Caliber Mark 75 Gun Mount Malfunction" NSWC/DL TR-3144 1975

The numerical approach is essentially a logical extension of that which we have previously implemented successfully for one dimensional problems¹⁸. An obvious milestone in the path of the desired extension is the demonstration of a stable integration scheme for a single region of two dimensional two phase flow in a closed chamber. Moreover, the demonstrated scheme must be clearly capable of interfacing in a natural manner with the additional requirements imposed by the considerations of multiple regions, including ullage, separated by explicitly represented boundaries.

The specific approach that we take to this particular milestone is as follows. We accommodate the geometrical complexity, imposed by the actual shape of a typical gun propellant chamber and an intruding projectile, by mapping the physical domain onto a square. An equipotential map of the type used by Thompson et al²⁹ is adopted for this purpose. The solution is updated at interior mesh points by means of the MacCormack scheme³⁰ modified according to some recommendations of Moretti³¹. The boundary values are updated using Kentzer's³² approach to the method of characteristics, also modified in accordance with some recommendations of Moretti.

We present stable solutions for three problems based on nominal data. The first two differ only in respect to the representation of the granular stress term, it being reversible in the first and irreversible in the second. The container is taken to have a curved breech closure similar to the mushroom in a howitzer. The tube is tapered and the base of the projectile is flat. Subsequently, in the third problem we allow the projectile to have a boattail which intrudes into the two phase flow producing as complicated a geometry as we expect to encounter, for any single region of continuous two phase flow, in future applications to howitzer charges.

The analytical basis for the model as a whole is presented in section 2.0. In section 3.0 we present the details of the method of solution and the three solutions described in the preceding paragraph.

Having now summarized our approach and present findings, we will attempt to clarify matters a little further by returning to the physical content of the model. In particular, we will comment on the nature and manner of modeling of the system components - breech block, tube, projectile, charge increments, igniter increments and the bag cloth, liner and additives.

-
- ²⁹. Thompson, J.F., Thames, F.C. and Mastin, C.W. "Automatic Numerical Generation of Body-Fitted Curvilinear Coordinate System for Field Containing Any Number of Arbitrary Two-Dimensional Bodies" *J. Comp. Phys.* 15, 299-319 1974
- ³⁰. MacCormack, R.W. "The Effect of Viscosity in Hypervelocity Impact Cratering" AIAA Paper No. 69-354 1969
- ³¹. Moretti, G. "Calculation of the Three-Dimensional, Supersonic, Inviscid, Steady Flow Past an Arrow-Winged Airframe" POLY-AE/AM Report No. 76-8 1976
- ³². Kentzer, C.P. "Discretization of Boundary Conditions on Moving Discontinuities" *Proc. 2nd Int. Conf. Num. Meth. in Fluid Dynamics Berkeley, Calif.* Sept. 15-19 1970

Figures 1.2.1 and 1.2.2 have respectively illustrated a typical case and bag charge in relation to the tube, breech and projectile. The points that we abstract from these figures are: (a) The tube is tapered and has fairly sharp corners associated with the forcing cone and the origin of rifling where the band of the projectile is approximately located (b) The breech of the Howitzer is roughly hemispherical. (c) The boattail of the projectile has a rather short intrusion into the tube. (d) Rather complex packaging elements are introduced at the front end of the case charge. (e) Although the figure does not make this clear, the bag charge is contained in a rather complex package consisting of a cloth bag, lined, in part, with lead foil to assist decoppering of the tube, and a layer of talc impregnated cloth to assist in the reduction of erosion. It is also not uncommon for a bag of potassium nitrate to be stitched onto one or both ends of the bag in order to eliminate muzzle flash. (f) It is evident that the bag charge is not an axisymmetric configuration. Thus our model involves a geometrical approximation from the very beginning. While it is not so obvious, the same is true of the case charge since the bayonet primer vents at a number of small holes and thereby introduces a three dimensional flow.

Each region occupied by propellant is modeled as a heterogeneous two phase mixture for which the balance equations have been established¹⁶. Thus, as in previous work¹⁴⁻¹⁸ we describe the flow by reference to macroscopic state variables which are presumed to be averages formed over a region large enough to contain many particles and yet small by comparison with the overall dimensions of the chamber. It should, however, be noted that the fundamental assumption that the scale of heterogeneity of the mixture is infinitesimal by comparison with the proportions of the chamber is on less firm ground when we turn from a consideration of axial to radial flow.

Also, as in previous work, the balance equations consist of statements of conservation of mass, momentum and energy for the gas phase and of mass and momentum for the solid phase. The solid phase is assumed to be microscopically incompressible so that an energy balance is tantamount to a heat transfer relation. Naturally, the bulk average temperature of the solid phase is not of interest; we assume that ignition is predicated on the surface temperature. As in previous work, we assume that drag, heat transfer and combustion can be represented by empirical correlations based on the macroscopic states of the two phases. The motion of the solid phase is taken to depend on the interphase drag, the macroscopic pressure gradient in the gas and also on intergranular stresses. These latter stresses are taken to depend on the porosity in an irreversible manner since the bed modulus is known to be much greater during unloading than during loading. In neither phase do we consider a macroscopic shear stress. The significant effects of viscosity and of heat conduction are assumed to be confined to the boundary layers around the particles and to be embedded in the correlations. They therefore appear in the balance equations as algebraic non-homogeneous terms rather than as higher order differentials.

Each region occupied by the mixture is treated as a continuum at all stages of the calculation. However, depending principally on its radial extent, it may be represented as either fully two dimensional or quasi-one-dimensional. Thus, in treating the bag charge shown in figure 1.2.2, we would expect the inner mixture region - the igniter - to be treated as quasi-one-dimensional at most. We shall have further comments below, on the modeling of the igniter.

In addition, it is expected on the basis of studies of the radial flow²⁶ that following the completion of flamespreading, no mixture region will require anything more detailed than a quasi-one-dimensional representation. The only non-trivial radial distribution, once flamespreading is complete, is expected to be that of porosity. Thus we expect that even if a fully two dimensional approach is adopted during flamespreading, the analysis will eventually be amenable to a quasi-two-dimensional treatment and, possibly, if the radial ullage disappears altogether, the latter portions of the interior ballistic cycle may be studied by the conventional quasi-one-dimensional model.

Similar considerations pertain to the regions which we employ in the representation of ullage. These are all presumed to contain an inviscid, non-heat-conducting, compressible gas. The neglect of diffusion is in accord with the purpose of the model which is to predict the structure of longitudinal pressure waves. It is believed that, at least in conventional charges, the influence of the tube mechanical and thermal boundary layers will be negligible.

Of course, if we were interested in erosion of the tube the behaviour of these boundary layers would be of paramount interest. We also note that predictions of maximum pressure of the tube are barely influenced by the heat loss to the tube and even the muzzle velocity is only affected to the extent of 3-5%. There is no doubt in our mind that the influence of wall friction and heat loss to the tube by the gas phase will be negligible in so far as the structure of the longitudinal pressure waves is concerned. An additional effect of the boundary layer, namely flow displacement may be influential in chambers which possess significant chambrage. Separation of the boundary layer at a sharp entrance to the tube could conceivably provide an appreciable constriction of the inviscid core flow. As far as displacement due to the transient developing boundary layer in the tube is concerned, estimates based on the momentum integral approach of Shelton et al³³ show that it may be neglected in medium caliber weapons.

The regions of ullage may be treated as two dimensional, quasi-one-dimensional in either the radial or the axial direction or as lumped parameter. As with the mixture regions, the principal criterion is extent in the radial and axial directions.

The influence of the bag material is readily seen to be embedded in the boundary conditions which govern the mass transfer between the mixture regions and the ullage regions. It is important to note that as flamespreading occurs the mixture regions will deform. Our approach follows this deformation precisely and the computational regions move and deform so that the boundaries are always located precisely.

We now summarize the representation of the system elements.

Breech Block, Tube and Projectile

The configuration of the chamber as defined by these elements is represented accurately through tabular input. However, corners in the individual boundary elements will not, in general, coincide with continuum mesh points.

³³. Shelton, S., Bergles, A. and Saha, P. "Study of Heat Transfer and Erosion in Gun Barrels" AFATL-TR-73-69

The projectile is assumed to move as a rigid body and to be opposed by a predetermined law of barrel resistance due to engraving of the rotating band. In general, the boundaries of the chamber are impermeable to both phases but gas loss due to poor obturation in the breech or at the rotating band can be considered. Modeling of the ignition train may also eventually require the consideration of a permeable boundary as discussed below.

Propellant Charge

It is assumed that each charge element consists of a single type of propellant and that within each such element, all the grains are initially identical. However, different elements need not contain the same propellant. The propellant is assumed to be characterized by the same data base considered in the one dimensional model¹⁸. The propellant is assumed to be heated by the gas phase until the surface temperature exceeds a value required for ignition and, subsequently, to regress in accordance with a steady state combustion law. The propellant moves as a consequence of drag, pressure gradient and also, intergranular stress.

Propellant Packaging

Since our interest is primarily directed towards bag charges we do not provide a model of the closure elements typical of case charges, figure 1.2.1, and which have played an important role in our one dimensional studies¹⁰. However, we assume that each charge element is surrounded by a bag material of negligible thickness and mechanical strength and which has variable permeability and inertia. The permeability is assumed to depend on the location of the surface element of the charge. If data become available, the permeability may be made time dependent by reference to the local mechanical and thermal environment. Once the bag material is determined to have been ruptured or rendered fully permeable it disappears from consideration in the model.

Ignition Train

The ignition train can be modeled by a combination of an external source and the representation of the center core charge as a quasi-one-dimensional two phase region. However, the author is not aware of data which demonstrate the reliability of predictions of flamespreading in black powder. Therefore, the representation of the ignition train by a predetermined rate of injection of energetic gas is thought to represent a more fruitful approach. Some comparisons of theoretical and observed flamespreading in black powder would soon resolve this issue. If the modeling of black powder combustion is indeed fruitful, then a mixture region can, in principle, be allocated for the representation of a black powder base pad. In such a case, the breech would be taken to be gas permeable in order to permit the simulation of the spit hole. However, that level of modeling is not recognized by the present study.

As regards the modeling of the ignition stimulus by an external source term, we note that previous one dimensional studies have incorporated a correction for the volume originally occupied by the condensed phase of the igniter^{17,18,26}. Here we take the attitude that, in the context of a two dimensional model, the correction for the volume of the condensed phase is no longer minor. Therefore, if it is to be considered at all, it must be embedded into a properly posed differential equation expressing macroscopic continuity of the substance in question.

We conclude the discussion of the model with some comments on its limitations of applicability. As has already been discussed, the neglect of the tube boundary layer implies that the model cannot be applied directly to problems of tube heat transfer and erosion. However, the model may be used to drive a boundary layer analysis.

The combustion model is doubtless oversimplified. However, the present status of the theory of transient combustion in the presence of cross flow is not sufficiently advanced to justify a more complete model. Likewise, the neglect of the possibility of grain fracture may well prevent the model from predicting catastrophic overpressures.

We also note that the scale of heterogeneity of medium caliber charges is not negligible by comparison with the radial dimensions of the tube. Accordingly, attempts to resolve too many of the details of the flow predicated on the ideal assumptions of a continuum theory are likely to amount to self-deception. Therefore, the liberal use of quasi-one-dimensional and lumped parameter representations is desirable not only to simplify the numerical analysis but also to pose the simulation consistently with the underlying assumptions.

We comment now on the choice of computational examples used to test the numerical scheme for two dimensional two phase flow. Figure 1.2.2 shows the bag configuration to be initially rectangular in cross section. However, we will represent the charge as uniformly occupying the entire chamber, including the region around the boattail. As we discuss further in section 4.0, such charge configurations are of immediate interest and are found in cased ammunition for which the projectile intrusion may be very large. The relevance of such a computational example to problems involving bag charges is simply this: as a consequence of igniter blast, the bed will expand and the most complicated geometry we expect, for any single region of continuous flow, corresponds to that defined by the external boundaries.

We conclude our introduction with some comments on the choice of the method of solution.

In terms of the gun problem and convective flamespreading in general, we note that several approaches have been used with reasonable success. We have used a variation of the MacCormack scheme³⁰ in our most recent work¹⁸ supplemented by the method of characteristics at the external and internal boundaries. Kuo has used a Lax-Wendroff type scheme also supplemented by the method of characteristics¹³. Krier has used the Richtmyer scheme with artificial viscosity¹² and Fisher has used the Lax scheme¹⁹⁻²². It should be noted that the Lax scheme is very inaccurate due to the large implicit viscosity embedded in the differencing technique. Thus stability is acquired only with a loss of accuracy. The artificial viscosity used by Krier and to a lesser extent by Kuo does not appear to be necessary in problems of gun flamespreading according to our own experience. Because we have had satisfactory results using the MacCormack scheme and the method of characteristics in our one dimensional simulation, it is natural for us to have considered using the same approach in our two dimensional simulations.

However, many papers are available to describe solutions of two dimensional unsteady multiphase flow, almost all being the work of the Los Alamos group. Fortunately, there appears to be complete compatibility between our balance equations and theirs³⁴, so that their methods are of particular interest.

We have previously commented on two papers by Harlow and Amsden^{35,36}. These papers demonstrate the feasibility of obtaining numerical solutions in two dimensions with several internal boundaries, all represented implicitly. Several programs are documented by the Los Alamos group including K-TIF³⁷, K-FIX³⁸ and KACHINA³⁹.

The methodology represented by these papers suffers from three difficulties when we relate it to our own application. In the first place, the implicit finite difference scheme is rather complicated. This is not a serious objection per se. However, if modifications are required in our application, the numerical ramifications may well be severe. For example, Lee et al⁴⁰ report difficulties experienced with the KACHINA code in applications to reactor containment problems. These difficulties included loss of stability and, not surprisingly, severe numerical diffusion problems. Secondly, there is a surprising lack of regard even for external boundary conditions in these papers. As usual, the reflection technique, which has been criticized by Moretti⁴¹ is used to describe impermeable boundaries. More seriously, a simple continuative condition is used in KACHINA to describe outflow, even for a subsonic condition. Since the outflow depends upon the external pressure in the subsonic mode, it is difficult to know what such solutions mean. Finally, the failure to capture explicitly the internal boundaries defined by jumps in porosity is a very serious omission as far as our application is concerned.

-
- 34. Gough, P.S. and Zwarts, F.J. "Modeling Heterogeneous Two Phase Reacting Flow" AIAA. J. v.17 n.1 17-25 January 1979
 - 35. Harlow, F.H. and Amsden, A.A. "Numerical Calculation of Multiphase Fluid Flow" J.Comp. Phys. v.17 19-52 1975
 - 36. Harlow, F.H. and Amsden, A.A. "Flow of Interpenetrating Material Phases" J. Comp. Phys. v.18 440-464 1975
 - 37. Harlow, F.H. and Amsden, A.A. "K-TIF: A Two-Fluid Computer Program for Downcomer Flow Dynamics" Los Alamos Scientific Laboratory, LA 6994 1978
 - 38. Rivard, W.C. and Torrey, M.D. "K-FIX: A Computer Program for Transient, Two-Dimensional, Two-Fluid Flow" Los Alamos Scientific Laboratory, LA-NUREG-6623 1977
 - 39. Amsden, A.A. and Harlow, F.H. "KACHINA: An Eulerian Computer Program for Multifield Fluid Flows" Los Alamos Scientific Laboratory LA-5680 1974
 - 40. Lee, W.H. and Lyczkowski, R.W. "Development of a State-of-the-Art Reactor Containment Program" Proc. 17th National Heat Transfer Conf. 1977
 - 41. Moretti, G. "The Importance of Boundary Conditions in the Numerical Treatment of Hyperbolic Equations" PIBAL Report No. 68-34 1968

The boundary conditions at the internal surfaces drive the flamespreading to a large degree since it is through these conditions that we express the behaviour of the bag and liner materials. Moreover, even a very small gap around the charge can be extremely influential in respect to flamespreading and the subsequent structure of the longitudinal pressure waves²⁶. Accordingly, the prospect of numerical diffusion which would obscure the existence of ullage is inadmissible in our application.

We close with the following general observations on the relative merits of explicit and implicit schemes. Explicit schemes are attractive because of their computational simplicity. Implicit schemes are generally more complex, requiring greater computation per time step, but offer stability over time steps which may greatly exceed those allowable with explicit schemes. When the allowable time step is sufficiently greater than that obtainable with an explicit scheme, the additional computational burden per time step, of the implicit scheme, becomes economically viable. Indeed, for problems which involve diffusion, the implicit schemes offer significant overall economy relative to explicit schemes.

In the present case, however, the nonhomogeneous terms are known to exert a dominant influence on the time step, at least during flamespreading. This has been not only our own experience using an explicit scheme¹⁸, but also that of Kuo⁴² who used an implicit scheme in a pioneering study of convective flamespreading in a stationary porous bed. Accordingly, as the explicit and implicit approaches to a finite difference scheme are expected to be similarly constrained, in regard to time step, the computational simplicity of the explicit scheme weighs strongly in its favor.

⁴². Kuo, K.K., Vichnevetsky, R. and Summerfield, M. "Theory of Flame Front Propagation in Porous Propellant Charges Under Confinement" AIAA J. v.11 No.4

2.0 GOVERNING EQUATIONS

As we have discussed in the introduction, our approach to the analysis of flamespreading and pressure wave development in a complex propelling charge is based on the solution of the balance equations for each region of continuous flow together with explicit boundary conditions which reflect the couplings between the regions. Our purpose, in the present section, is to take note of these equations in sufficient detail as to provide an analytical basis for our model. At the same time, we will define that subset of the governing equations whose numerical solution is undertaken in the present study.

Thus, section 2.1 includes equations for both two phase and single phase flow in both one and two dimensional regions. However, the subsequent numerical studies pertain solely to a two dimensional region of two phase flow. In section 2.2 we discuss the constitutive laws required to close the balance equations. In general, the extension from earlier one dimensional studies is analytically straightforward. However, new restrictions on the validity of the correlations for the interphase processes arise and are duly noted. We also note the simplified forms of the constitutive laws used in the present numerical studies.

Following the discussion of the constitutive laws, we consider, in section 2.3, the conditions which apply at both the external boundaries of the computational domain and at the internal boundaries which separate regions of continuous flow. As part of this topic we discuss the behaviour of the bag or packaging material and we note the form of the constitutive laws suitable for the description of bag strength, inertia and permeability. We also comment on the initial conditions.

We conclude, in section 2.4, with a characteristic analysis of the balance equations. The resulting conditions of compatibility play an essential role in respect to the method of solution, as we discuss further in section 3.0. Results are developed for both single and two phase two dimensional flow, although only the latter are used in the present numerical studies. We also note that the discussion of section 2.4 anticipates the numerical technique and therefore accounts for a transformation of independent variables whose purpose is to map each region of continuous flow onto a regular figure.

2.1 Systems of Balance Equations

We require statements of the balance equations for both two dimensional and quasi-one-dimensional flow of either a single or two phase substance. In the latter case we formulate the balance equations for each of the individual species. We also consider a lumped parameter description for a region of single phase flow, it being understood throughout this report that the single phase flow is always that defined by the gas phase.

The two phase flow balance equations are as given previously and are governing equations for macroscopic properties of each of the phases or averages formed over regions large in comparison with the scale of heterogeneity of the mixture. As in our previous work, the complex boundary layer phenomena - drag, heat transfer, combustion rate - appear as nonhomogeneous terms or algebraic entities in the balance equations. It is assumed that empirical correlations are available to relate these processes to the macroscopic state variables as we describe further in section 2.2.

The quasi-one-dimensional formulation of the two phase flow equations contains a provision for mass exchange with neighboring regions. Both the quasi-one-dimensional and the two dimensional systems incorporate a source term to reflect an ignition stimulus. However, heat loss to the tube is neglected and the stress tensor is taken to be isotropic for both species so that resistance to shearing is not considered for either the gas or the solid phase.

We assume the single phase continuum flow to be inviscid and non-heat conducting. However, we do retain the source terms which may embed either an ignition stimulus or mass transfer from a neighboring region.

2.1.1 Two Dimensional Two Phase Flow

In cylindrical coordinates such that z is the axial coordinate, r is the radial coordinate and t is the time, the balance equations take the forms:

Balance of Mass of Gas Phase

$$\frac{D\epsilon\rho}{Dt} + \epsilon\rho\left[\frac{\partial u}{\partial z} + \frac{\partial v}{\partial r}\right] = \dot{m} + \psi - \frac{\epsilon\rho v}{r} \quad 2.1.1.1$$

The notation conforms with that used previously. We have ρ , the density of the gas, ϵ the porosity, u and v the z - and r - components of gas phase velocity, D/Dt the convective derivative along the gas phase streamline, ψ the source term associated with a stimulus, \dot{m} the rate of production of gas due to combustion of the solid phase. It should be noted, in accordance with the discussion given in the introduction, that we neglect the volume occupied by the condensed phase of the ignition stimulus.

We recall:

$$\frac{D}{Dt} \equiv \frac{\partial}{\partial t} + u \frac{\partial}{\partial z} + v \frac{\partial}{\partial r} \quad 2.1.1.2$$

$$\dot{m} = (1-\epsilon) \frac{S_p}{V_p} \dot{\rho}_p = s_p \dot{\rho}_p \quad 2.1.1.3$$

Here S_p , V_p are the surface area and volume of an individual grain and \dot{d} is the rate of surface regression. We have introduced s_p as the surface area per unit volume.

Balance of Momentum of Gas Phase

$$\epsilon \rho \frac{D\vec{u}}{Dt} + \epsilon g_o \nabla p = -\vec{f} + \dot{m}(\vec{u}_p - \vec{u}) - \psi \vec{u} \quad 2.1.1.4$$

Here \vec{u} is the velocity with components u and v . Also, in cylindrical coordinates $\nabla p = (\partial p / \partial z, \partial p / \partial r)$. The vector form of the interphase drag \vec{f} should be noted.

Balance of Energy of Gas Phase

$$\begin{aligned} \epsilon \rho \frac{De}{Dt} + \epsilon p \left[\frac{\partial u}{\partial z} + \frac{\partial v}{\partial r} \right] + p \frac{D\epsilon}{Dt} &= \vec{f} \cdot (\vec{u} - \vec{u}_p) \\ &- s_p q + \dot{m} \left(e_p - e + \frac{p}{\rho_p} + \frac{|\vec{u} - \vec{u}_p|^2}{2g_o} \right) \\ &+ \psi \left(e_{IG} - e + \frac{\vec{u} \cdot \vec{u}}{2g_o} \right) - \epsilon p \frac{v}{r} \end{aligned} \quad 2.1.1.5$$

Here $e = e(p, \rho)$ is the internal energy of the gas phase and q is the interphase heat transfer per unit surface area of the solid phase.

Balance of Mass of Solid Phase

$$\frac{D\epsilon}{Dt}_p - (1-\epsilon) \left[\frac{\partial u_p}{\partial z} + \frac{\partial v_p}{\partial r} \right] = \frac{\dot{m}}{\rho_p} + (1-\epsilon) \frac{v_p}{r} \quad 2.1.1.6$$

The subscript p denotes properties of the solid phase and D/Dt_p is defined by analogy with 2.1.1.2.

Balance of Momentum of Solid Phase

$$(1-\epsilon) \rho_p \frac{D\vec{u}_p}{Dt}_p + (1-\epsilon) g_o \nabla p + g_o \nabla \sigma = \vec{f} \quad 2.1.1.7$$

The vector form of this equation should be noted. We have $\sigma = (1-\epsilon)R(\epsilon, \dot{\epsilon})$ where R is the average stress due to contacts between particles and

will be assumed to depend upon porosity in an irreversible manner.

2.1.2 Quasi-One-Dimensional Two Phase Flow

We assume that for the applications of interest to us, the non-trivial spacewise coordinate is aligned with the axis of the tube and that u , u_p are the non-trivial components of gas and solid phase velocity respectively. The cross sectional area of the annulus through which the flow occurs is taken to be $A(z,t)$ and therefore depends upon both position and time. It is supposed that the circumferential boundaries are permeable to the gas phase and that mass transfers must be considered. We use R_i and R_o to denote respectively the radii of a circumferential surface on which influx (\dot{m}_i) or efflux (\dot{m}_o) occur. Attention should be paid to this convention. The subscripts i and o do not refer to the interior and exterior surfaces, only to the direction of mass transfer. We understand \dot{m}_i and \dot{m}_o to represent rates of transfer per unit surface area. Moreover, we will also denote the properties transported with \dot{m}_i by the subscript i . Thus u_i will be the axial velocity associated with the incoming gas. The exiting properties are, of course, those of the gas in the quasi-one-dimensional region presently under consideration.

Balance of Mass of Gas Phase

$$\frac{\partial}{\partial t} \epsilon A \rho + \frac{\partial}{\partial z} \epsilon A \rho u = A \dot{m} + A \psi + 2\pi [\Sigma R_i \dot{m}_i - \Sigma R_o \dot{m}_o] \quad 2.1.2.1$$

Of course, the summations are over all entering and all exiting fluxes.

Balance of Momentum of Gas Phase

$$\epsilon \rho \frac{Du}{Dt} + \epsilon g_o \frac{\partial p}{\partial z} = -f - \psi u + \dot{m}(u_p - u) + \frac{2\pi}{A} \Sigma R_i \dot{m}_i (u_i - u) \quad 2.1.2.2$$

Balance of Energy of Gas Phase

$$\begin{aligned} \epsilon \rho \frac{De}{Dt} + \frac{p}{A} \frac{D\epsilon A}{Dt} + \epsilon p \frac{\partial u}{\partial z} &= \frac{f}{g_o} (u - u_p) - s_p q \\ &+ \psi [e_{IG} - e + \frac{u^2}{2g_o}] \\ &+ \dot{m} [e_p - e + \frac{p}{\rho_p} + \frac{(u - u_p)^2}{2g_o}] \\ &+ \frac{2\pi}{A} \Sigma \dot{m}_i R_i [e_i + \frac{p_i}{\rho_i} + \frac{(u - u_i)^2}{2g_o} - e] \\ &- \frac{2\pi}{A} \frac{p}{\rho} \Sigma \dot{m}_o R_o \end{aligned} \quad 2.1.2.3$$

Balance of Mass of Solid Phase

$$\frac{1}{A} \frac{D}{Dt} (1-\epsilon)A + (1-\epsilon) \frac{\partial u_p}{\partial z} = - \frac{\dot{m}}{\rho_p} \quad 2.1.2.4$$

Balance of Momentum of Solid Phase

$$\rho_p (1-\epsilon) \frac{Du_p}{Dt} + (1-\epsilon)g_o \frac{\partial p}{\partial z} + g_o \frac{\partial \sigma}{\partial z} = f \quad 2.1.2.5$$

2.1.3 Two Dimensional Single Phase (Gas) Flow

These equations are quite familiar. We also note that they represent the limiting forms of 2.1.1.1, 2.1.1.4 and 2.1.1.5 as $\epsilon \rightarrow 1$, bearing in mind that f , \dot{m} and $q \rightarrow 0$. We have:

Balance of Mass

$$\frac{D\rho}{Dt} + \rho \left[\frac{\partial u}{\partial z} + \frac{\partial v}{\partial r} \right] = \psi - \frac{\rho v}{r} \quad 2.1.3.1$$

Balance of Momentum

$$\rho \frac{D\vec{u}}{Dt} + g_o \nabla p = - \psi \vec{u} \quad 2.1.3.2$$

Balance of Energy

$$\rho \frac{De}{Dt} + p \left[\frac{\partial u}{\partial z} + \frac{\partial v}{\partial r} \right] = \psi \left[e_{IG} + \frac{\vec{u} \cdot \vec{u}}{2g_o} - e \right] - p \frac{v}{r} \quad 2.1.3.3$$

2.1.4 Quasi-One-Dimensional Single Phase (Gas) Flow

As in the previous section the balance equations for this case follow from those set forth in section 2.1.2 by taking the limit $\epsilon \rightarrow 0$. We have, assuming the axial direction to be non-trivial:

Balance of Mass

$$\frac{\partial}{\partial t} A\rho + \frac{\partial}{\partial z} A\rho u = A\psi + 2\pi [\Sigma R_i \dot{m}_i - \Sigma R_o \dot{m}_o] \quad 2.1.4.1$$

Balance of Momentum

$$\rho \frac{Du}{Dt} + g_o \frac{\partial p}{\partial z} = -\psi u + \frac{2\pi}{A} \Sigma \dot{R}_i \dot{m}_i (u_i - u) \quad 2.1.4.2$$

Balance of Energy

$$\begin{aligned} \rho \frac{De}{Dt} + \frac{p}{A} \frac{DA}{Dt} + p \frac{\partial u}{\partial z} &= \psi [e_{IG} - e + \frac{u^2}{2g_o}] \\ &+ \frac{2\pi}{A} \Sigma \dot{m}_i R_i [e_i + \frac{p_i}{\rho_i} + \frac{(u - u_i)^2}{2g_o} - e] \\ &- \frac{2\pi}{A} \frac{p}{\rho} \Sigma \dot{m}_o R_o \end{aligned} \quad 2.1.4.3$$

If, in fact, the non-trivial direction is not axial, the divergence and transfer terms must be suitably modified.

2.1.5 Lumped Parameter Single Phase (Gas) Flow

As in previous work we provide balance equations only for mass and energy. It is assumed that the velocity of the gas in the lumped parameter region can be deduced from the boundary values by interpolation. Using V to denote the volume of the region and S the bounding surface we have:

$$\frac{dV}{dt} = \int_S \vec{w} \cdot \vec{n} \, da \quad 2.1.5.1$$

where \vec{w} is the boundary velocity and \vec{n} is the outward facing normal. The mass balance is:

$$\frac{d}{dt} \rho V = \int_V \psi \, dv + \Sigma \dot{m}_i - \Sigma \dot{m}_o \quad 2.1.5.2$$

where the \dot{m}_i and \dot{m}_o now refer to the total fluxes rather than the fluxes per unit area used previously.

The energy balance is:

$$\frac{d}{dt} \rho EV = \int_V \psi e_{IG} dv + \sum_i \dot{m}_i \left(e_i + \frac{p_i}{\rho_i} + \frac{u_i^2}{2g_o} \right) - p \int_S \vec{w} \cdot \vec{n} da$$

$$- \sum_o \dot{m}_o \left(E + \frac{p}{\rho} \right) \quad 2.1.5.3$$

where E is the total energy $e + u^2/2g_o$.

2.2 Constitutive Laws

The constitutive laws required to close the foregoing systems of balance equations are of several types. As is usual in fluid mechanical problems we require an equation of state for the gas. However, we also need formulae for the particle surface area and volume and for the granular stress due to contacts among particles. In addition to these, we require formulae for the interphase transfer processes - drag, heat transfer and combustion. In order to discuss combustion we will have to introduce the surface temperature of the solid phase and a criterion for ignition. All of the above topics are addressed in the present section. However, the mass transfers from one region to another, due to the gas permeability of the boundary between them will be discussed in section 2.3.

2.2.1 Equation of State of Gas

It is assumed that the gas obeys the covolume equation of state:

$$e = c_v T = \frac{p(1-b\rho)}{(\gamma-1)\rho} \quad 2.2.1.1$$

where b is the covolume, γ is the ratio of specific heats and c_v is the specific heat at constant volume. In previous studies¹⁸ we have considered the composition dependence of the molecular weight and the specific heats. From an analytical viewpoint this simply amounts to the addition of two first order partial differential equations to the model. Physically, the consequences of the composition dependence are found to be small as the values of molecular weight and specific heat appropriate to the propellant are quickly attained. Moreover, we do not consider, herein, mixtures of propellants. Thus, in the present work we treat the molecular weight and the ratio of specific heats as constants, an assumption which can be relaxed easily when future studies so demand.

2.2.2 Granular Stress Law

The formulation of the granular stress law is of considerable importance not only because of the physical role played by the forces transmitted from grain to grain but also because of the influence of the stress law on the degree of hyperbolicity of the balance equations. Thus, although the present study can tolerate simplifications in certain of the constitutive laws for the sake of temporary expedience, it is essential that we evaluate our numerical scheme in the context of the physically complete granular stress law.

The granular stress is taken to depend on porosity and also on the direction of loading. As in the past¹⁴⁻¹⁸, we embed the constitutive law into the formula for the rate of propagation of intergranular disturbances:

$$a(\epsilon) = \left[-\frac{g_o}{\rho_p} \frac{d\sigma}{d\epsilon} \right]^{\frac{1}{2}} \quad 2.2.2.1$$

We may recast 2.2.2.1 into a form more suitable for numerical integration, namely:

$$\frac{D\sigma}{Dt}_p = - \rho_p \frac{a^2}{g_o} \frac{D\epsilon}{Dt}_p \quad 2.2.2.2$$

In order to formulate the functional behaviour of $a(\epsilon)$ we introduce ϵ_o , the settling porosity of the bed, and values of $a(\epsilon)$ equal to a_1 and a_2 which respectively correspond to loading at ϵ_o and to unloading/reloading. The nominal loading curve, corresponding to monotonic compaction of the bed from ϵ_o to a smaller value of the porosity ϵ is given by:

$$\sigma = \sigma_{nom}(\epsilon) = \rho_p \frac{a_1^2}{g_o} \epsilon_o^2 \left(\frac{1}{\epsilon} - \frac{1}{\epsilon_o} \right) \quad 2.2.2.3$$

The functional dependence of $a(\epsilon)$ may now be stated as:

$$a(\epsilon) = \begin{cases} a_1 \epsilon_o / \epsilon & \text{if } \dot{\epsilon} \leq 0, \sigma = \sigma_{nom}, \epsilon \leq \epsilon_o \\ a_2 & \text{if } 0 < \sigma < \sigma_{nom}, \epsilon \leq \epsilon_o \\ & \text{or if } \dot{\epsilon} > 0, \sigma = \sigma_{nom}, \epsilon \leq \epsilon_o \\ 0 & \text{if } \sigma = 0 \text{ and } \dot{\epsilon} > 0 \text{ or if } \epsilon > \epsilon_o \end{cases} \quad 2.2.2.4$$

Here we understand $\dot{\epsilon}$ to mean $D\epsilon/Dt_p$. In general, it appears that $a_2 \sim 3a_1$ so that the unload/reload modulus is roughly one order of magnitude greater than the nominal loading value. We emphasize that this constitutive law does not admit any granular stress when $\epsilon > \epsilon_o$, that is, when the bed is dispersed. We also emphasize the absence of the stress decay factor used in previous work for purely numerical reasons¹⁴⁻¹⁸.

2.2.3 Propellant Form Functions

It is assumed, in the present study, that the particles are multi-perforated cylinders having initial length L_o , external diameter D_o and perforation diameter d_o . The surface area per unit volume is related to the individual surface area S_p and volume V_p of the particle according to:

$$s_p = (1-\epsilon)S_p/V_p \quad 2.2.3.1$$

Until such time as slivering occurs, that is to say the time at which the regressing perforation surfaces intersect, the surface area and volume

are given by:

$$S_p = \pi(L_o - 2d)[(D_o - 2d) + N(d_o + 2d)] \\ + \pi/2[(D_o - 2d)^2 - N(d_o + 2d)^2] \quad 2.2.3.2$$

$$V_p = \pi(L_o - 2d)[(D_o - 2d)^2 - N(d_o + 2d)^2] \quad 2.2.3.3$$

where N is the number of perforations and d is the total linear surface regression, assumed uniform over the surface.

Formulae for other grain geometries are simple to determine provided that the initial configuration is regular and that slivering has not occurred. Formulae for the form functions following the slivering of seven perforation grains may be found in Krier et al⁴³.

2.2.4 Interphase Drag

In previous work¹⁵⁻¹⁸ we have assumed the interphase drag to be composed of a steady state component and a transient component reflecting the virtual mass effect:

$$\vec{f} = \vec{f}_s + (1-\epsilon)\beta\rho\left[\frac{D\vec{u}}{Dt} - \frac{D\vec{u}_p}{Dt}\right] \quad 2.2.4.1$$

where β is the virtual mass constant. However, while our one dimensional modeling exercises have carried the influence of virtual mass throughout the analysis and coding, actual calculations have almost always been based on the value $\beta = 0$, due to the absence of reliable independent data for the actual value. This being the case, we intend to neglect the virtual mass effect ab initio as a simplification of the present study.

The formula for the steady state component of the drag is assumed to follow as the obvious generalization of the one dimensional form:

$$\vec{f}_s = \frac{1-\epsilon}{D_p} \rho |\vec{u} - \vec{u}_p| (\vec{u} - \vec{u}_p) C_{DB}(\epsilon, Re_p) \quad 2.2.4.2$$

⁴³. Krier, H. Shimpi, S.A. and Adams, M.J. "Interior Ballistic Predictions Using Data From Closed and Variable Volume Simulators"
Tech. Rept. AAE 73-6, University of Illinois at Urbana-Champaign 1973

where D_p is the effective diameter of the particles, given as $D_p = 6V_p/S_p$ and $Re_p = \rho |\vec{u} - \vec{u}_p| D_p / \mu$ is the Reynolds number. In previous studies we have taken C_{DB} equal to the value reported by Ergun⁴⁴, for packed beds of various shaped particles, modified according to the tortuosity factor of Anderssen⁴⁵ as the bed becomes dispersed. In the present study we treat C_{DB} as constant and equal to Ergun's limiting value of 1.75 for high Reynolds number flows. Success with a vector form of Ergun's correlation has been reported by Stanek and Szekely⁴⁶.

The value of $C_{DB} = 1.75$ for a packed bed was determined by Ergun for a Reynolds number regime which is, in fact, low by comparison with the values expected in interior ballistic flows. Kuo⁴⁷ has shown that C_{DB} continues to decrease at least until $Re_p = 40000$, in beds of ball propellant and that a value of $C_{DB} \sim 1.3$ may be more typical of the interior ballistic situation in which $Re_p \sim 10^5$. In computing the effective diameter of the particles, the question arises as to the actual contribution of the surface area of the perforations. Robbins⁴⁸ has presented data which indicate that $C_{DB} \sim 1.2$ if the entire surface area is used to compute the effective diameter and that $C_{DB} \sim 1.9$ if only the contribution of the external surface is considered.

We also note that relatively few grains are present as we traverse the tube in a radial direction. Generally speaking, a medium caliber weapon whose diameter is, say, 15-20 cms has a charge consisting of grains whose lengths are typically 2-3 cms and whose diameters are typically 1 cm. The reported values of C_{DB} are based on flows through long columns for which entrance and exit effects are negligible. Evidently, as few as 5 grains may lie between the centerline of the tube and the inside of the wall. By investigating the drag on individual particles, van der Merwe and Gauvin⁴⁹ showed that seven or eight layers may be needed to produce conditions typical of a long bed.

-
44. Ergun, S. "Fluid Flow Through Packed Columns"
Chem. Eng. Progr. v.48 p.89 1952
45. Anderssen, K.E.B. "Pressure Drop in Ideal Fluidization"
Chem. Eng. Sci. V.15 1961
46. Stanek, V. and Szekely, J. "The Effect of Non-Uniform Porosity
in Causing Flow Maldistributions in Isothermal Packed Beds"
Can. J. Chem. Eng. v.50 1972
47. Kuo, K.K. and Nydegger, C.C. "Flow Resistance Measurement and
Correlation in a Packed Bed of WC-870 Ball Propellants",
J. Ballistics, v.2, No. 1 p.1 1978
48. Robbins, F. and Gough, P.S. "An Experimental Determination of Flow
Resistance in Packed Beds of Gun Propellant"
Proc. 15th Jannaf Combustion Meeting September 1978
49. van der Merwe, D.F. and Gauvin, W.H. "Pressure Drag Measurements
for Turbulent Air Flow Through a Packed Bed" A.I.Ch.E.J. 1971

2.2.5 Interphase Heat Transfer

Previously we have used both the Denton⁵⁰ correlation for packed beds and the Gelperin-Einstein⁵¹ correlation for dispersed and packed beds. However, the two are sufficiently close that we consider, herein, only the correlation of Gelperin-Einstein. We express the heat transfer in the form:

$$Nu_p = 0.4 Pr^{1/3} Re_p^{2/3} \quad 2.2.5.1$$

where

$$Nu_p = hD_p / k_f$$

$$Re_p = \rho_f |\vec{u} - \vec{u}_p| D_p / \mu_f$$

$$h = q / (T - T_p)$$

The subscript f denotes an evaluation of properties at the film temperature $(T + T_p)/2$ where T and T_p are respectively the gas bulk average temperature and the particle surface average temperature. The viscosity is taken to have a Sutherland type dependence on temperature:

$$\mu = 0.134064 \frac{(T/298)^{1.5}}{T + 110} \quad 2.2.5.2$$

The thermal conductivity follows from the Prandtl number which is assumed to satisfy:

$$Pr = \frac{c_p \mu}{k} = \frac{4\gamma}{9\gamma - 5} \quad 2.2.5.3$$

2.2.6 Solid Phase Surface Temperature

In previous one dimensional studies we have treated the determination of surface temperature as though conditions on the surface were essentially homogeneous. That is to say, the heat flux given by 2.2.5.1 was treated as uniform over the particle. Moreover, conduction to the interior was assumed to be governed by a one dimensional form of the heat diffusion equation and solved by means of a cubic profile¹⁴.

⁵⁰. Denton, W. H. "General Discussion on Heat Transfer"
Inst. Mech. Eng. and Am. Soc. Mech. Eng.

1951

⁵¹. Gelperin, N.I. and Einstein, V.G. "Heat Transfer in Fluidized Beds"
Fluidization, edited by J.F. Davidson and D. Harrison,
Academic Press

1971

The basis for the assumption of uniformity derives from observations of quenched beds. In these the surfaces show regular regression of all surfaces. Thus it is inferred that surface relaxation phenomena such as transverse flamespreading proceed very quickly. This need not always be true, however. Data acquired by Jakus⁵² in conditions of low pressure ignition revealed very poor uniformity. Also it is thought that the assumption of surface uniformity may be poor for long grains, particularly stick or cord, which have perforations.

In the multi dimensional calculation we have, in principle, an essentially new feature. The stagnation point on a given particle may vary as the direction of relative flow changes. In keeping with the previous assumption of surface uniformity, this feature is neglected. Thus the surface temperature is given by:

$$T_p = T_{p_o} - \frac{2}{3} \frac{hH}{k_p^2} + \left[\left(T_{p_o} - \frac{2}{3} \frac{hH}{k_p^2} \right)^2 + \frac{4}{3} \frac{hTH}{k_p^2} - T_{p_o} \right]^{\frac{1}{2}} \quad 2.2.6.1$$

where T_{p_o} is the initial surface temperature and H satisfies:

$$\frac{DH}{Dt_p} = \alpha_p q \quad 2.2.6.2$$

2.2.7 Ignition and Combustion

Ignition is assumed to occur when the surface temperature exceeds a predetermined value. The rate of surface regression is given by:

$$\frac{Dd}{Dt_p} = B_1 + B_2 p^n \quad 2.2.7.1$$

It should be noted that only one of 2.2.6.2 and 2.2.7.1 has to be solved at each point according as the temperature is less than or equal to the ignition temperature.

2.2.8 Primer Stimulus

The primer stimulus ψ is assumed to be given in tabular form as a predetermined function of space and time.

⁵² Jakus, K. "Study of Flame Spreading Through Single Base Propellant Beds" Proc. 11th Jannaf Combustion Meeting

2.3 Initial and Boundary Conditions

The initial conditions are more or less self evident and require only minimal attention. For problems of interest in interior ballistics we suppose that both phases are at rest and at atmospheric pressure. The temperatures of the two phases may differ but are uniform throughout each of the respective media. The porosity is piecewise continuous, the discontinuities being defined by the presence of ullage or of the boundary between bags.

We therefore turn our subsequent attention to the analysis of the boundary conditions. The natural starting point for this discussion is the form of the jump conditions at a discontinuity in two phase flow. This topic is addressed in section 2.3.1. Then, in sections 2.3.2, 2.3.3 and 2.3.4 we successively consider the boundary conditions which apply at the external boundaries, the gas permeable internal boundaries and at the impermeable internal boundaries. In the context of the latter topic it is natural to include the discussion of the behaviour of the bag or cloth material used to package the propellant.

2.3.1 Jump Conditions at a Discontinuity in Two Phase Flow

We have previously derived these results for one dimensional flow¹⁶. The extension to multidimensional flow is straightforward⁵³ and requires no new discussion. We designate the properties on each side of the discontinuity by the subscripts 1 and 2. Moreover, we use u_n and u_{pn} to denote the normal components of gas and solid phase velocity and u_T and u_{pT} to denote the transverse components. The jump conditions are:

$$j = \epsilon_1 \rho_1 (u_{n_1} - u_s) = \epsilon_2 \rho_2 (u_{n_2} - u_s) \quad 2.3.1.1$$

$$j_p = (1-\epsilon_1) \rho_p (u_{pn_1} - u_s) = (1-\epsilon_2) \rho_p (u_{pn_2} - u_s) \quad 2.3.1.2$$

$$p_1 + (1-\epsilon_1) R_1 + \frac{\epsilon_1 \rho_1}{g_o} (u_{n_1} - u_s)^2 + (1-\epsilon_1) \frac{\rho_p}{g_o} (u_{pn_1} - u_s)^2 \quad 2.3.1.3$$

$$= p_2 + (1-\epsilon_2) R_2 + \frac{\epsilon_2 \rho_2}{g_o} (u_{n_2} - u_s)^2 + (1-\epsilon_2) \frac{\rho_p}{g_o} (u_{pn_2} - u_s)^2$$

$$j \left\{ e_1 + \frac{p_1}{\rho_1} + \frac{(u_{n_1} - u_s)^2}{2g_o} \right\} = j \left\{ e_2 + \frac{p_2}{\rho_2} + \frac{(u_{n_2} - u_s)^2}{2g_o} \right\} \quad 2.3.1.4$$

⁵³. Kraiko, A.N. and Sternin, L.E. "Theory of Flow of a Two-Velocity Continuous Medium Containing Solid or Liquid Particles" PMM v.29, n.3 1965

$$j(u_{T_1} - u_{T_2}) = 0 \quad 2.3.1.5$$

$$j_p(u_{p_{T_1}} - u_{p_{T_2}}) = 0 \quad 2.3.1.6$$

Here we have used u_s to denote the normal velocity of a point on the surface of discontinuity. It is important to note that separate momentum jumps are not provided for the individual species. The momentum jump is expressed for the mixture alone. In general an exchange of momentum between the phases is not forbidden at the discontinuity.

We will confine our interest to the case $j_p = 0$ since we do not consider boundaries which are permeable to the solid phase. We may then distinguish two cases of interest.

(a) Impermeable Boundary, $j = 0$

Evidently the boundary conditions are the intuitively obvious set. We have:

$$u_{n_1} = u_{n_2} = u_s \quad 2.3.1.7$$

$$u_{p_{n_1}} = u_{p_{n_2}} = u_s \quad 2.3.1.8$$

$$p_1 + (1-\epsilon_1)R_1 = p_2 + (1-\epsilon_2)R_2 \quad 2.3.1.9$$

and the tangential components u_{T_1} , u_{T_2} , $u_{p_{T_1}}$, $u_{p_{T_2}}$ are unrestricted corresponding to slip conditions. In the event that the flow exists on only one side of the boundary 2.3.1.7, 2.3.1.8 and 2.3.1.9 apply to the non-trivial side. We also note that 2.3.1.7 is the familiar condition for the inviscid single phase flow.

(b) Gas Permeable Boundary, $j \neq 0$

We have the conditions:

$$\epsilon_1 \rho_1 (u_{n_1} - u_s) = \epsilon_2 \rho_2 (u_{n_2} - u_s) \quad 2.3.1.10$$

$$p_1 + (1-\epsilon_1)R_1 + \frac{\epsilon_1 \rho_1}{g_o} (u_{n_1} - u_s)^2 = p_2 + (1-\epsilon_2)R_2 + \frac{\epsilon_2 \rho_2}{g_o} (u_{n_2} - u_s)^2 \quad 2.3.1.11$$

$$e_1 + \frac{p_1}{\rho_1} + \frac{(u_{n1} - u_s)^2}{2g_o} = e_2 + \frac{p_2}{\rho_2} + \frac{(u_{n2} - u_s)^2}{2g_o} \quad 2.3.1.12$$

$$u_{T1} = u_{T2} \quad 2.3.1.13$$

Also, according to 2.3.1.6, an arbitrary jump in the tangential velocity of the solid phase is admitted. We observe that as $\epsilon_1, \epsilon_2 \rightarrow 1$ these conditions reduce to the familiar Rankine-Hugoniot conditions for a single phase fluid. In fact, 2.3.1.12, the condition of adiabatic flow, is unchanged by the presence of the solid phase. The condition of continuity of mass, 2.3.1.10, appears as the obvious generalization. The major novel features are associated with the momentum jump, 2.3.1.11. We see that progress cannot be made without either specifying the manner in which the granular stress behaves at the discontinuity or providing some functionally equivalent datum.

Since we have assumed R to embed the stresses due to direct contacts among the grains it is natural to postulate:

$$(1-\epsilon_1)R_1 = (1-\epsilon_2)R_2 \quad 2.3.1.14$$

whereupon the gas phase momentum jump becomes:

$$p_1 + \frac{\epsilon_1 \rho_1}{g_o} (u_{n1} - u_s)^2 = p_2 + \frac{\epsilon_2 \rho_2}{g_o} (u_{n2} - u_s)^2 \quad 2.3.1.15$$

However, the postulational nature of 2.3.1.14 should be emphasized. The tensor R arises formally as the difference between the average stress tensors for the two phases¹⁶. The argument that it embeds only the influence of granular contact is plausible only at low relative Mach numbers. At high Mach numbers the situation is complicated by the influence of the pressure distribution around each particle associated with drag.

On the other hand, 2.3.1.15 agrees with the familiar form of the momentum jump used to analyze flow losses at a sudden increase in the cross section of the flow^{54,55} of an incompressible fluid.

⁵⁴. Prandtl, L. and Tietjens, O.G. "Fundamentals of Hydro-and Aeromechanics" Dover Publications 1957

⁵⁵. Kaufmann, W. "Fluid Mechanics" McGraw-Hill 1963

2.3.2 External Boundaries

We do not consider the possibility of flow of the solid phase through an external boundary. The gas permeable boundary is of interest only for problems involving poor obturation or detailed simulation of the ignition train. The mass transfer relations for such cases can be deduced according to standard isentropic flow theory⁵⁶ and are not discussed here. We confine our attention, for the time being, to the fully impermeable boundary.

Accordingly, we have to consider simply the slip boundary conditions applied to both phases, equations 2.3.1.7, 2.3.1.8 and 2.3.1.9. For the surfaces of the tube and the breech we assume $u_s = 0$, corresponding to the neglect of recoil and strain.

Now let S_{PROJ} be the surface of the projectile which intrudes into the combustion chamber and let \vec{n} be the local normal to the surface, positive pointing outwards from the combustion chamber. Let $\vec{n} = (n_z, n_r)$ describe the z - and r - components of \vec{n} . Let the axial speed of the projectile be u_{PROJ} . Then the boundary conditions at the projectile surface are:

$$\vec{u} \cdot \vec{n} = \vec{u}_p \cdot \vec{n} = n_z u_{\text{PROJ}} \quad 2.3.2.1$$

Of course, the condition on the solid phase applies only in a region of two phase flow.

The projectile motion is assumed to be governed by:

$$M_{\text{eff}} \frac{du_{\text{PROJ}}}{dt} = \int_{S_{\text{PROJ}}} (p + (1-\epsilon)R) n_z da - F_{\text{res}} \quad 2.3.2.2$$

where the effective mass is related to the actual mass, M , and polar moment of inertia, I , according to:

$$M_{\text{eff}} = M + \frac{4I}{D^2} \tan^2 \theta \quad 2.3.2.3$$

and D and θ are respectively the diameter of the tube and the angle of the rifling. The quantity F_{res} is the bore resistance and will be assumed to be available as a semi-empirical correlation.

⁵⁶ Shapiro, A.H. "The Dynamics and Thermodynamics of Compressible Fluid Flow" Ronald Press 1953

2.3.3 Gas Permeable Internal Boundaries

We take equations 2.3.1.10, 2.3.1.12, 2.3.1.13, 2.3.1.14 and 2.3.1.15 to apply at all the internal boundaries defined by a jump in porosity. When the boundary separates two regions of two dimensional flow, the interpretation of these conditions is straightforward since they refer to the boundary values on each side of the discontinuity. We note, of course, that these conditions reduce correctly when one or both sides of the boundary contains a single phase flow.

When the boundary is such that the flow on one or both sides is quasi-one-dimensional or lumped parameter, care must be taken with the interpretation of terms. For example let side 1 correspond to two dimensional two phase flow so that values of ε_1 , p_1 , ρ_1 , u_{n_1} , $u_{p_{n_1}}$, u_{T_1} and $u_{p_{T_1}}$ are available. If the side 2 represents a quasi-one-dimensional model of the tangential flow, we identify ε_2 , p_2 with the state variables for side 2. However, u_{n_2} is not modeled except implicitly through the mass transfer terms \dot{m}_1 and \dot{m}_0 . The values of ρ_2 , e_2 , u_{T_2} correspond with the state of the quasi-one-dimensional flow only when that region is acting as a donor.

The assumption that 2.3.1.14 and 2.3.1.15 are valid restricts our analysis to relatively low subsonic transfers through the internal boundaries. In our opinion, further study is required to permit a meaningful analysis of the transonic and supersonic flows. Certainly, one can proceed pragmatically, using quasi-equilibrium nozzle flow analyses as a basis for determining solutions. However, the validity of such an approach is not clear at present.

Finally, we comment that from the application of these boundary conditions we, in effect, establish the constitutive laws for the mass transfer terms \dot{m}_1 and \dot{m}_0 as used in section 2.1.

2.3.4 Impermeable Internal Boundaries

This topic is of considerable importance since it is here that we embed the influence of the bag and additive materials on mass transfer and hence, on flamespreading. If the bag is impermeable we have as boundary conditions, 2.3.1.7, 2.3.1.8 and 2.3.1.9. As in the previous section, the interpretation of these terms is straightforward provided that both sides of the boundary correspond to a two dimensional flow.

When one or both sides is a quasi-one-dimensional two phase flow, the boundary condition 2.3.1.9 serves, in effect, to define the evolution of the cross sectional area. As we have shown previously²⁶, the constitutive law for the granular stress may be combined with the continuity equation for the solid phase to produce the desired result. We also showed²⁶ that when the bag became ruptured, the mass transfer deduced according to the previous section could be used to estimate the subsequent lateral dilation of the quasi-one-dimensional flow.

If the data base warrants, it may be of value to treat the internal boundary by explicitly recognizing the flow resistance and thermal loss associated with the bag material. Equations 2.3.1.11 and 2.3.1.12 may be

modified to reflect a finite loss of momentum and energy experienced by gas passing through the bag. Indeed, the permeability may be made time dependent and linked to flow parameters which characterize the mechanical and thermal attack due to the penetrating gas. Moreover, the momentum jump may also reflect an inertial loss associated with acceleration of the bag material. This level of modeling may well be necessary in order to study charge configurations composed of several bags or even for single bag charges in which a sophisticated use is made of the bag permeability to control flame-spreading.

2.4 Characteristic Analysis of Balance Equations

Our interest in this topic is principally motivated by the numerical ramifications of the theory of characteristic surfaces. In the case of one dimensional unsteady flow, the existence of real characteristic directions enables one to replace the system of partial differential equations by an equivalent system of ordinary differential equations in which the derivatives are taken along the characteristic lines. When we proceed to a larger number of independent variables an analogous result holds for hyperbolic systems of equations. Given n independent variables, a hyperbolic system is one that admits the existence of a hypersurface of dimension $n-1$ such that only derivatives interior to the surface appear in the equations.

We proceed as follows. In section 2.4.1, we discuss the theory in general for a quasi linear system of partial differential equations which depend on three independent coordinates. In section 2.4.2, we illustrate the theory by reference to the equations for unsteady homentropic flow with azimuthal symmetry.

In section 2.4.3 and 2.4.4 we deduce the characteristic forms for two dimensional single phase and two phase flows respectively.

2.4.1 Formulation of Characteristic Analysis

Consider a system of partial differential equations

$$A \frac{\partial \psi}{\partial t} + B \frac{\partial \psi}{\partial z} + C \frac{\partial \psi}{\partial r} = D \quad 2.4.1.1$$

where ψ and D are n -dimensional column vectors and A, B, C are $n \times n$ square matrices. The concept of a characteristic surface follows naturally from the consideration of an initial value problem posed for a surface:

$$\phi(t, z, r) = 0$$

or, in general, the family of surfaces generated by the parameter ϕ_0 such that:

$$\phi(t, z, r) = \phi_0 \quad 2.4.1.2$$

Let α, β be coordinates internal to the surface $\phi = \phi_0$ then ϕ itself serves as a normal coordinate. On $\phi = \phi_0$ we assume that we are given values of ψ and hence, values of ψ_α and ψ_β . The surface $\phi = \phi_0$ is said to be free if equation 2.4.1.1 permits the determination of the normal derivative ψ_ϕ and characteristic if it does not. If $\phi = \phi_0$ is characteristic it follows that 2.4.1.1 may be expressed in terms of derivatives with respect to α and β

alone, that is to say, derivatives internal to the characteristic surface.

By means of the chain rule for differentiation, 2.4.1.1 may be transformed into derivatives with respect to ϕ , α and β :

$$[A\phi_t + B\phi_z + C\phi_r]\psi_\phi = D - [A\alpha_t + B\alpha_z + C\alpha_r]\psi_\alpha - [A\beta_t + B\beta_z + C\beta_r]\psi_\beta \quad 2.4.1.3$$

Accordingly, the question of whether ϕ is free or characteristic is settled by the rank of the matrix:

$$\Delta = A\phi_t + B\phi_z + C\phi_r \quad 2.4.1.4$$

If $\text{Rank}(\Delta) = n$, the system 2.4.1.3 always has a unique solution ψ_ϕ and the surface $\phi = \phi_0$ is free. However, if the value of $\text{Rank}(\Delta) < n$ then 2.4.1.3 does not possess a solution for arbitrary initial data on the surface $\phi = \phi_0$. In the latter case the partial differential equation represents a constraint on the data as expressed by the condition of solvability of 2.4.1.3. Thus if we let Δ^+ be the augmented matrix formed by appending to Δ the column vector corresponding to the right hand side of 2.4.1.3.

$$\Delta^+ = [\Delta; D - [A\alpha_t + B\alpha_z + C\alpha_r]\psi_\alpha - [A\beta_t + B\beta_z + C\beta_r]\psi_\beta]$$

Then the condition of solvability is⁵⁷:

$$\text{Rank}(\Delta^+) = \text{Rank}(\Delta) \quad 2.4.1.5$$

The condition $\text{Rank}(\Delta) < n$ will lead to a partial differential equation for $\phi(t, z, r)$ in the form:

$$F(t, z, r, \psi, \phi_t, \phi_z, \phi_r) = 0 \quad 2.4.1.6$$

it being assumed that A, B, C are functions only of t, z, r and ψ . Since every element of Δ is a homogeneous linear combination of ϕ_t , ϕ_z and ϕ_r it follows that F is homogeneous of order $\kappa \geq 1$ in these quantities so that:

$$F(t, z, r, \psi, \lambda\phi_t, \lambda\phi_z, \lambda\phi_r) = \lambda^\kappa F(t, z, r, \psi, \phi_t, \phi_z, \phi_r) \quad 2.4.1.7$$

⁵⁷ Hadley, G. "Linear Algebra" Addison-Wesley 1961

Accordingly it follows that:

$$F_{\phi_t} \phi_t + F_{\phi_z} \phi_z + F_{\phi_r} \phi_r = 0 \quad 2.4.1.8$$

Because of the degree of freedom induced by the homogeneity of F it is convenient in many cases to append an additional condition corresponding to the normalization of the vector (ϕ_t, ϕ_z, ϕ_r) . In practice the most convenient choice is to set $\phi_t = -1$. This corresponds to having ϕ in the form:

$$\phi = t(z, r) - t \quad 2.4.1.9$$

so that $\phi_t = -1$, $\phi_z = \partial t / \partial z$ and $\phi_r = \partial t / \partial r$.

It is useful to interpret these results geometrically⁵⁸. We may think of $\phi = \phi_0$ as defining a surface with normal vector proportional to (ϕ_t, ϕ_z, ϕ_r) . Then 2.4.1.6, the partial differential equation for the characteristic surface, imposes an algebraic constraint on the components of the normal at each point in the (t, z, r) space. At each point 2.4.1.6 defines a family of planes such that the characteristic surface must be tangent to one of them. If F is not linear, the envelope of this family of planes is a cone, the Monge cone, whose generators are called bicharacteristics.

According to 2.4.1.7 the family of allowable normal vectors at a given point lies on the surface of a cone whose apex is the point in question. Thus 2.4.1.8 asserts that the vector $(F_{\phi_t}, F_{\phi_z}, F_{\phi_r})$ is perpendicular not only to the surface of normal vectors, but also to the vectors themselves since they lie along the cone. In fact, the vector $(F_{\phi_t}, F_{\phi_z}, F_{\phi_r})$ defines a bicharacteristic direction. From 2.4.1.8 it is evident that it must lie in a tangent plane of a characteristic surface. However, the bicharacteristic may be thought of as the limit of the line of intersection of neighboring tangent planes. Thus if we write \vec{b} as a bicharacteristic, \vec{n} as the normal to a tangent plane and λ as a parameter which labels the planes at a given point, it follows that $\vec{b} = \vec{n} \times (\vec{n} + \frac{d\vec{n}}{d\lambda} d\lambda)$. Therefore $\vec{b} = \vec{n} \times \frac{d\vec{n}}{d\lambda} d\lambda$. Since both \vec{n} and $\frac{d\vec{n}}{d\lambda}$ lie on a tangent plane of the cone defined by 2.4.1.6 we see that \vec{b} is parallel to $(F_{\phi_t}, F_{\phi_z}, F_{\phi_r})$. The bicharacteristic ray may be written as:

$$\frac{dt}{F_{\phi_t}} = \frac{dz}{F_{\phi_z}} = \frac{dr}{F_{\phi_r}} \quad 2.4.1.10$$

⁵⁸ Courant, R. and Hilbert, D. "Methods of Mathematical Physics" Interscience. 1953

This result may be used to eliminate ϕ_t , ϕ_z and ϕ_r from 2.4.1.6 and to describe the characteristic surface by reference to the bicharacteristics.

2.4.2 Illustration: Homentropic Flow

In order to understand the formulism we consider briefly the balance equations for homentropic, unsteady, single phase, compressible flow in two dimensions with cylindrical symmetry.

$$\frac{\partial \rho}{\partial t} + \frac{\partial}{\partial z} \rho u + \frac{\partial}{\partial r} \rho v + \frac{\rho v}{r} = 0 \quad 2.4.2.1$$

$$\frac{\partial u}{\partial t} + u \frac{\partial u}{\partial z} + v \frac{\partial u}{\partial r} + \frac{c^2}{\rho} \frac{\partial \rho}{\partial z} = 0 \quad 2.4.2.2$$

$$\frac{\partial v}{\partial t} + u \frac{\partial v}{\partial z} + v \frac{\partial v}{\partial r} + \frac{c^2}{\rho} \frac{\partial \rho}{\partial r} = 0 \quad 2.4.2.3$$

Here we have used $c^2 = (\partial p / \partial \rho)_s$ as the square of the speed of sound. We have:

$$\psi = \begin{bmatrix} \rho \\ u \\ v \end{bmatrix} \quad D = \begin{bmatrix} -\rho \frac{v}{r} \\ 0 \\ 0 \end{bmatrix}$$

$$A = \begin{bmatrix} 1 & 0 & 0 \\ 0 & 1 & 0 \\ 0 & 0 & 1 \end{bmatrix} ; \quad B = \begin{bmatrix} u & \rho & 0 \\ c^2/\rho & u & 0 \\ 0 & 0 & v \end{bmatrix}$$

$$C = \begin{bmatrix} v & 0 & \rho \\ 0 & v & 0 \\ c^2/\rho & 0 & v \end{bmatrix}$$

Thus we must consider the rank of:

$$\Delta = \begin{bmatrix} \phi_t + u\phi_z + v\phi_r & \rho\phi_z & \rho\phi_r \\ \frac{c^2}{\rho}\phi_z & \phi_t + u\phi_z + v\phi_r & 0 \\ \frac{c^2}{\rho}\phi_r & 0 & \phi_t + u\phi_z + v\phi_r \end{bmatrix}$$

A necessary condition that the rank of Δ be less than 3 is $\det(\Delta) = 0$ or:

$$(\phi_t + u\phi_z + v\phi_r)\{(\phi_t + u\phi_z + v\phi_r)^2 - c^2(\phi_r^2 + \phi_z^2)\} = 0 \quad 2.4.2.4$$

Evidently the characteristic surface consists of two sheets:

$$G(\phi_t, \phi_z, \phi_r) = \phi_t + u\phi_z + v\phi_r = 0 \quad 2.4.2.5$$

and
$$F(\phi_t, \phi_z, \phi_r) = (\phi_t + u\phi_z + v\phi_r)^2 - c^2(\phi_r^2 + \phi_z^2) = 0 \quad 2.4.2.6$$

The bicharacteristics corresponding to 2.4.2.5 are just the particle path-lines. Those for the quadratic sheet may be expressed as:

$$\vec{b} = \{2(\phi_t + u\phi_z + v\phi_r), 2u(\phi_t + u\phi_z + v\phi_r) - 2c^2\phi_z, \\ 2v(\phi_t + u\phi_z + v\phi_r) - 2c^2\phi_r\}$$

Accordingly we can express ϕ_t , ϕ_z and ϕ_r in terms of the components of $\vec{b} = (dt, dz, dr)$ as:

$$\phi_t = \{dt(c^2 - u^2 - v^2) + udz + vdr\}/c^2$$

$$\phi_z = (udt - dz)/c^2$$

$$\phi_r = (vdt - dr)/c^2$$

whereupon substitution into 2.4.2.6 shows the bicharacteristics to satisfy:

$$\left(\frac{dz}{dt} - u\right)^2 + \left(\frac{dr}{dt} - v\right)^2 = c^2 \quad 2.4.2.7$$

In a computational application we expect that dt is known as the time increment through which the solution is to be advanced. Moreover, we select the bicharacteristic to lie in a given plane. Therefore the ratio $dz:dr$ is known and 2.4.2.7 enables us to determine their separate values. These, when entered into the condition of compatibility lead to a finite difference formula for the state variables. Since we have no application for this simple case we do not bother to write down the condition of compatibility. It follows mechanically from a consideration of the augmented matrix.

2.4.3 Single Phase Two Dimensional Unsteady Flow

We now wish to deduce complete results for a two dimensional single phase flow. These results will differ from those of the preceding section in three essential respects. We will assume that an initial transformation of variables has been made for computational purposes. Secondly, we will not take the entropy to be the same for all fluid particles. Thirdly, we will deduce the conditions of compatibility.

The balance equations are given in cylindrical coordinates in section 2.1.3. As usual, we recast the energy equation by means of the continuity equation and the identity:

$$\frac{p}{\rho^2} - \left(\frac{\partial e}{\partial \rho}\right)_p = \frac{c^2}{g_o} \left(\frac{\partial e}{\partial p}\right)_\rho \quad 2.4.3.1$$

Thus we have:

$$\frac{D\rho}{Dt} + \rho\left(\frac{\partial u}{\partial z} + \frac{\partial v}{\partial r}\right) = \psi - \frac{\rho v}{r} = \xi_1 \quad 2.4.3.2$$

$$\rho \frac{Du}{Dt} + g_o \frac{\partial p}{\partial z} = -\psi u = \xi_2 \quad 2.4.3.3$$

$$\rho \frac{Dv}{Dt} + g_o \frac{\partial p}{\partial r} = -\psi v = \xi_3 \quad 2.4.3.4$$

$$\frac{Dp}{Dt} - \frac{c^2}{g_o} \frac{D\rho}{Dt} = \frac{\psi}{\rho\left(\frac{\partial e}{\partial p}\right)_\rho} \left\{ e_{IG} + \frac{\vec{u} \cdot \vec{u}}{2g_o} - e - p/\rho \right\} = \xi_4 \quad 2.4.3.5$$

where ψ is understood to be a source term and is not to be confused with the column vector of state variables.

We identify these equations with the system:

$$A \frac{\partial \psi}{\partial t} + B \frac{\partial \psi}{\partial z} + C \frac{\partial \psi}{\partial r} = D \quad 2.4.3.6$$

by setting:

$$\psi = \begin{bmatrix} \rho \\ u \\ v \\ p \end{bmatrix} ; \quad D = \begin{bmatrix} \xi_1 \\ \xi_2 \\ \xi_3 \\ \xi_4 \end{bmatrix} ; \quad A = \begin{bmatrix} 1 & 0 & 0 & 0 \\ 0 & \rho & 0 & 0 \\ 0 & 0 & \rho & 0 \\ -\frac{c^2}{g_0} & 0 & 0 & 1 \end{bmatrix}$$

$$B = \begin{bmatrix} u & \rho & 0 & 0 \\ 0 & \rho u & 0 & g_0 \\ 0 & 0 & \rho v & 0 \\ -\frac{c^2 u}{g_0} & 0 & 0 & u \end{bmatrix}$$

$$C = \begin{bmatrix} v & 0 & \rho & 0 \\ 0 & \rho v & 0 & 0 \\ 0 & 0 & \rho v & g_0 \\ -\frac{c^2 v}{g_0} & 0 & 0 & v \end{bmatrix} \quad 2.4.3.7$$

At this point we have established the balance equations in a form suitable for the application of the methodology described in section 2.4.1. However, we now consider a transformation of coordinates in the form:

$$\begin{aligned} \tau &= t \\ \zeta &= \zeta(t, z, r) \\ \eta &= \eta(t, z, r) \end{aligned} \quad 2.4.3.8$$

We assume that this transformation is one to one and has continuous partial

derivatives and that $\partial(\zeta, \eta)/\partial(z, r) \neq 0$ so that we can also write:

$$\begin{aligned} t &= \tau \\ z &= z(\tau, \zeta, \eta) \\ r &= r(\tau, \zeta, \eta) \end{aligned} \quad 2.4.3.9$$

We have used a separate notation τ for the time in the transformed frame. This facilitates the use of subscripts to denote partial derivatives. Thus we understand $\phi_t = (\frac{\partial \phi}{\partial t})_{z, r}$ whereas $\phi_\tau = (\frac{\partial \phi}{\partial \tau})_{\zeta, \eta}$ and ϕ is an arbitrary property.

Bearing this in mind we define:

$$\begin{aligned} u_m &= z_\tau \\ v_m &= r_\tau \end{aligned} \quad 2.4.3.10$$

Thus u_m and v_m are the velocity components in a cylindrical coordinate frame of a point moving so that it is stationary with respect to the transformed frame. Evidently, if we impose the requirement $u_m = u$ and $v_m = v$ we will have selected the transformed frame to coincide with a Lagrangian description of the fluid whereas the choice $u_m = v_m = 0$ implies the retention of an Eulerian description, possibly in a different coordinate frame established by a stationary transformation.

It follows that the balance equations 2.4.3.6 subject to 2.4.3.8 and 2.3.4.10 become:

$$A \frac{\partial \psi}{\partial \tau} + [(B - Au_m)\zeta_z + (C - Av_m)\zeta_r] \frac{\partial \psi}{\partial \zeta} + [(B - Au_m)\eta_z + (C - Av_m)\eta_r] \frac{\partial \psi}{\partial \eta} = D \quad 2.4.3.11$$

Thus we now consider the characteristic surfaces for the system:

$$A \frac{\partial \psi}{\partial \tau} + B' \frac{\partial \psi}{\partial \zeta} + C' \frac{\partial \psi}{\partial \eta} = D \quad 2.4.3.12$$

where we identify B' and C' as:

$$B' = \begin{bmatrix} w & \rho \zeta_z & \rho \zeta_r & 0 \\ 0 & \rho w & 0 & g_o \zeta_z \\ 0 & 0 & \rho w & g_o \zeta_r \\ -c^2 w / g_o & 0 & 0 & w \end{bmatrix}$$

$$C' = \begin{bmatrix} x & \rho \eta_z & \rho \eta_r & 0 \\ 0 & \rho x & 0 & g_o \eta_z \\ 0 & 0 & \rho x & g_o \eta_r \\ -c^2 x / g_o & 0 & 0 & x \end{bmatrix}$$

and where we have introduced:

$$\begin{aligned} w &= (u-u_m)\zeta_z + (v-v_m)\zeta_r \\ x &= (u-u_m)\eta_z + (v-v_m)\eta_r \end{aligned} \quad 2.4.3.13$$

Then the characteristic surfaces $\phi(\tau, \zeta, \eta)$ are such that the rank of Δ is less than four where:

$$\Delta = A\phi_\tau + B'\phi_\zeta + C'\phi_\eta \quad 2.4.3.14$$

Thus we have:

$$\Delta = \begin{bmatrix} \dot{\phi} & \rho(\zeta_z\phi_\zeta + \eta_z\phi_\eta) & \rho(\zeta_r\phi_\zeta + \eta_r\phi_\eta) & 0 \\ 0 & \rho\dot{\phi} & 0 & g_o(\zeta_z\phi_\zeta + \eta_z\phi_\eta) \\ 0 & 0 & \rho\dot{\phi} & g_o(\zeta_r\phi_\zeta + \eta_r\phi_\eta) \\ -c^2\dot{\phi}/g_o & 0 & 0 & \dot{\phi} \end{bmatrix}$$

and where we have introduced:

$$\dot{\phi} = \phi_\tau + w\phi_\zeta + x\phi_\eta \quad 2.4.3.15$$

Now in our applications of the conditions of compatibility we shall always require that either $\phi_\zeta = 0$ or that $\phi_\eta = 0$ so that the normal lies either in the τ - η plane or the τ - ζ plane. We assume therefore that $\phi_\eta = 0$. The corresponding results for the case $\phi_\zeta = 0$ will follow from considerations of symmetry. With this assumption Δ reduces to:

$$\Delta = \begin{bmatrix} \dot{\phi} & \rho\zeta_z\phi_\zeta & \rho\zeta_r\phi_\zeta & 0 \\ 0 & \rho\dot{\phi} & 0 & g_o\zeta_z\phi_\zeta \\ 0 & 0 & \rho\dot{\phi} & g_o\zeta_r\phi_\zeta \\ -c^2\dot{\phi}/g_o & 0 & 0 & \dot{\phi} \end{bmatrix} \quad 2.4.3.16$$

Now we consider two possibilities

(i) Let $\dot{\phi} = 0$ Then Δ reduces to:

$$\Delta = \begin{bmatrix} 0 & \rho\phi_{\zeta}\zeta_z & \rho\phi_{\zeta}\zeta_r & 0 \\ 0 & 0 & 0 & g_o\zeta_z\phi_{\zeta} \\ 0 & 0 & 0 & g_o\zeta_r\phi_{\zeta} \\ 0 & 0 & 0 & 0 \end{bmatrix}$$

From this it is apparent that the streamline

$$\dot{\phi} = \phi_{\tau} + w\phi_{\zeta} = 0$$

is a characteristic direction. In order to establish the condition of compatibility we now introduce α and β as coordinates internal to the characteristic surface. Then we may write the augmented matrix as:

$$\Delta^+ = \left[\begin{array}{c} \xi_1 - \{\dot{\alpha}\rho_{\alpha} + \rho[\zeta_z\alpha_{\zeta} + \eta_z\alpha_{\eta}]u_{\alpha} + \rho[\zeta_r\alpha_{\zeta} + \eta_r\alpha_{\eta}]v_{\alpha}\} \\ \quad - \{\dot{\beta}\rho_{\beta} + \rho[\zeta_z\beta_{\zeta} + \eta_z\beta_{\eta}]u_{\beta} + \rho[\zeta_r\beta_{\zeta} + \eta_r\beta_{\eta}]v_{\beta}\} \\ \xi_2 - \{\rho\dot{\alpha}u_{\alpha} + g_o[\zeta_z\alpha_{\zeta} + \eta_z\alpha_{\eta}]p_{\alpha}\} \\ \quad - \{\rho\dot{\beta}u_{\beta} + g_o[\zeta_z\beta_{\zeta} + \eta_z\beta_{\eta}]p_{\beta}\} \\ \xi_3 - \{\rho\dot{\alpha}v_{\alpha} + g_o[\zeta_r\alpha_{\zeta} + \eta_r\alpha_{\eta}]p_{\alpha}\} \\ \quad - \{\rho\dot{\beta}v_{\beta} + g_o[\zeta_r\beta_{\zeta} + \eta_r\beta_{\eta}]p_{\beta}\} \\ \xi_4 - \dot{\alpha}[p_{\alpha} - c^2\rho_{\alpha}/g_o] - \dot{\beta}[p_{\beta} - c^2\rho_{\beta}/g_o] \end{array} \right]$$

where $\dot{\alpha}$ and $\dot{\beta}$ are defined by analogy with $\dot{\phi}$.

Accordingly, if we write ξ_i' , $i=1, \dots, 4$ to denote the members of the fifth column of Δ^+ , the conditions of solvability yield the following conditions of compatibility.

$$\zeta_z \xi_3' - \zeta_r \xi_2' = 0 \quad 2.4.3.17$$

$$\xi_4' = 0 \quad 2.4.3.18$$

A convenient choice for α , β is:

$$\alpha = \zeta \quad \beta = \eta \quad 2.4.3.19$$

and we will adhere to this convention. The use of a separate nomenclature for the coordinates internal to the characteristic surface is again motivated by the desire to maintain clarity in respect to the representation of the partial derivatives.

Evidently:

$$\alpha_\tau = \alpha_\eta = \beta_\tau = \beta_\zeta = 0$$

$$\alpha_\zeta = \beta_\eta = 1$$

It follows that $wv_\alpha = v_\tau + w\psi_\zeta$ whereupon 2.4.3.17 may be identified as a linear combination of the two momentum equations.

On the other hand, since the bicharacteristic ray satisfies $d\alpha = w d\tau$ we can write 2.4.3.18 as:

$$[p_\alpha - \frac{c^2}{g_o} \rho_\alpha] d\alpha = [\xi_4 - (p_\beta - \frac{c^2}{g_o} \rho_\beta)] d\tau \quad 2.4.3.20$$

This is now recognized as the familiar one dimensional result with the β - derivatives (i.e. η -derivatives) taken to the right hand side and treated formally as non-homogeneous terms.

(ii) Now let $\dot{\phi} \neq 0$. Then perform successively the following row and column operations to Δ as given by equation 2.4.3.16. Add g_o/c^2 times column one to column four; subtract $\zeta_z \phi_\zeta / \dot{\phi}$ times row two from row one; subtract $g_o \zeta_z \phi_\zeta / \rho \dot{\phi}$ times column two from column four; subtract $g_o \zeta_r \phi_\zeta / \rho \dot{\phi}$ times column three from column four; subtract $-\zeta_r \phi_\zeta / \dot{\phi}$ times row three from row one; add g_o/c^2 times row four to row one. Then Δ is equivalent to $\bar{\Delta}$ where:

$$\bar{\Delta} = \begin{bmatrix} 0 & 0 & 0 & \frac{g_o}{\dot{\phi} c^2} [\dot{\phi}^2 - c^2(\zeta_z^2 \phi_\zeta^2 + \zeta_r^2 \phi_\zeta^2)] \\ 0 & \rho \dot{\phi} & 0 & 0 \\ 0 & 0 & \rho \dot{\phi} & 0 \\ -c^2 \dot{\phi} / g_o & 0 & 0 & 0 \end{bmatrix}$$

Accordingly, ϕ can only be characteristic if:

$$\dot{\phi}^2 = c^2 \phi_\zeta^2 \quad 2.4.3.21$$

That is:

$$\phi_\tau = -[w \pm c\sqrt{\zeta_z^2 + \zeta_r^2}] \phi_\zeta \quad 2.4.3.22$$

Thus the bicharacteristics satisfy the familiar one dimensional form:

$$d\tau = \frac{d\zeta}{w \pm c(\zeta_z^2 + \zeta_r^2)^{1/2}} \quad 2.4.3.23$$

The corresponding condition of compatibility is easily seen to be:

$$\xi_1' - \frac{\zeta_z \phi_\zeta}{\dot{\phi}} \xi_2' - \frac{\zeta_r \phi_\zeta}{\dot{\phi}} \xi_3' + \frac{g_o}{c^2} \xi_4' = 0$$

Then choosing α and β as before, equation 2.4.3.19, and observing $\phi_\zeta / \dot{\phi} = \mp 1/c_*$ where $c_* = c(\zeta_z^2 + \zeta_r^2)^{1/2}$ the condition of compatibility may be expressed as:

$$\begin{aligned} & \{p_\alpha \pm \frac{\rho c}{g_o} \frac{(\zeta_z u_\alpha + \zeta_r v_\alpha)}{\sqrt{\zeta_z^2 + \zeta_r^2}}\} d\alpha \\ &= c_*^2 d\tau \{ [\xi_1 - (x\rho_\beta + \rho\eta_z u_\beta + \rho\eta_r v_\beta)] \\ & \quad \pm \frac{\zeta_z}{c_*} [\xi_2 - (\rho x u_\beta + g_o p_\beta \eta_z)] \\ & \quad \pm \frac{\zeta_r}{c_*} [\xi_3 - (\rho x v_\beta + g_o p_\beta \eta_r)] \\ & \quad + \frac{g_o}{c^2} [\xi_4 - x(p_\beta - \frac{c^2}{g_o} \rho_\beta)] \} \end{aligned} \quad 2.4.3.24$$

As before, the β - derivatives are, in effect, η - derivatives which is to say derivatives along a coordinate curve which we may align with a computational boundary. Again, 2.4.3.24 is analogous with the one dimensional result with the cross derivatives (β - derivatives) treated formally as non homogeneous terms.

2.4.4. Two Phase Two Dimensional Unsteady Flow

Finally, we wish to establish complete results for a two dimensional two phase flow, including the conditions of compatibility. As in the preceding section we shall see that the algebraic problem is complicated only to the extent that the non-homogeneous terms now include derivatives along one of the internal coordinate directions. This direction will always conform with a computational coordinate line as a consequence of the transformation 2.4.3.8 which we will also apply to the two phase flow equations.

In addition, we will introduce a parameter λ into the solid phase momentum equations such that when $\lambda = 1$ the pressure gradient is treated, correctly, as a differential term and when $\lambda = 0$, the pressure gradient is treated as a non-homogeneous term. It is emphasized that the results corresponding to a non-unit value of λ are to be thought of as merely formal; they do not represent the hyperbolic structure of the balance equations. Our purpose in introducing them is to provide certain approximate results for use in determining numerical solutions.

The system to be studied includes, of course, the balance equations 2.1.1.1 through 2.1.1.7. In addition, we must consider the constitutive law 2.2.2.2 which is in differential form. The constitutive laws 2.2.6.2 and 2.2.7.1 need not be considered. Although they are expressed as partial differential equations, they are not coupled, at a differential level, to the other governing equations.

Eliminating the internal energy in favor of the pressure and density in 2.1.1.5 and adding the appropriate component of $(\lambda-1)(1-c)g_o \nabla p$ to each side of 2.1.1.7 leads to the system, in transformed coordinates:

$$A \frac{\partial \psi}{\partial \tau} + B' \frac{\partial \psi}{\partial \zeta} + C' \frac{\partial \psi}{\partial \eta} = D \quad 2.4.4.1$$

Where:

$$\psi = \begin{bmatrix} \rho \\ u \\ v \\ p \\ \epsilon \\ u_p \\ v_p \\ \sigma \end{bmatrix} \quad 2.4.4.2$$

$$D = \begin{bmatrix} \xi_1 \\ \xi_2 \\ \xi_3 \\ \xi_4 \\ \xi_5 \\ \xi_6 \\ \xi_7 \\ \xi_8 \end{bmatrix} = \begin{bmatrix} \dot{m} + \psi - \frac{\epsilon \rho v}{r} \\ -f_z + \dot{m}(u_p - u) - \psi u \\ -f_r + \dot{m}(v_p - v) - \psi v \\ \frac{1}{\epsilon \rho (\frac{\partial e}{\partial p})_\rho} \{ \vec{f} \cdot (\vec{u} - \vec{u}_p) - s_p q + \dot{m}(e_p - e + p(\frac{1}{\rho_p} - \frac{1}{\rho})) \\ + \frac{|\vec{u} - \vec{u}_p|^2}{2g_o} \} + \psi(e_{IG} - \frac{p}{\rho} - e + \frac{\vec{u} \cdot \vec{u}}{2g_o}) \\ \dot{m}/\rho_p + (1-\epsilon)v_p/r \\ f_z + (\lambda-1)(1-\epsilon)g_o \partial p / \partial z \\ f_r + (\lambda-1)(1-\epsilon)g_o \partial p / \partial r \\ 0 \end{bmatrix} \quad 2.4.4.3$$

$$A = \begin{bmatrix} \varepsilon & 0 & 0 & 0 & \rho & 0 & 0 & 0 \\ 0 & \varepsilon\rho & 0 & 0 & 0 & 0 & 0 & 0 \\ 0 & 0 & \varepsilon\rho & 0 & 0 & 0 & 0 & 0 \\ -\frac{c^2}{g_o} & 0 & 0 & 1 & 0 & 0 & 0 & 0 \\ 0 & 0 & 0 & 0 & 1 & 0 & 0 & 0 \\ 0 & 0 & 0 & 0 & 0 & (1-\varepsilon)\rho_p & 0 & 0 \\ 0 & 0 & 0 & 0 & 0 & 0 & (1-\varepsilon)\rho_p & 0 \\ 0 & 0 & 0 & 0 & \rho_p \frac{a^2}{g_o} & 0 & 0 & 1 \end{bmatrix} \quad 2.4.4.4$$

$$B' = \begin{bmatrix} \varepsilon w & \varepsilon\rho\zeta_z & \varepsilon\rho\zeta_r & 0 & \rho w & 0 & 0 & 0 \\ 0 & \varepsilon\rho w & 0 & \varepsilon g_o \zeta_z & 0 & 0 & 0 & 0 \\ 0 & 0 & \varepsilon\rho w & \varepsilon g_o \zeta_r & 0 & 0 & 0 & 0 \\ -\frac{c^2 w}{g_o} & 0 & 0 & w & 0 & 0 & 0 & 0 \\ 0 & 0 & 0 & 0 & w_p & -(1-\varepsilon)\zeta_z & -(1-\varepsilon)\zeta_r & 0 \\ 0 & 0 & 0 & \lambda(1-\varepsilon)g_o \zeta_z & 0 & (1-\varepsilon)\rho_p w_p & 0 & g_o \zeta_z \\ 0 & 0 & 0 & \lambda(1-\varepsilon)g_o \zeta_r & 0 & 0 & (1-\varepsilon)\rho_p v_p & g_o \zeta_r \\ 0 & 0 & 0 & 0 & \rho_p \frac{a^2 w_p}{g_o} & 0 & 0 & w_p \end{bmatrix} \quad 2.4.4.5$$

$$C' = \begin{bmatrix} \epsilon x & \epsilon \rho \eta_z & \epsilon \rho \eta_r & 0 & \rho x & 0 & 0 & 0 \\ 0 & \epsilon \rho x & 0 & \epsilon g_o \eta_z & 0 & 0 & 0 & 0 \\ 0 & 0 & \epsilon \rho x & \epsilon g_o \eta_r & 0 & 0 & 0 & 0 \\ -\frac{c^2 x}{g_o} & 0 & 0 & x & 0 & 0 & 0 & 0 \\ 0 & 0 & 0 & 0 & x_p & -(1-\epsilon)\eta_z & -(1-\epsilon)\eta_r & 0 \\ 0 & 0 & 0 & \lambda(1-\epsilon)g_o \eta_z & 0 & (1-\epsilon)\rho_p x_p & 0 & g_o \eta_z \\ 0 & 0 & 0 & \lambda(1-\epsilon)g_o \eta_r & 0 & 0 & (1-\epsilon)\rho_p x_p & g_o \eta_r \\ 0 & 0 & 0 & 0 & \rho_p \frac{a^2 x_p}{g_o} & 0 & 0 & x_p \end{bmatrix} \quad 2.4.4.6$$

As in the previous section we have introduced the kinematic coefficients w , x , w_p and x_p such that:

$$w = (u - u_m)\zeta_z + (v - v_m)\zeta_r$$

$$x = (u - u_m)\eta_z + (v - v_m)\eta_r$$

2.4.4.7

$$w_p = (u_p - u_m)\zeta_z + (v_p - v_m)\zeta_r$$

$$x_p = (u_p - u_m)\eta_z + (v_p - v_m)\eta_r$$

The characteristics are determined from the rank of Δ given by:

$$\Delta = \begin{bmatrix} \epsilon \dot{\phi} & \epsilon \rho (\zeta_z \phi_\zeta + \eta_z \phi_\eta) & \epsilon \rho (\zeta_r \phi_\zeta + \eta_r \phi_\eta) & 0 & \rho \dot{\phi} & 0 & 0 & 0 \\ 0 & \epsilon \rho \dot{\phi} & 0 & \epsilon g_o (\zeta_z \phi_\zeta + \eta_z \phi_\eta) & 0 & 0 & 0 & 0 \\ 0 & 0 & \epsilon \rho \dot{\phi} & \epsilon g_o (\zeta_r \phi_\zeta + \eta_r \phi_\eta) & 0 & 0 & 0 & 0 \\ -\frac{c^2 \dot{\phi}}{g_o} & 0 & 0 & \dot{\phi} & 0 & 0 & 0 & 0 \\ 0 & 0 & 0 & 0 & \dot{\phi}_p & -(1-\epsilon)(\zeta_z \phi_\zeta + \eta_z \phi_\eta) & -(1-\epsilon)(\zeta_r \phi_\zeta + \eta_r \phi_\eta) & 0 \\ 0 & 0 & 0 & g_o \lambda (1-\epsilon) (\zeta_z \phi_\zeta + \eta_z \phi_\eta) & 0 & (1-\epsilon) \rho_p \dot{\phi}_p & 0 & g_o (\zeta_z \phi_\zeta + \eta_z \phi_\eta) \\ 0 & 0 & 0 & g_o \lambda (1-\epsilon) (\zeta_r \phi_\zeta + \eta_r \phi_\eta) & 0 & 0 & (1-\epsilon) \rho_p \dot{\phi}_p & g_o (\zeta_r \phi_\zeta + \eta_r \phi_\eta) \\ 0 & 0 & 0 & 0 & \rho_p \frac{a^2 \dot{\phi}_p}{g_o} & 0 & 0 & \dot{\phi}_p \end{bmatrix}$$

2.4.4.8

and where $\dot{\phi} = \dot{\phi}_\tau + w \dot{\phi}_\zeta + x \dot{\phi}_\eta$

$\dot{\phi}_p = \dot{\phi}_\tau + w_p \dot{\phi}_\zeta + x_p \dot{\phi}_\eta$

We do not pursue the general case any further. Our interest will be confined to cases in which ϕ_ζ or $\phi_\eta = 0$. As in the previous section, we proceed under the assumption $\phi_\eta = 0$. Then the characteristic conditions are found to be:

$$\left[\left(\frac{\phi_\tau}{\phi_\zeta} + w \right)^2 - c_*^2 \right] \left[\left(\frac{\phi_\tau}{\phi_\zeta} + w_p \right)^2 - a_*^2 \right] = \lambda \left(\frac{1-\epsilon}{\epsilon} \right) \frac{c_*^2}{\rho_p} \left[\frac{\phi_\tau}{\phi_\zeta} + w \right]^2 \quad 2.4.4.9$$

$$\dot{\phi} = 0$$

2.4.4.10

$$\dot{\phi}_p = 0$$

2.4.4.11

which are formally identical with the one dimensional results¹⁶. We have used:

$$c_*^2 = c^2(\zeta_z^2 + \zeta_r^2)$$

$$a_*^2 = a^2(\zeta_z^2 + \zeta_r^2)$$

It is also clear why we have introduced the coefficient λ . When $\lambda = 0$, equation 2.4.4.9 factors and always has four real roots.

With the same choice of coordinates internal to the characteristic surface as we used in the previous section we may tabulate the members of the last column of the augmented matrix, ξ_i' , $i=1, \dots, 8$ as:

$$\begin{aligned}\xi_1' &= \xi_1 - [\epsilon w \rho_\alpha + \epsilon \rho \zeta_z u_\alpha + \epsilon \rho \zeta_r v_\alpha + \rho w \epsilon_\alpha] \\ &\quad - [\epsilon x \rho_\beta + \epsilon \rho \eta_z u_\beta + \epsilon \rho \eta_r v_\beta + \rho x \epsilon_\beta] \\ \xi_2' &= \xi_2 - [\epsilon \rho w u_\alpha + \epsilon g_o \zeta_z p_\alpha] - [\epsilon \rho x u_\beta + \epsilon g_o \eta_z p_\beta] \\ \xi_3' &= \xi_3 - [\epsilon \rho w v_\alpha + \epsilon g_o \zeta_r p_\alpha] - [\epsilon \rho x v_\beta + \epsilon g_o \eta_r p_\beta] \\ \xi_4' &= \xi_4 - w[p_\alpha - \frac{c^2}{g_o} \rho_\alpha] - x[p_\beta - \frac{c^2}{g_o} \rho_\beta] \\ \xi_5' &= \xi_5 - [w_p \epsilon_\alpha - (1-\epsilon) \zeta_z u_{p\alpha} - (1-\epsilon) \zeta_r v_{p\alpha}] \\ &\quad - [x_p \epsilon_\beta - (1-\epsilon) \eta_z u_{p\beta} - (1-\epsilon) \eta_r v_{p\beta}] \\ \xi_6' &= \xi_6 - [\lambda(1-\epsilon) g_o \zeta_z p_\alpha + (1-\epsilon) \rho_p w_p u_{p\alpha} + g_o \zeta_z \sigma_\alpha] \\ &\quad - [\lambda(1-\epsilon) g_o \eta_z p_\beta + (1-\epsilon) \rho_p x_p u_{p\beta} + g_o \zeta_z \sigma_\beta] \\ \xi_7' &= \xi_7 - [\lambda(1-\epsilon) g_o \zeta_r p_\alpha + (1-\epsilon) \rho_p w_p v_{p\alpha} + g_o \zeta_r \sigma_\alpha] \\ &\quad - [\lambda(1-\epsilon) g_o \eta_r p_\beta + (1-\epsilon) \rho_p x_p v_{p\beta} + g_o \eta_r \sigma_\beta] \\ \xi_8' &= \xi_8 - w_p [\sigma_\alpha + \frac{\rho_p a^2}{g_o} \epsilon_\alpha] - x_p [\sigma_\beta + \frac{\rho_p a^2}{g_o} \epsilon_\beta]\end{aligned}$$

In terms of these quantities we may express the conditions of compatibility corresponding to 2.4.4.10 and 2.4.4.11 in the simple forms:

$$\xi_4' = 0 \quad 2.4.4.12$$

$$\xi_8' = 0 \quad 2.4.4.13$$

The condition of compatibility corresponding to the acoustic characteristics of equation 2.4.4.10 has the form:

$$\begin{aligned} \rho \dot{\phi} \left[\xi_5' + \frac{\zeta_r \phi}{\rho_p \dot{\phi}_p} \left(\xi_7' - \frac{g_o \zeta_r \phi}{\dot{\phi}_p} \xi_8' \right) + \frac{\zeta_z \phi}{\rho_p \dot{\phi}_p} \left(\xi_6' - \frac{g_o \zeta_z \phi}{\dot{\phi}_p} \xi_8' \right) \right] \\ = \dot{\phi}_p \left[1 - \frac{a^2 \phi^2}{\dot{\phi}_p} \right] \left[\xi_1' + \frac{\varepsilon g_o}{c^2} \xi_4' - \frac{\zeta_z \phi}{\dot{\phi}} \xi_2' - \frac{\zeta_r \phi}{\dot{\phi}} \xi_3' \right] \end{aligned} \quad 2.4.4.14$$

In order to deduce results in a form suitable for our computational applications, we define:

$$\xi_1^* = \xi_1 - [\varepsilon x \rho_\eta + \varepsilon \rho \eta_z u_\eta + \varepsilon \rho \eta_r v_\eta + \rho x \varepsilon_\eta]$$

$$\xi_2^* = \xi_2 - [\varepsilon \rho x u_\eta + \varepsilon g_o \eta_z p_\eta]$$

$$\xi_3^* = \xi_3 - [\varepsilon \rho x v_\eta + \varepsilon g_o \eta_r p_\eta]$$

$$\xi_4^* = \xi_4 - x \left[p_\eta - \frac{c^2}{g_o} \rho_\eta \right]$$

$$\xi_5^* = \xi_5 - [x_p \varepsilon_\eta - (1-\varepsilon) \eta_z u_{p\eta} - (1-\varepsilon) \eta_r v_{p\eta}]$$

$$\xi_6^* = \xi_6 - [\lambda(1-\varepsilon) g_o \eta_z p_\eta + (1-\varepsilon) \rho_p x_p u_{p\eta} + g_o \eta_z \sigma_\eta]$$

$$\xi_7^* = \xi_7 - [\lambda(1-\varepsilon) g_o \eta_r p_\eta + (1-\varepsilon) \rho_p x_p v_{p\eta} + g_o \eta_r \sigma_\eta]$$

$$\xi_8^* = \xi_8 - x_p \left[\sigma_\eta + \frac{\rho_p a^2}{g_o} \varepsilon_\eta \right]$$

Next, we use 2.4.1.10 to recast 2.4.4.9 as:

$$\left[\left(\frac{d\zeta}{d\tau} - w\right)^2 - c_*^2\right] \left[\left(\frac{d\zeta}{d\tau} - w_p\right)^2 - a_*^2\right] = \lambda c_*^2 \frac{\rho}{\rho_p} \frac{1-\epsilon}{\epsilon} \left[\frac{d\zeta}{d\tau} - w\right]^2 \quad 2.4.4.15$$

Evidently, when $\lambda = 0$ this yields the roots:

$$\frac{d\zeta}{d\tau} = w \pm c_* \text{ and } \frac{d\zeta}{d\tau} = w_p \pm a_*$$

We introduce $y = \frac{d\zeta}{d\tau} - w$ 2.4.4.16

$$y_p = \frac{d\zeta}{d\tau} - w_p \quad 2.4.4.17$$

and, by reference to 2.4.4.14 we define:

$$\xi_A = \xi_1^* + \frac{\epsilon g_o}{c^2} \xi_4^* + \frac{\zeta_z}{y} \xi_2^* + \frac{\zeta_r}{y} \xi_3^* \quad 2.4.4.18$$

$$\xi_B = \xi_5^* - \frac{\zeta_r}{\rho_p y_p} (\xi_7^* + \frac{g_o \zeta_r}{y_p} \xi_8^*) - \frac{\zeta_z}{\rho_p y_p} (\xi_6^* + \frac{g_o \zeta_z}{y_p} \xi_8^*) \quad 2.4.4.19$$

It then follows, when $\lambda = 0$ and $\phi_\eta = 0$ and $y_p = \pm a_*$, corresponding to the solid phase acoustic characteristic, that 2.4.4.14 yields:

$$\sigma_\alpha = - \frac{\rho_p y_p}{g_o (1 + \frac{w}{y_p})} \left\{ \frac{\xi_B + (1-\epsilon) (1 + \frac{w}{y_p}) (\zeta_z u_{p\alpha} + \zeta_r v_{p\alpha})}{\zeta_r^2 + \zeta_z^2} \right\} \quad 2.4.4.20$$

Moreover, when we have simply $\phi_\eta = 0$ then 2.4.4.14 may be written as:

$$\begin{aligned}
 -\frac{\varepsilon g_o}{c^2} y p_\alpha &= \frac{-\xi_A}{1 + \frac{w}{y}} + \frac{\rho \xi_B y y_p}{(1 + \frac{w}{y})(y_p^2 - a_*^2)} \\
 &+ \frac{\rho y y_p (1-\varepsilon)(1 + \frac{w_p}{y_p})(\zeta_z u_{p\alpha} + \zeta_r v_{p\alpha})}{(1 + \frac{w}{y})(y_p^2 - a_*^2)} \\
 &+ \varepsilon \rho (\zeta_z u_\alpha + \zeta_r v_\alpha) + \frac{\frac{g_o \rho}{\rho_p} y (1 + \frac{w_p}{y_p})(\zeta_r^2 + \zeta_z^2)}{(1 + \frac{w}{y})(y_p^2 - a_*^2)} \sigma_\alpha \\
 &+ \rho y \frac{\frac{w}{y} - \frac{w_p}{y_p}}{1 + \frac{w}{y}} \varepsilon_\alpha
 \end{aligned} \tag{2.4.4.21}$$

We note that whereas 2.4.4.20 requires $\lambda = 0$, 2.4.4.21 does not. In practice, however, we will use $\lambda = 0$. Evidently 2.4.4.21 reduces to 2.4.4.20 when $y_p = \pm a_*$. We will use 2.4.4.20 to determine values of σ on the computational boundaries. Equation 2.4.4.21 will be used, with $y = \pm c$, corresponding to the gas phase acoustic characteristics, to determine values of p . We also note:

$$\sigma_\alpha = \sigma_\zeta + \sigma_\tau / \left(\frac{d\zeta}{d\tau} \right) \tag{2.4.4.22}$$

All the foregoing results were obtained subject to the assumption $\phi_\eta = 0$. The corresponding results for $\phi_\zeta = 0$ follow from considerations of symmetry.

3.0 TWO DIMENSIONAL CONVECTIVE FLAMESPREADING IN A CLOSED CHAMBER

From a consideration of the systems of balance equations presented in the preceding section it may be seen that a logical step in the development of a fully two dimensional interior ballistic code is the establishment of a technique for the numerical solution of the equations of two phase flow in a two dimensional, axisymmetric chamber. Techniques have been developed previously for one dimensional two phase flows in the full degree of generality required by our ultimate goal. In the present section we confine ourselves to the problem of convective flamespreading in a closed chamber, without ullage. Thus we are concerned, for the moment, only with impermeable stationary external boundaries and not at all with internal boundaries. However, we will consider the complications imposed by the detailed geometry of typical gun chambers, namely the hemispherical breech closure plug and the projectile intrusion due to the presence of a boattail. The manner of extension of the present techniques, in combination with those previously developed, will be discussed in chapter 4.0.

The method of solution for a single region of continuous two phase flow bounded by stationary impermeable walls is contained in section 3.1. Solutions generated with this method are presented in section 3.2.

3.1 Method of Integration

The present section has five subsections, reflecting five aspects of the task of numerical integration. In 3.1.1 we discuss the choice of coordinate transformation used to map the physical domain onto a unit square. In 3.1.2 we discuss the method of integration for interior mesh points and in 3.1.3 we discuss the treatment of points which lie on the boundaries. In section 3.1.4 we comment on the special treatment reserved for the boundary points which lie on the corners of the computational domain. Finally, in section 3.1.5 we note some numerical devices.

3.1.1 Coordinate Transformations

The physical domain has stationary boundaries in the present study. Accordingly, a single transformation is sufficient to map the physical domain once and for all onto a unit square. However, in subsequent work we will be confronted with the more general problem in which the boundaries are mobile and which therefore demands a time dependent mapping technique.

The approach taken here consists of two steps. Initially, we transform the arbitrarily configured physical domain onto a square by means of an equipotential map. Subsequently, we effect a solid phase Lagrangian transformation so that the mesh moves with the particles. This second step, which is not really required in the present study, is expected to provide the desired extension to the case in which the boundaries are mobile. It has, moreover, several benefits even in the present case. The troublesome convective terms in the solid phase balance equations¹⁸ vanish. Accordingly, the path of flamespreading is more sharply resolved due to the elimination of numerical diffusion in the solid phase thermal equation, 2.2.6.2.

Our approach to the first part of the coordinate transformation follows that of Thompson et al²⁹. The computational coordinates are embedded into an elliptic equation as follows:

$$\zeta_{zz} + \zeta_{rr} = 0 \quad 3.1.1.1$$

$$\eta_{zz} + \eta_{rr} = 0 \quad 3.1.1.2$$

It should be noted that as we have neglected the divergence terms, 3.1.1.1 and 3.1.1.2 do not express Laplace's equation in cylindrical coordinates.

We do not solve 3.1.1.1 and 3.1.1.2 directly. Rather, we solve the inverted system:

$$\alpha z_{\zeta\zeta} - 2\beta z_{\zeta\eta} + \gamma z_{\eta\eta} = 0 \quad 3.1.1.3$$

$$\alpha r_{\zeta\zeta} - 2\beta r_{\zeta\eta} + \gamma r_{\eta\eta} = 0 \quad 3.1.1.4$$

where

$$\alpha = z_{\eta}^2 + r_{\eta}^2$$

$$\beta = z_{\zeta} z_{\eta} + r_{\zeta} r_{\eta}$$

$$\gamma = z_{\zeta}^2 + r_{\zeta}^2$$

Thompson et al solved 3.1.1.3 and 3.1.1.4 subject to Dirichlet data on all boundaries. In effect, therefore, only the distribution of mesh points on the boundaries is required. The use of 3.1.1.3 and 3.1.1.4 produces a smoothly varying network of mesh lines on the interior. In order to solve 3.1.1.3 and 3.1.1.4, we replace all derivatives by second order differences. The resulting finite difference equations are solved using the method of successive over-relaxation⁵⁹.

In the present work, Dirichlet data are generated on each boundary by specifying the element as a string of straight line segments. Mesh points are always located on the ends of each segment. The interior of each segment is assigned mesh points at regularly spaced intervals. The number of points assigned to the interior of each segment may be prespecified. If the total number of points allocated to the boundary element is not exhausted by the foregoing criteria, the surplus is allocated so as to minimize the maximum physical mesh interval in the given boundary element.

⁵⁹. Roache, P.J. "Computational Fluid Dynamics"
Hermosa Publishers

In addition, we have encoded the capacity to apply Neumann data on any or all boundary segments to express the requirement that the mesh lines intercept the boundaries at right angles. Each of the four boundary elements may only have one of Dirichlet or Neumann data over each of its segments. Otherwise, the selection is arbitrary. When Neumann data are required only the segment end points are predetermined. Boundary values are chosen to satisfy the orthogonality condition as expressed by a second order one-sided difference formula after each sweep of the interior by the relaxation scheme.

3.1.2 Integration at Interior Mesh Points

The integration scheme used for interior mesh points is basically the MacCormack algorithm³⁰ with some refinements suggested by Moretti³¹. The basic algorithm of MacCormack, applied to the system:

$$\frac{\partial \psi}{\partial t} + B \frac{\partial \psi}{\partial \zeta} + C \frac{\partial \psi}{\partial \eta} = D \quad 3.1.2.1$$

may be expressed as a two-level scheme:

$$\begin{aligned} \tilde{\psi}_{i,j} = & \psi_{i,j}^n + [D_{i,j}^n - \frac{B_{i,j}^n}{\Delta \zeta} (\psi_{i+1,j}^n - \psi_{i,j}^n) \\ & - \frac{C_{i,j}^n}{\Delta \eta} (\psi_{i,j+1}^n - \psi_{i,j}^n)] \Delta t \end{aligned} \quad 3.1.2.2$$

$$\begin{aligned} \psi_{i,j}^{n+1} = & \frac{1}{2} (\psi_{i,j}^n + \tilde{\psi}_{i,j}) + [\tilde{D}_{i,j} - \frac{\tilde{B}_{i,j}}{\Delta \zeta} (\tilde{\psi}_{i,j} - \tilde{\psi}_{i-1,j}) \\ & - \frac{\tilde{C}_{i,j}}{\Delta \eta} (\tilde{\psi}_{i,j} - \tilde{\psi}_{i,j-1})] \frac{\Delta t}{2} \end{aligned} \quad 3.1.2.3$$

Thus alternating forward and backward differences are used for the representation of the spacewise derivatives.

The modification suggested by Moretti relates to the discretization of the convective derivatives. These are always represented by upstream differences as follows, except where forbidden by proximity to a boundary:

Predictor

$$\frac{\partial \phi}{\partial \zeta} = \pm \frac{1}{\Delta \zeta} [\phi_{i+1,j} - \phi_{i,j}] \quad 3.1.2.4$$

Corrector

$$\frac{\partial \phi}{\partial \zeta} = \pm \frac{1}{\Delta \zeta} [3\phi_{i+1,j} - \phi_{i+2,j} - 2\phi_{i,j}] \quad 3.1.2.5$$

The upper or lower sign is used according as the pre-multiplying velocity component is negative or positive respectively. It should be noted that 3.1.2.5 is not a second order accurate form. It only yields formal second order accuracy in combination with 3.1.2.4. When the mesh point is adjacent to a boundary and the rule expressed by 3.1.2.4, 3.1.2.5 would require data outside the computational domain, we revert to the regular MacCormack prescription.

We also note that the matrices B and C involve terms like ζ_z . These are deduced by first expressing z_ζ , z_η , r_ζ , r_η by means of centered differences. Then ζ_z , ζ_r , η_z , η_r follow from an elementary theorem of partial differentiation as:

$$\begin{aligned}\zeta_z &= r_\eta/J & \zeta_r &= -z_\eta/J \\ \eta_z &= -r_\zeta/J & \eta_r &= z_\zeta/J\end{aligned}\tag{3.1.2.6}$$

where $J = z_\zeta r_\eta - z_\eta r_\zeta$.

It was not found necessary, in the cases considered in the present study, either to time-split the non-homogeneous terms or to introduce implicitness for stability. However, we have incorporated an element of implicitness into the determination of the interphase drag. If we write $\vec{f}_s = (\vec{u} - \vec{u}_p)\phi(\vec{u} - \vec{u}_p)$ then the vectorial prefactor is represented implicitly in the term \vec{u} .

The integration scheme is assumed to be stable when subjected to a usual C-F-L domain of dependence limitation. If C is the fastest local wavespeed we require:

$$C \frac{\Delta t}{\Delta \zeta} \leq \frac{(r_\eta - k r_\zeta) z_\zeta + (z_\eta - k z_\zeta) r_\zeta}{\sqrt{(r_\eta - k r_\zeta)^2 + (z_\eta - k z_\zeta)^2}}\tag{3.1.2.7}$$

Where $k = \pm \Delta \zeta / \Delta \eta$ according as $z_\eta z_\zeta + r_\eta r_\zeta \gtrless 0$. In practice, we further constrain this heuristic limit by dividing it by a safety factor which we have taken to be 1.1.

3.1.3 Integration at Boundary Points

At the boundary points we use a variation by Moretti³¹ of a scheme apparently due to Kentzer³². The method is based on the characteristic forms of the balance equations. However, the characteristic forms are integrated explicitly using one sided differences for the spacewise derivatives. We describe first the computational sequence and subsequently the procedure of discretization.

Along a $\zeta = \text{constant}$ boundary we may combine the components of the gas phase momentum equation to yield a tangential equation:

$$\zeta_z v_\tau - \zeta_r u_\tau = \frac{\zeta_z \xi_3 - \zeta_r \xi_2}{\epsilon \rho} - \zeta_z x v_\eta + \zeta_r x u_\eta + \frac{g_o}{\rho} (\zeta_r \eta_z - \zeta_z \eta_r) p_\eta \quad 3.1.3.1$$

Equation 3.1.3.1 involves only τ - and η - derivatives of the state variables and may be marched forward according to the same prescription as we described in the preceding section on interior points. Then the application of the boundary condition, which requires the normal velocity component to vanish, yields updated values of u and v . A similar procedure is followed for the solid phase and, for both phases, on an $\eta = \text{constant}$ boundary.

Then, the rate of propagation of granular disturbances is computed. If it is zero, the porosity is updated directly from the solid phase continuity equation using one sided differences for the normal derivatives as prescribed by 3.1.2.4 and 3.1.2.5. If the rate of propagation is not zero, we use equation 2.4.4.20 to integrate σ and then ϵ follows from 2.4.4.13.

In any case, the pressure p follows from equation 2.4.4.21 and the density may then be determined from equation 2.4.4.12.

In discretizing the characteristic forms we use exactly the prescription of the previous section, on interior points, to evaluate all derivatives along the boundary. Except as noted in section 3.1.5, the normal spacewise derivatives are evaluated according to 3.1.2.4 and 3.1.2.5 with the sign chosen to ensure differencing inside the computational domain. The coordinate transformation derivatives are deduced using centered differences for the derivatives along the boundary and the usual second order one sided three point difference for the normal derivatives.

3.1.4 Integration at Corner Points

At the corners both the normal derivatives and the derivatives along the boundaries must be resolved in one-sided forms. Moreover, the definition of the normal direction is ambiguous as it may coincide with either of the intersecting coordinate lines. In the present study we have chosen the characteristic plane according to the structure of the flow near the boundary. The normal direction is chosen as either $\zeta - \tau$ or as $\eta - \tau$ according as:

$$|\zeta_z u_\zeta + \zeta_r v_\zeta| > |\eta_z u_\eta + \eta_r v_\eta|$$

Except as noted in the following section, equations 3.1.2.4 and 3.1.2.5 are used to discretize both the normal and the tangential spacewise derivatives of the state variables. The mesh transformation derivatives are deduced according to the usual second order accurate one sided difference formula.

3.1.5 Numerical Devices

The purpose of this section is to record certain details of the present method of solution which amount to ad hoc devices. Two topics are addressed. The first relates to the ignition of particles on the boundaries and the second relates to the representation of normal derivatives in the characteristic analysis.

We have noted previously in one dimensional studies¹⁸ that ignition can be significantly delayed for particles on impermeable boundaries where the slip velocity and hence the convective heating may vanish. Physically, flamespreading is continued to the boundary by different mechanisms than that expressed by our model. In our one dimensional work we simply extrapolated the flame trajectory to the boundary in order to estimate the ignition delay for particles on the boundary. In the present two dimensional study, an extrapolation of the path of flamespreading is difficult due to the geometrical factors. Moreover, in subsequent applications to bag charges we expect to deal with permeable boundaries for which the extended ignition delay does not arise. Accordingly, we have simply compared the surface temperature of a particle on the boundary with that of its neighbor in the interior and replaced it by the greater of the two values. Thus if there is significant convective heating due to a tangential flow, ignition of a boundary particle will follow in the natural manner. On the other hand, if the boundary corresponds to a stagnation region, the particle temperature follows that of its neighbor in the interior.

As described in section 3.1.3, the corrector step in the analysis of the boundary values involves a three point difference formula to provide overall second order formal accuracy. We have found that as the flamefront approaches the boundary, the three point formula provides less real accuracy than a uniformly first order scheme. The same effect has been noted in our one dimensional solutions¹⁸. Similar observations have been made in the context of highly structured single phase flow⁶⁰. Accordingly, we only use the three point corrector when ignition has occurred at the boundary point in question. During the pre-heat period we use the first order difference formula on both the predictor and the corrector steps.

3.2 Numerical Results

We now present numerical results for three problems. In the first two problems we assume that the projectile does not intrude into the combustion chamber. These serve as a baseline against which to consider the third problem in which the projectile is assumed to have a long boattail. The first two problems differ from one another only in respect to the law governing the intergranular stresses. In the first problem the stress is assumed to be reversible while, in the second, it is taken to be irreversible. The data bases for these solutions are presented in section 3.2.1. The solutions themselves are respectively discussed in sections 3.2.2 through 3.2.4.

⁶⁰. Abbett, M.J. "Boundary Condition Calculation Procedures for Inviscid Supersonic Flow Fields" Proc. 1st AIAA Comp. Fluid Dynamics Conf. 1973

3.2.1 Discussion of Data Bases

Figure 3.2.1.1 presents the boundary configurations and the initial mesh distributions for the zero intrusion projectile, discussed in sections 3.2.2 and 3.2.3, and for the long intrusion projectile, discussed in section 3.2.4. In both cases the mesh has been generated using Dirichlet data along each boundary element.

The mesh for the zero intrusion projectile involves 16 points in the axial direction and 7 in the radial direction. An overrelaxation coefficient of 1.6 was used to produce a mesh convergent to 1 part in 10^5 after 36 iterations. The 21×7 mesh used for the long intrusion projectile required 39 iterations to converge to the same precision. Notable features of the physical domain, in both cases, are the representation of the curvature of the breech and the taper of the tube. It is important to note that only the four corners defined by the intersections of the four boundary elements are treated explicitly in the calculation. Thus, in the case of the long intrusion projectile the corner defined by the termination of the boattail at the base is perceived implicitly by the numerical method as a point on a smooth and continuously differentiable boundary curve. Therefore, numerical diffusion is to be expected at this corner with a corresponding degradation of accuracy.

The thermophysical data used to determine the three solutions are presented in Table 3.2.1.1. The tabular representation of the igniter discharge is given in Table 3.2.1.2. Tables 3.2.1.3 and 3.2.1.4 respectively present the tabular data used to define the boundary elements for the zero intrusion and long intrusion cases.

It should be noted that the data bases are nominal in the sense that we do not attempt to simulate a specific in-service round. The purpose of these calculations is simply to enable us to appraise the operability of the numerical scheme.

Attention is drawn to Table 3.2.1.2. The distribution of the igniter venting function is seen to be quite localized, especially in the radial direction. As only seven points are used to resolve the radial structure of the flow we should not anticipate great accuracy in these solutions. However, problems of resolution concerning the igniter venting characteristics are not a concern in the present study. We intend, in subsequent work, to pose more properly the physical model of the center core igniter. Ultimately, it will be treated as a separate computational zone, linked to the behaviour of the two phase flow in the propelling charge by an explicit representation of the boundary separating the two zones.

Table 3.2.1.1 Thermophysical Properties Used in Two Dimensional Simulations

Initial Temperature (°K)	305.6
Initial Pressure (MPa)	0.1014
Initial Porosity (-)	0.5
Settling Porosity of Granular Bed (-)	0.5
Speed of Granular Compression Wave (m/sec)	442.
Speed of Granular Expansion Wave (m/sec)*	1270.
Density of Solid Phase (gm/cc)	1.6608
Thermal Conductivity (J/cm-sec-°K)	0.0016
Thermal Diffusivity (cm ² /sec)	0.0006
Ratio of Specific Heats (-)	1.25
Molecular weight (gm/gmol)	28.8
Covolume (cc/gm)	1.084
Ignition Temperature (°K)	488.9
Chemical Energy of Propellant (J/gm)	4982.
Burn Rate Additive Constant (cm/sec)	0.
Burn Rate Pre-Exponential Factor (cm/sec-MPa ⁿ)	0.25159
Burn Rate Exponent (-)	0.6
External Diameter of Grain (cm)	1.270
Length of Grain (cm)	2.54
Diameter of Perforations (cm)	0.127
Number of Perforations (-)	7
Energy of Igniter (J/gm)	3487

* Set equal to 442 m/sec for problem with reversible stress law

Table 3.2.1.2 Tabular Data Used to Define Igniter Discharge*

Rate of Discharge at 0 msec			
Radial Location (cm)	0	1.5	4.0
Axial Location (cm)			
0.	27.68	27.68	0
10.	27.68	27.68	0
20.	0	0	0

Rate of Discharge at 1 msec			
Radial Location (cm)	0	1.5	4.0
Axial Location (cm)			
0.	27.68	27.68	0
10.	27.68	27.68	0
20.	0	0	0

* Values linearly interpolated for arguments within table range.
 Discharge zero outside table argument range.

Table 3.2.1.3 Tabular Data Used to Define Geometry of Chamber with Zero Intrusion Projectile*

<u>Axial Position (cms)</u>	<u>Radial Position (cms)</u>
<u>Breech</u>	
3.0	0
3.0	4.5
2.5	6.0
1.5	7.5
0.	9.0
<u>Projectile Base</u>	
33.0	0.
33.0	8.
<u>Internal Boundary</u>	
3.0	0.
33.0	0.
<u>External Boundary</u>	
0.	9.0
33.0	8.0

* Points located on each boundary element by linear interpolation.

Table 3.2.1.4 Tabular Data Used to Define Geometry of Chamber with Long Intrusion Projectile*

<u>Axial Position (cms)</u>	<u>Radial Position (cms)</u>
<u>Breech</u>	
3.0	0.
3.0	4.5
2.5	6.0
1.5	7.5
0.	9.0
<u>Projectile Base</u>	
33.0	0.
33.0	4.0
45.0	8.0
<u>Internal Boundary</u>	
3.0	0.
33.0	0.
<u>External Boundary</u>	
0.	9.0
45.0	8.0

* Points located on each boundary element by linear interpolation.

3.2.2 Zero Intrusion Projectile with Reversible Granular Stress Law

Some aspects of this solution are depicted in figures 3.2.2.1 through 3.2.2.7. These are confined to some distributions of porosity and pressure at three times during the flamespreading process and the distribution of granular stress at the conclusion of flamespreading.

From the distribution of igniter venting given in Table 3.2.1.2 we anticipate the following sequence of physical events. As the rate of venting is quite vigorous, that part of the bed adjacent to the region of venting is subjected to intense convective heating from the initial instant. Therefore, ignition occurs very quickly around the venting region. The convective flame sweeps rapidly outward in the radial direction and induces ignition of the entire rear portion of the charge. The equilibration of pressure over the cross-section of the tube occurs faster than the forward spreading of the flame. The flow soon develops a one dimensional character, with the distribution of pressure resembling that of the NOVA code.

Figures 3.2.2.1, 3.2.2.2 and 3.2.2.3 present the distributions of porosity at three times. Flamespreading is complete by 1.0 msec, the latest time considered in these figures.

We note particularly the progressive rarefaction of the solid phase in the region of igniter blast due to the gas dynamic forces exerted by the expanding products of combustion. This rarefaction is, of course, balanced by a net compression in the outer regions. The degree of compaction is comparatively mild, due to the influence of the granular stress. In fact, the present problem is made relatively difficult from a computational point of view by the absence of an explicit treatment of ullage. The problem would be better posed, computationally as well as physically, if the igniter were taken to vent into the bed through a permeable boundary. In such a case, the region of rarefaction seen in figures 3.2.2.1 through 3.2.2.3 would be replaced by a separate computational zone and linked to the compacted bed by an explicitly represented internal boundary. This aspect of the solution will be present in all the three cases which we consider. We will, in the succeeding sections, look a little more closely at the evidence of numerical strain imposed by the requirement of capturing, with a coarse mesh, the interaction between the compression wave and the rarefaction wave in the solid phase.

Concerning the figures, we make the following general observations. They are all oblique views of the three dimensional surface formed by the state variable in question and the axial and radial coordinates. The axially directed lines are, in fact, contours of constant η while the radially directed lines constitute contours of constant ζ . Here ζ and η are the computational coordinates. The intersections of the two families define the mesh point values of the quantity in question. The contours are all drawn as straight line segments between successive pairs of mesh points and hidden lines are removed from the drawings. As the computational coordinates follow the motion of the solid phase, the mesh distortion can be inferred from these figures, particularly those for which the variable in question is essentially uniform. It should also be noted that the axial length scale is foreshortened relative to the radial length scale in all the figures.

Returning now to the specific results, we consider figures 3.2.2.4 through 3.2.2.7. We note the fully two dimensional nature of the flow at 0.2 msec as the flame is still in the process of spreading radially. By 0.4 msec, radial equilibration is nearly complete and by 1.0 msec. the pressure distribution has virtually no radial structure.

Figure 3.2.2.7 presents the distribution of granular stress at the conclusion of flamespreading. It, too, shows very little radial structure at this time.

We will explore more fully the radial structure of the remaining state variables in the two succeeding sections. Physically speaking, we are more interested in the cases in which the granular stress law is irreversible. We have now sufficient information about the present problem for our purpose, namely to provide a benchmark comparison with the next problem.

3.2.3 Zero Intrusion Projectile with Irreversible Granular Stress Law

The solution for this problem is represented by figures 3.2.3.1 through 3.2.3.33 and is therefore displayed in much greater detail than that of the preceding section.

We emphasize that the only physical difference between the present problem and that of the preceding section relates to the granular stress law. In the preceding section the unloading modulus was taken to be the same as the loading modulus. In the present section, as shown by Table 3.2.1.1, the unloading modulus, proportional to the square of the wave speed, is approximately ten times as great as the loading modulus.

Figure 3.2.3.1 presents the distribution of porosity following the completion of flamespreading at 1.0 msec. By comparison with figure 3.2.2.3 we see that the relative absence of elastic recovery in the present example results in somewhat greater rarefaction in the region directly influenced by the primer blast. Figure 3.2.3.2 presents the porosity at a still later time and shows even greater expansion. Indeed, the porosity is very nearly discontinuous at the leading edge of the granular rarefaction.

Figures 3.2.3.3 through 3.2.3.6 present distributions of pressure at various times. The first three of these may be compared with their counterparts in the previous section. Evidently, the change in the granular stress law has produced no qualitative changes in the pressure distributions and only minor quantitative differences are seen. Figure 3.2.3.6 shows that by 1.3 msec the pressure has completely equilibrated throughout the chamber in spite of the transient flamespreading process. This may be regarded as an indication of the high degree of mechanical dissipation present in the two phase flow. The figure also enables one to assess the total mesh distortion which takes place during flamespreading.

Thus far we have discussed flamespreading without providing any quantitative details of its history. In figures 3.2.3.7 through 3.2.3.11 we present the distributions of the surface temperature of the solid phase. The fully two dimensional flamespreading induced by the igniter blast is seen clearly in figures 3.2.3.7 and 3.2.3.8. By 0.3 msec, as shown in figure

3.2.3.9, flamespreading has a largely one dimensional character although the continuing venting of the igniter produces a somewhat greater rate of spreading at the centerline. This is also seen in figure 3.2.3.10. By 1.0 msec, as seen in figure 3.2.3.11, flamespreading is complete.

These figures indicate just how short the preheat or induction phase is at the leading edge of the flame. The surface temperature distribution essentially consists of two plateaux, the lower at ambient temperature and the higher at the ignition temperature. Actually, the upper surface is seen to depart slightly from an ideally uniform distribution. The departure is due to a slight overshoot of the temperature history during the time step corresponding to the ignition event at any given mesh point.

In figures 3.2.3.12 through 3.2.3.15, we consider the distributions of gas density at four times. These exhibit a pronounced entropy layer near the external and forward boundaries when the pressure distributions are also taken into account. The density at the external and forward boundaries, where ignition is delayed due to weak convection, is seen to be very much greater than that elsewhere in the chamber. In effect, the density at these boundaries results largely from an isentropic response to the pressure field. The temperature distribution is correspondingly depressed, as shown in figure 3.2.3.16. Of course, once ignition has occurred on the boundaries the density distribution tends to become more uniform as may be seen by comparing figures 3.2.3.14 and 3.2.3.15.

Figures 3.2.3.12 and 3.2.3.13 reveal the rather weak adiabatic precursor that runs ahead of the convective flame in the axial direction. It is also clear why upstream differencing of the convective terms is necessary for stability. The use of the standard MacCormack prescription for the convective terms is found to lead to negative values of the density at mesh points adjacent to the cool boundaries.

We turn now to some additional aspects of the behaviour of the solid phase, looking first at some distributions of granular stress and subsequently at the velocity components.

The distributions of granular stress are presented in figures 3.2.3.17 through 3.2.3.22. In all of these figures the granular stress is seen to vanish in the region of igniter venting where the porosity corresponds to dispersed flow. Figures 3.2.3.17 through 3.2.3.19 indicate that quite a strong radial compression is established by the igniter blast. Then, as the flame penetrates to the outside of the charge, the granular stress quickly unloads. By 0.6 msec, as shown in figure 3.2.3.20, we have an essentially one dimensional compression wave moving in the axial direction. The granular stress exerted on the base of the projectile is seen, in figure 3.2.3.21, eventually to rise to a value comparable to that experienced, much earlier, at the external boundary near the breech in figure 3.2.3.19. By 1.3 msec, figure 3.2.3.22, the granular stress has decayed strongly in the forward region. At this point the grains have rebounded somewhat and a mild level of stress is seen in the outer part of the breech.

In figure 3.2.3.22 we see, for the first time, an unsatisfactory level of numerical noise. This is due in part to the non-analytical character of the

granular stress law and also to the numerical strain imposed by the interaction of the reflected compression wave with the rarefaction in the region of igniter blast. We do not address the problem of alleviating these numerical wiggles in the present study. In the first place, they are associated with relatively low amplitudes of granular stress. In the second place, as we have already noted, subsequent studies will introduce an explicit internal discontinuity to separate the region of igniter venting from the compacted bed.

Some idea of the granular velocity field may be had by reference to figures 3.2.3.23 through 3.2.3.26. The maximum grain velocity appears to occur at the periphery of the region of igniter venting. We see that both the axial and radial components have maxima equal to 11 m/sec and that these maxima are virtually constant throughout flamespreading. Virtually no radial motion of the charge occurs forward of the region of igniter venting. The axial component is seen not to exceed 5 m/sec in this region at 0.6 msec and, by 1.0 msec, to be slightly negative as the axial compression wave is reflected from the base of the projectile.

We conclude our discussion of this solution by examining some distributions of the components of the gas velocity. The axial component is illustrated at two times in figures 3.2.3.27 and 3.2.3.28. These reveal no especially surprising features in view of the preceding discussion. The gas velocity is seen to have a value of approximately 220 m/sec at 0.6 msec. However, the maximum value has subsided to approximately 110 m/sec by 1.0 msec. The largest value of the axial component occurs shortly after the start of igniter venting and is approximately 270 m/sec or slightly more than that shown in figure 3.2.3.27.

The distributions of the radial component of the gas phase velocity are of somewhat greater interest, figures 3.2.3.29 through 3.2.3.33. At 0.2 msec, the maximum value of the radial component is approximately 270 m/sec which is the same as that for the axial component. By 0.6 msec, the maximum has already decreased to about 80 m/sec, by 1.0 msec to about 30 m/sec and by 1.3 msec to less than 10 m/sec. The rapid damping of the radial component of the gas velocity is in accord with our previous findings based on the solutions for cylindrical flow²⁶.

It is interesting to note, in figures 3.2.3.30 and 3.2.3.31, the existence of two maxima in the radial velocity distributions. The profile near the breech is associated with the venting of the igniter which is represented as continuing for 1 msec. The forward profile is apparently driven by the tendency of the convective flame to produce ignition somewhat earlier at the centerline than at the outside. Once the igniter venting is terminated the radial velocity distribution at the rear reverses itself. Gas now flows inward to supply the region attenuated by the igniter blast and which is accordingly deficient in terms of local gas generation. This is seen in figures 3.2.3.32 and 3.2.3.33. The forward profile disappears altogether once ignition of the bed is complete.

3.2.4 Long Intrusion Projectile

This problem differs from that of the preceding section in respect to the geometry of the projectile which is now taken to have a boattail which intrudes into the combustion chamber. Thus we introduce an added measure of geometrical complexity.

In many respects, however, the solution for the present problem resembles that of the preceding section. Therefore, we will not present as many details of the solution as we did in the preceding case. We will first provide some indications of the similarity of the two solutions and, subsequently, dwell on the differences. The present solution is represented by figures 3.2.4.1 through 3.2.4.21.

Figure 3.2.4.1 presents the distribution of porosity at 1.4 msec, following the conclusion of flamespreading. The additional delay to complete flamespreading is, of course, due to the extension of the chamber defined by the region around the boattail. We have, as in the preceding cases, a pronounced rarefaction in the region of igniter blast accompanied by a modest compression of the remainder of the charge.

Figures 3.2.4.2 through 3.2.4.5 present the distributions of pressure at four different times. These resemble, qualitatively, the results presented in the previous section. In particular we see that shortly after the conclusion of flamespreading, figure 3.2.4.5, the pressure is virtually uniform throughout the chamber, including the region around the boattail. Figure 3.2.4.5 also provides a clear indication of the total mesh distortion which occurs during flamespreading.

We note that there is no sign of numerical wiggles in the vicinity of the corner defined by the intersection of the boattail and the base of the projectile. The density and temperature of the gas are equally well behaved as indicated by figures 3.2.4.6 and 3.2.4.7. Of course, the pronounced entropy layer is still present although, due to the somewhat later time considered here, the effect is diminished at the external boundary.

Figures 3.2.4.8 through 3.2.4.11 illustrate the path of flamespreading. By 1.0 msec the entire portion of the charge to the rear of the base is fully ignited, in keeping with the finding of the previous section.

Distributions of granular stress are shown, at three times, in figures 3.2.4.12 through 3.2.4.14. The distribution at 0.3 msec is seen to be virtually the same as in the previous case, as one would expect. By 1.0 msec some differences are apparent as the stress becomes quite large in the region around the boattail. At 1.3 msec the stress in the corner defined by the intersection of the tube and the boattail reaches its maximum value of nearly 20 MPa. Subsequently, unloading occurs, partly as a consequence of wave reflection and partly due to combustion of the grains. We note that 20 MPa represents a rather large value of the average granular stress. Considering that the actual bearing surface to support the stress may be quite small, the localized values within the grains may be significantly higher than this value. Therefore the possibility of grain fracture ought not be overlooked.

We conclude by examining some of the distributions of the velocity components of each of the phases. The axial component of the gas velocity is shown in figures 3.2.4.15 through 3.2.4.17. Again, the distribution at 0.6 msec resembles closely that of the previous section, the gas being quiescent in the region around the boattail at this time. By 0.1 msec, the convection around the boattail has strengthened as the flame begins to penetrate that region. By 1.4 msec, however, the axial component of the gas phase velocity has subsided significantly and a weak backflow is apparently about to occur, near the breech, in the region rarefied by the igniter blast.

The corresponding distributions of the radial component of the gas phase velocity are shown in figures 3.2.4.18 through 3.2.4.20. The only noteworthy comment concerns the existence of a numerical wiggle in the corner defined by the tube and the boattail. This is probably due to the relatively coarse mesh spacing in that region, compounded by the delayed ignition. Once flamespreading is complete, the wiggle is seen to be much less pronounced, figure 3.2.4.20.

Finally, in figures 3.2.4.21 and 3.2.4.22 we present the distributions of the axial and radial components of the solid phase velocity. These have the expected correspondence with their counterparts of the preceding section.

4.0 CONCLUDING REMARKS

We have described the overall theoretical framework for a model of the two dimensional flow in a gun. The objective of the model being the analysis of longitudinal wave propagation, emphasis has been given to the precise numerical treatment of such potentially important aspects of the propelling charge as the location of ullage and of the influence of bag material.

As a step towards the complete numerical implementation of the model, we have encoded a method of solution of the equations of two dimensional heterogeneous reacting two phase flow and presented results for chamber geometries whose complexity is typical of what we expect to encounter in howitzer charges.

We now provide some comments on the extendability of the present methods to account for ullage and we indicate the next steps in the path of development of the code.

Regarding the extension of the present method to account for ullage, we comment successively on the overall approach to programming strategy, the influence of the gas permeable internal boundaries and the mapping techniques for the regions of ullage.

The strategy is a natural extension of that used previously in the development of the one dimensional model¹⁸. We assume the existence of two user supplied spatial resolution factors, one axial and one radial. Then a continuum representation is made of either the radial or the axial structure of a given region of the flow in accordance with a criterion which compares the extent of the region with that of the chamber as a whole. If the radial extent of the region exceeds the product of the radial resolution factor and the radius of the tube, a continuum representation is made of the radial structure of the flow and likewise for the axial structure. On this basis a given region can be determined as two dimensional, quasi-one-dimensional, or as lumped parameter.

The present method is well suited to the problem of the gas permeable internal boundary. The jump conditions may be differentiated along the path-line of the boundary to provide a system of partial differential equations which are updated explicitly in combination with the characteristic forms to yield new values of the state variables on both sides of the internal boundary.

As regards the mapping of the regions of ullage, new considerations arise only when the ullage is treated as a two dimensional region. However, the equipotential map is easily made time dependent so that no difficulty is anticipated in maintaining a suitable mesh distribution.

We conclude with some comments on the application of the code, in its present form, to the analysis of flamespreading in a charge for which the projectile intrusion is extremely large. Figure 4.1 presents two possible mesh distributions for the representation of a 105mm Howitzer with the XM622 projectile. The first distribution was generated by mapping the entire rear surface of the projectile, including afterbody and boattail onto one

side of the square computational domain. This approach is seen to provide very crowded mesh lines in the rear of the chamber while the resolution at the front is poor. Since the physical problem of interest relates to the possibility of large granular stress in the corner defined by the intersection of the boattail and the tube, this mesh is unsatisfactory.

The second mesh was generated by mapping only the boattail onto one side of the computational domain. The portion of the centerline between the breech and the base of the projectile together with the entire afterbody has been mapped onto the computational boundary normally thought of as the internal boundary. This is seen to provide a much better distribution of mesh points. As motion of the projectile is not considered, no difficulty arises from the apparent splitting of the physical boundary element.

However, it should be noted that a stagnation boundary condition is applied to both phases at the corners of the computational mesh and nowhere else. Accordingly, further attention will be required to the problem of posing correctly, within the macroscopic point of view, the boundary conditions at sharp internal edges of the type associated with projectiles having a long afterbody.

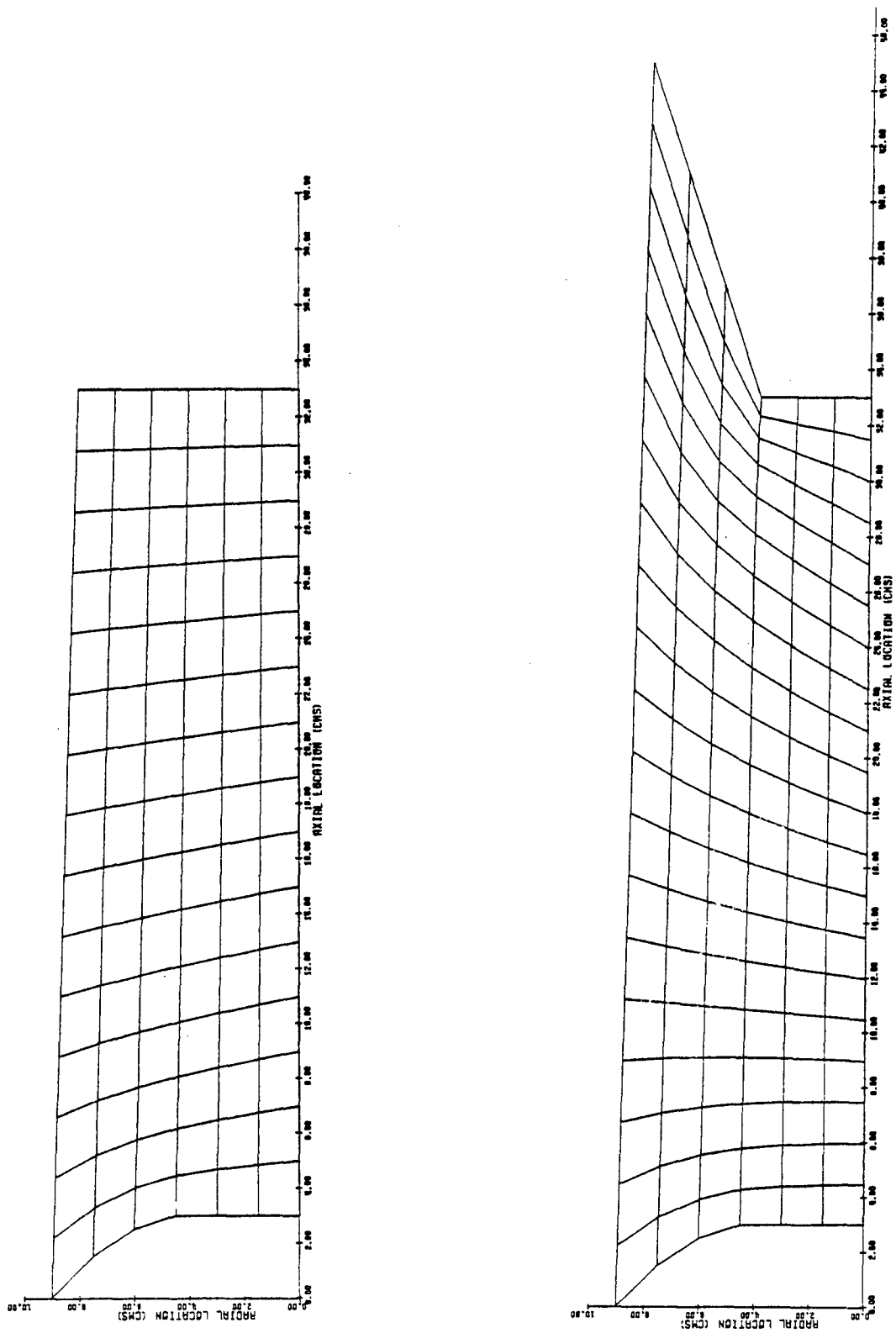


Fig. 3.2.1.1 Initial mesh distributions for simulation of zero intrusion and long intrusion projectiles

ZERO INTRUSION PROJECTILE
 REVERSIBLE STRESS LAW
 STEP 24

TIME (MSEC) 0.200

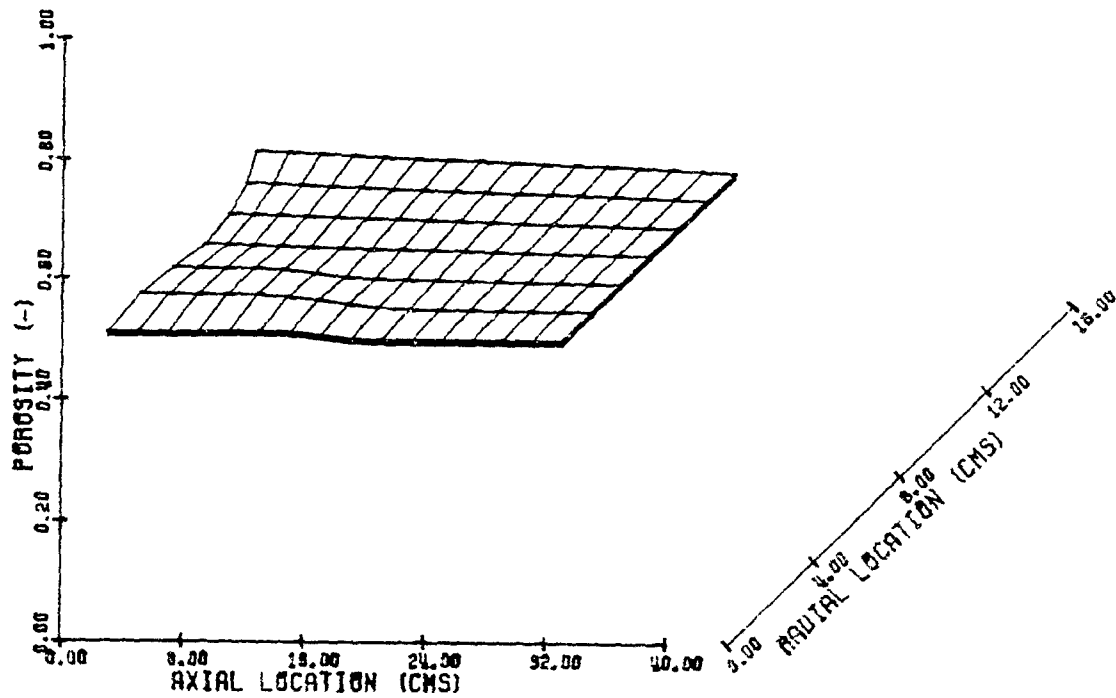


Fig. 3.2.2.1 Distribution of porosity at 0.2 msec in case of zero intrusion projectile with reversible granular stress law

ZERO INTRUSION PROJECTILE
REVERSIBLE STRESS LAW
STEP 52

TIME (MSEC) 0.400

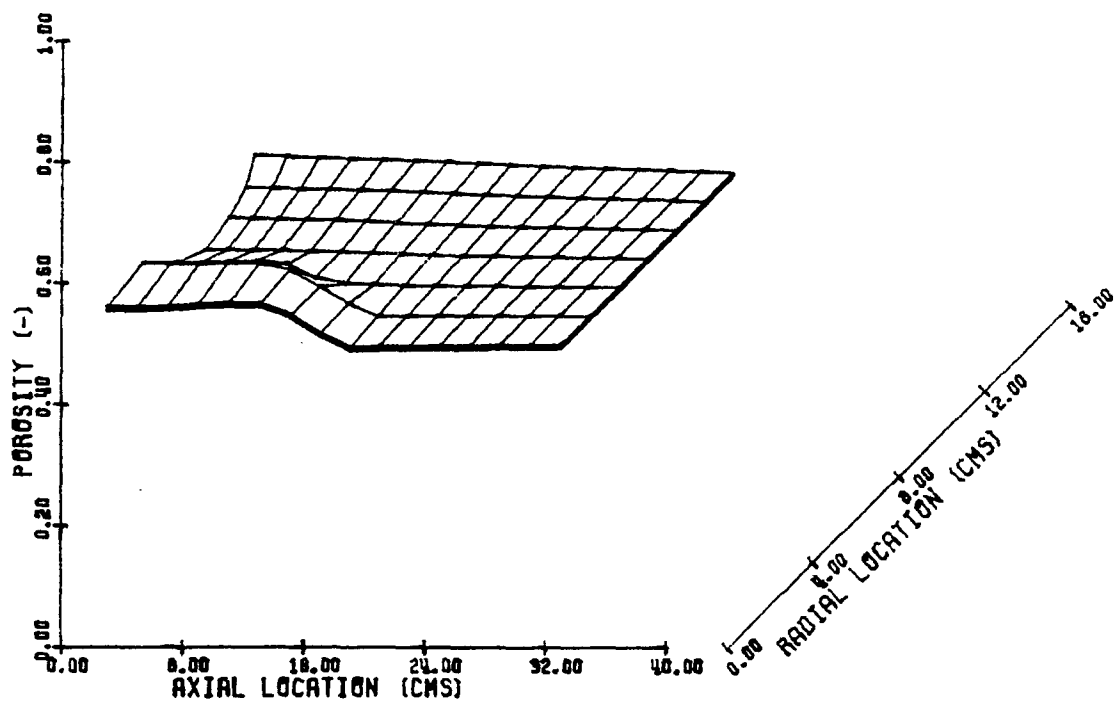


Fig. 3.2.2.2 Distribution of porosity at 0.4 msec in case of zero intrusion projectile with reversible granular stress law

ZERO INTRUSION PROJECTILE
REVERSIBLE STRESS LAW
STEP 134

TIME (MSEC) 1.000

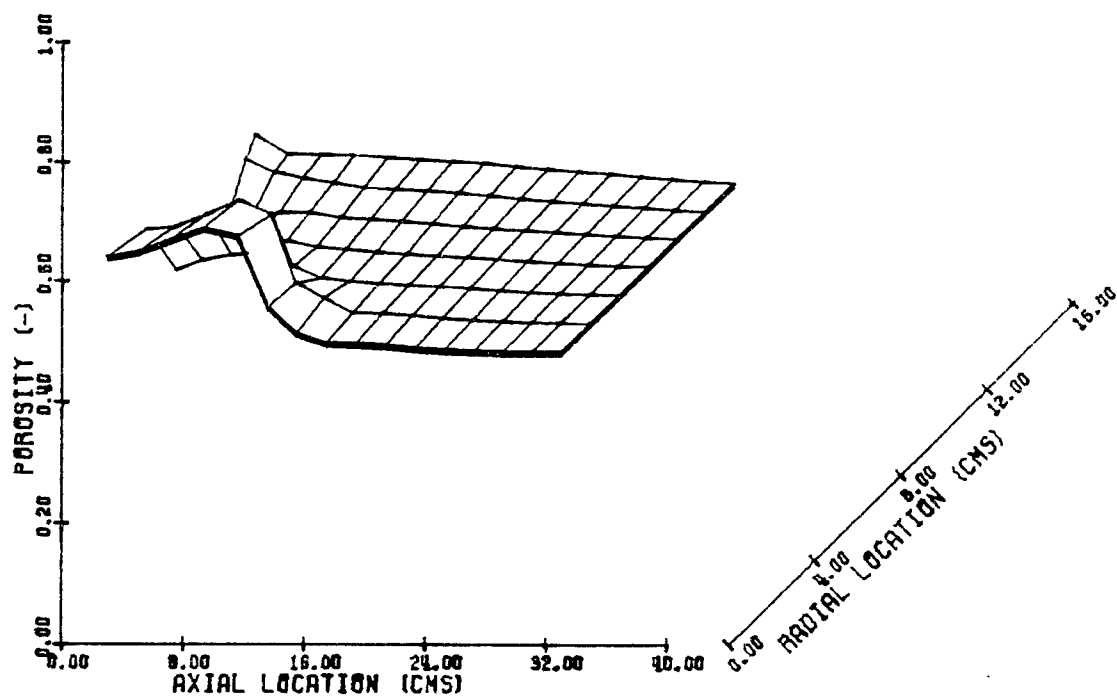


Fig. 3.2.2.3 Distribution of porosity at 1.0 msec in case of zero intrusion projectile with reversible granular stress law

ZERO INTRUSION PROJECTILE
 REVERSIBLE STRESS LAW
 STEP 24

TIME (MSEC) 0.200

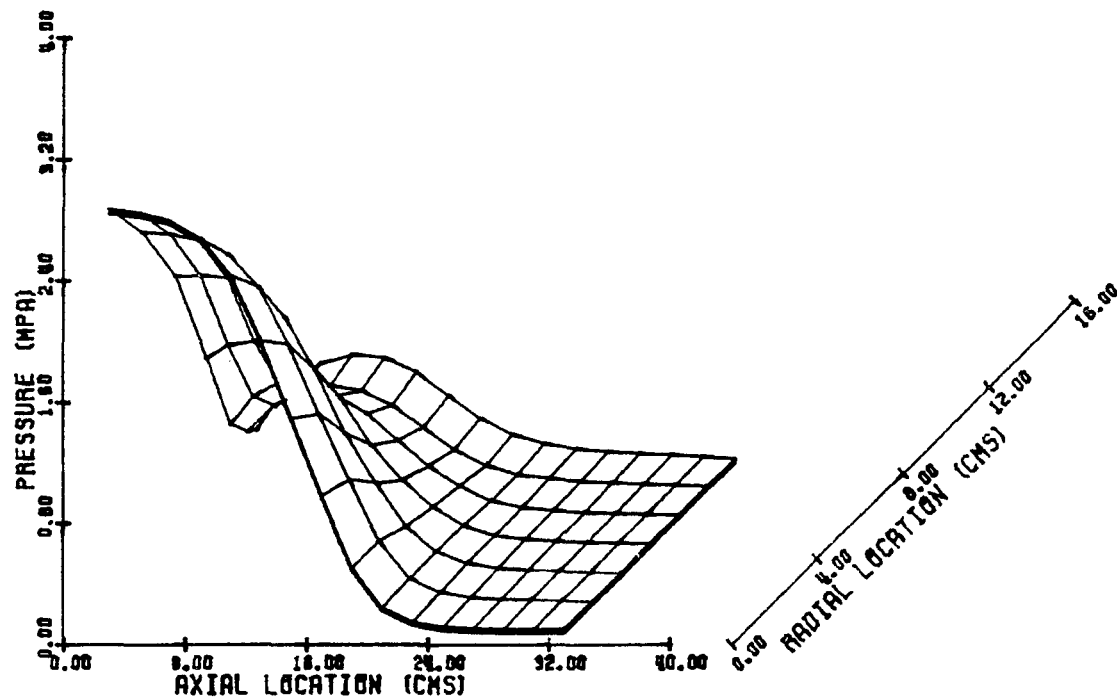


Fig. 3.2.2.4 Distribution of pressure at 0.2 msec in case of zero intrusion projectile with reversible granular stress law

ZERO INTRUSION PROJECTILE
 REVERSIBLE STRESS LAW
 STEP 52

TIME (MSEC) 0.400

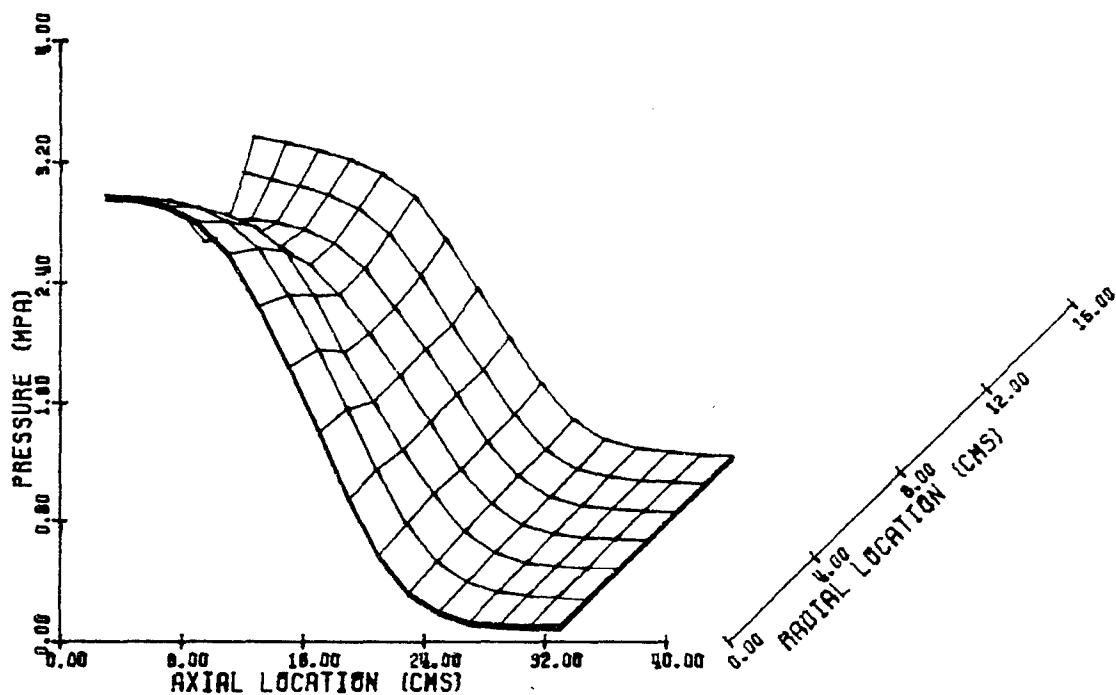


Fig. 3.2.2.5 Distribution of pressure at 0.4 msec in case of zero intrusion projectile with reversible granular stress law

ZERO INTRUSION PROJECTILE
REVERSIBLE STRESS LAW
STEP 194

TIME (MSEC) 1.000

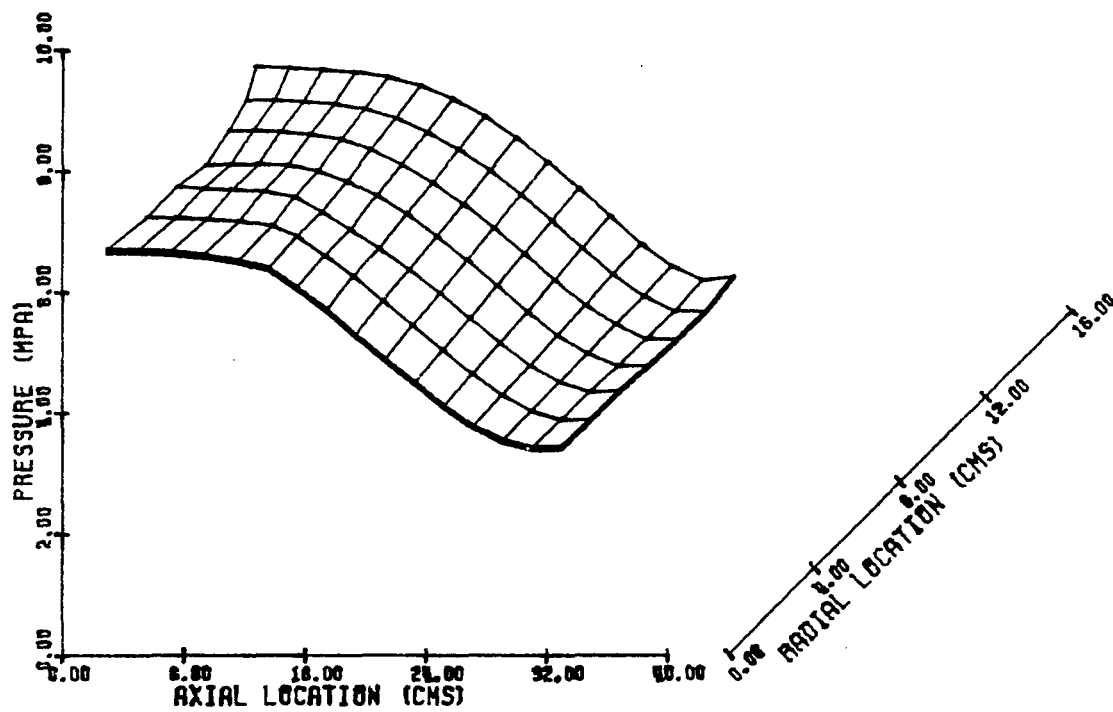


Fig. 3.2.2.6 Distribution of pressure at 1.0 msec in case of zero intrusion projectile with reversible granular stress law

ZERO INTRUSION PROJECTILE
REVERSIBLE STRESS LAW
STEP 134

TIME (MSEC) 1.000

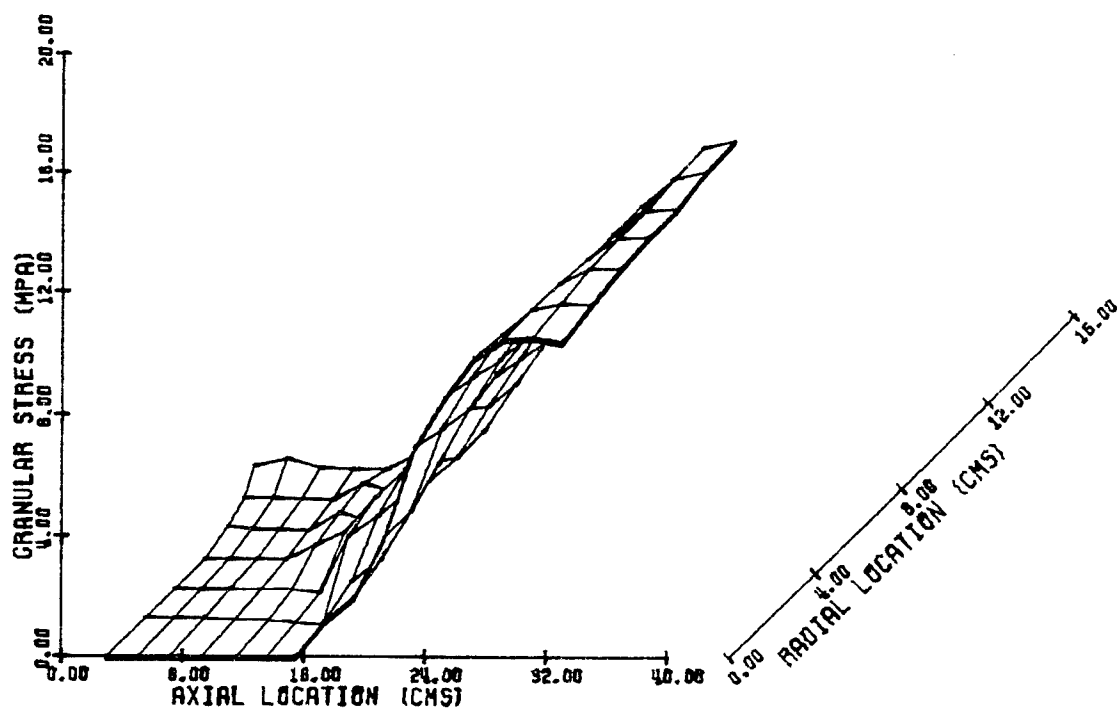


Fig. 3.2.2.7 Distribution of granular stress at 1.0 msec in case of zero intrusion projectile with reversible granular stress law

ZERO INTRUSION PROJECTILE
 IRREVERSIBLE STRESS LAW
 STEP 148

TIME (MSEC) 1.000

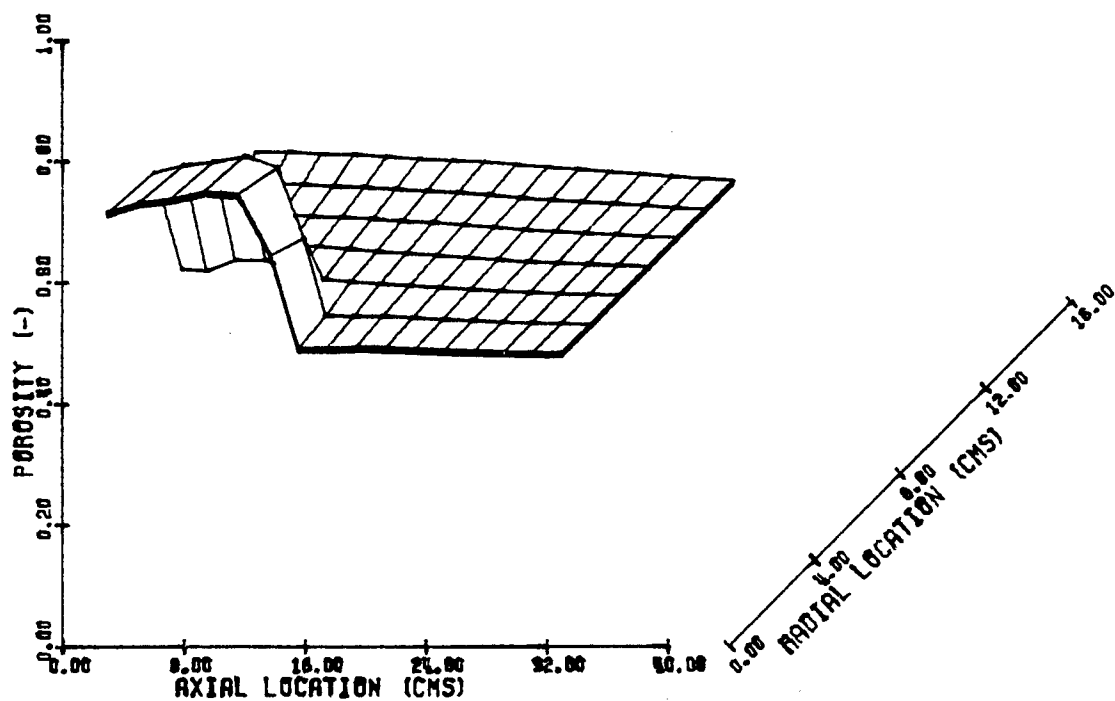


Fig. 3.2.3.1 Distribution of porosity at 1.0 msec in case of zero
 intrusion projectile with irreversible granular
 stress law

ZERO INTRUSION PROJECTILE
 IRREVERSIBLE STRESS LAW
 STEP 194

TIME (MSEC) 1.300

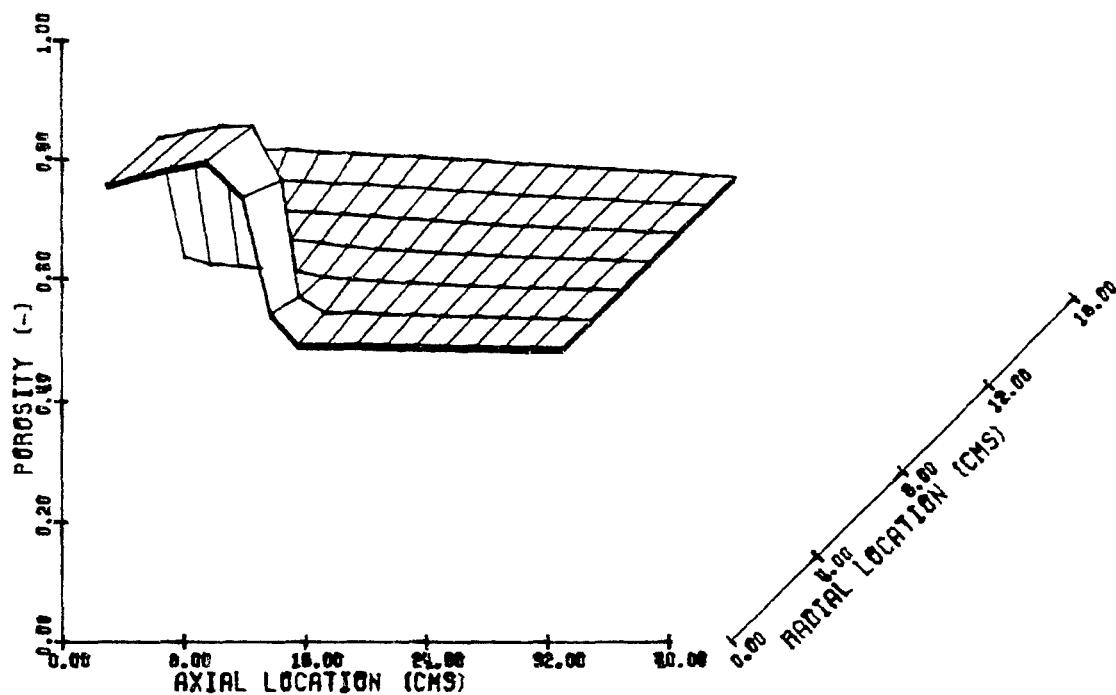


Fig. 3.2.3.2 Distribution of porosity at 1.3 msec in case of zero intrusion projectile with irreversible granular stress law

ZERO INTRUSION PROJECTILE
 IRREVERSIBLE STRESS LAW
 STEP 28

TIME (MSEC) 0.200

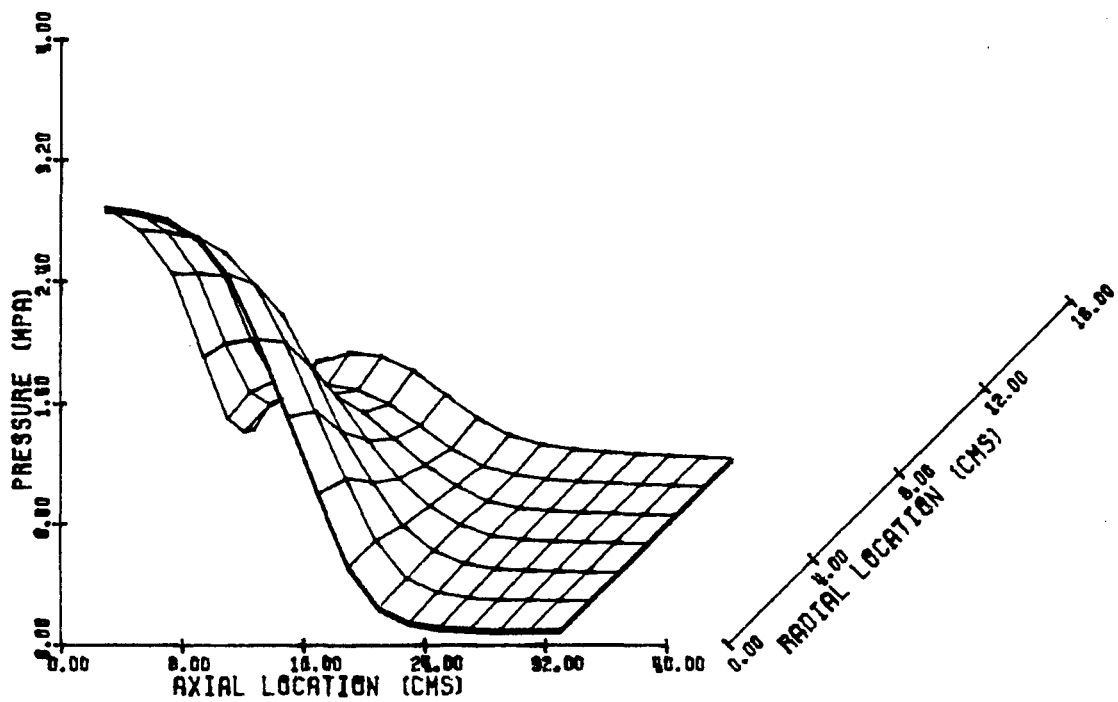


Fig. 3.2.3.3 Distribution of pressure at 0.2 msec in case of zero intrusion projectile with irreversible granular stress law

ZERO INTRUSION PROJECTILE

IRREVERSIBLE STRESS LAW

STEP 57

TIME (MSEC) 0.400

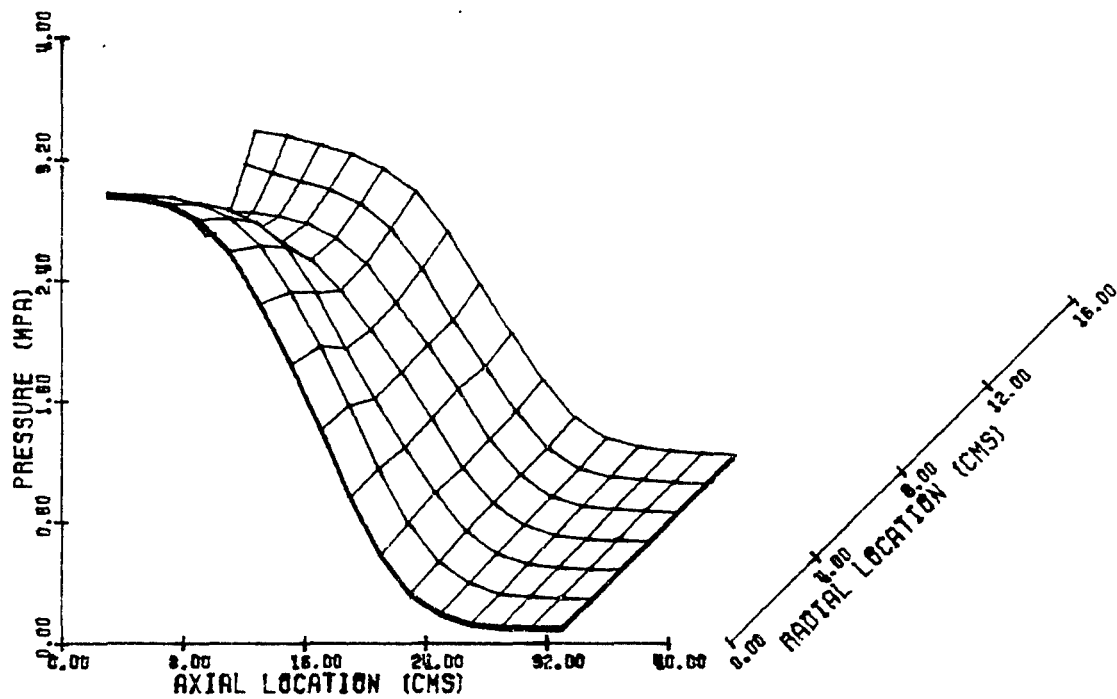


Fig. 3.2.3.4 Distribution of pressure at 0.4 msec in case of zero intrusion projectile with irreversible granular stress law

ZERO INTRUSION PROJECTILE
 IRREVERSIBLE STRESS LAW
 STEP 148

TIME (MSEC) 1.000

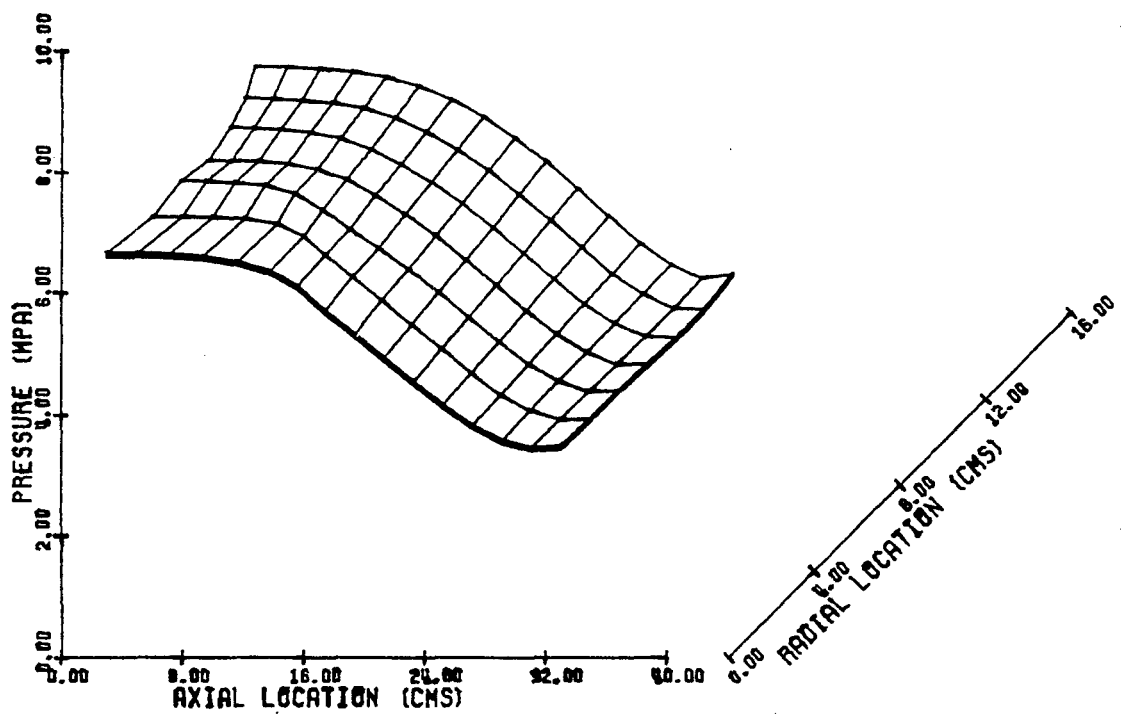


Fig. 3.2.3.5 Distribution of pressure at 1.0 msec in case of zero intrusion projectile with irreversible granular stress law

ZERO INTRUSION PROJECTILE
 IRREVERSIBLE STRESS LAW
 STEP 194

TIME (MSEC) 1.300

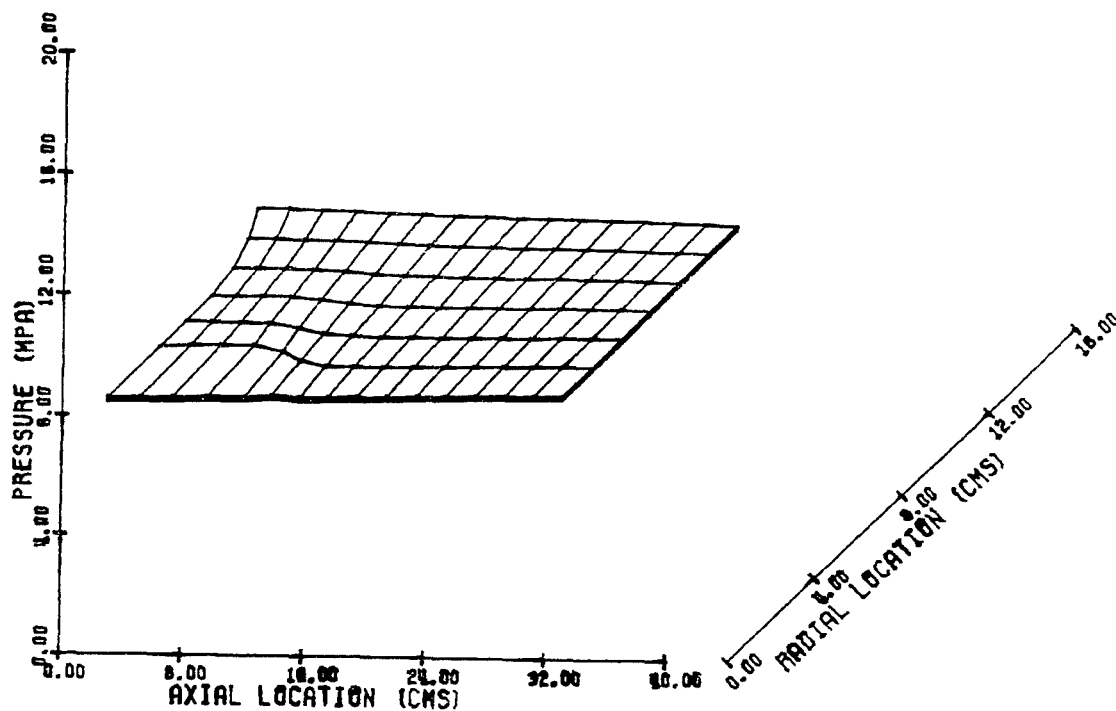


Fig. 3.2.3.6 Distribution of pressure at 1.3 msec in case of zero
 intrusion projectile with irreversible granular
 stress law

ZERO INTRUSION PROJECTILE
 IRREVERSIBLE STRESS LAW
 STEP 14

TIME (MSEC) 0.100

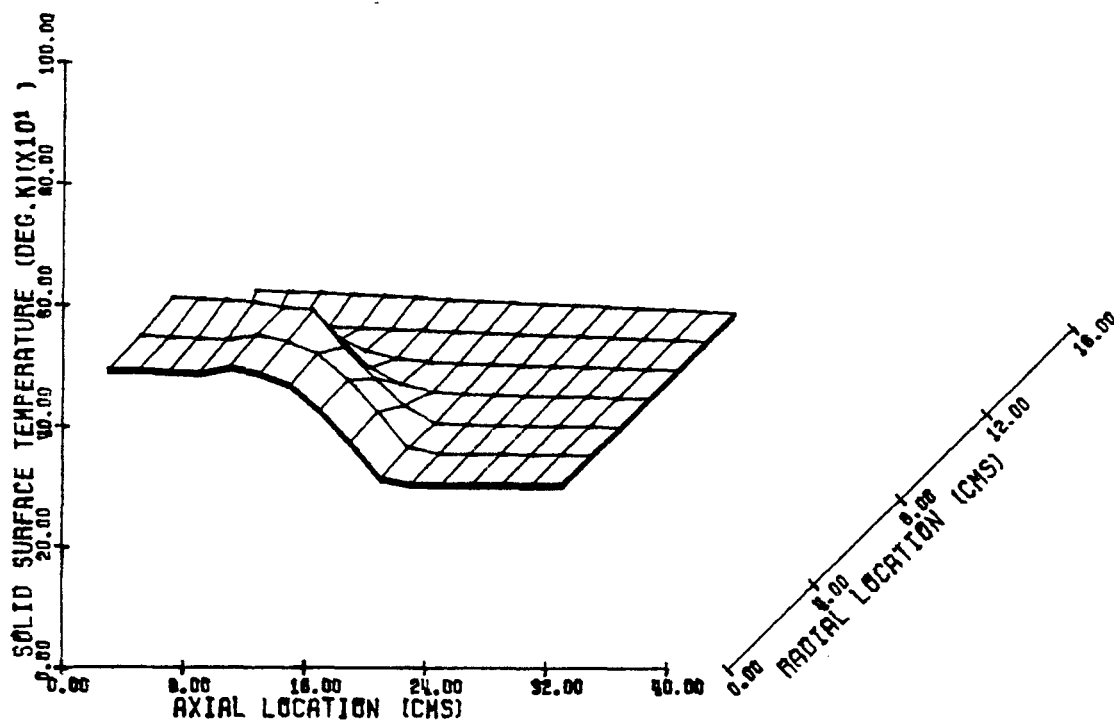


Fig. 3.2.3.7 Distribution of solid phase surface temperature at 0.1 msec in case of zero intrusion projectile with irreversible granular stress law

ZERO INTRUSION PROJECTILE
 IRREVERSIBLE STRESS LAW
 STEP 28

TIME (MSEC) 0.200

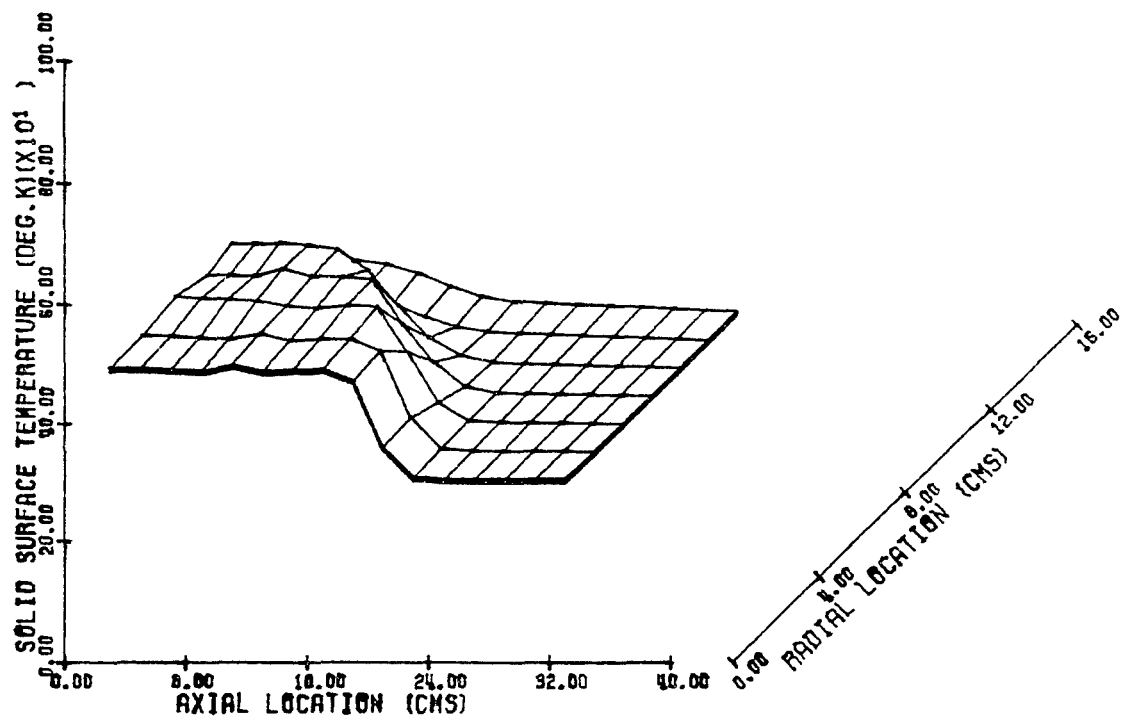


Fig. 3.2.3.8 Distribution of solid phase surface temperature at 0.2 msec in case of zero intrusion projectile with irreversible granular stress law

ZERO INTRUSION PROJECTILE
 IRREVERSIBLE STRESS LAW
 STEP 42

TIME (MSEC) 0.900

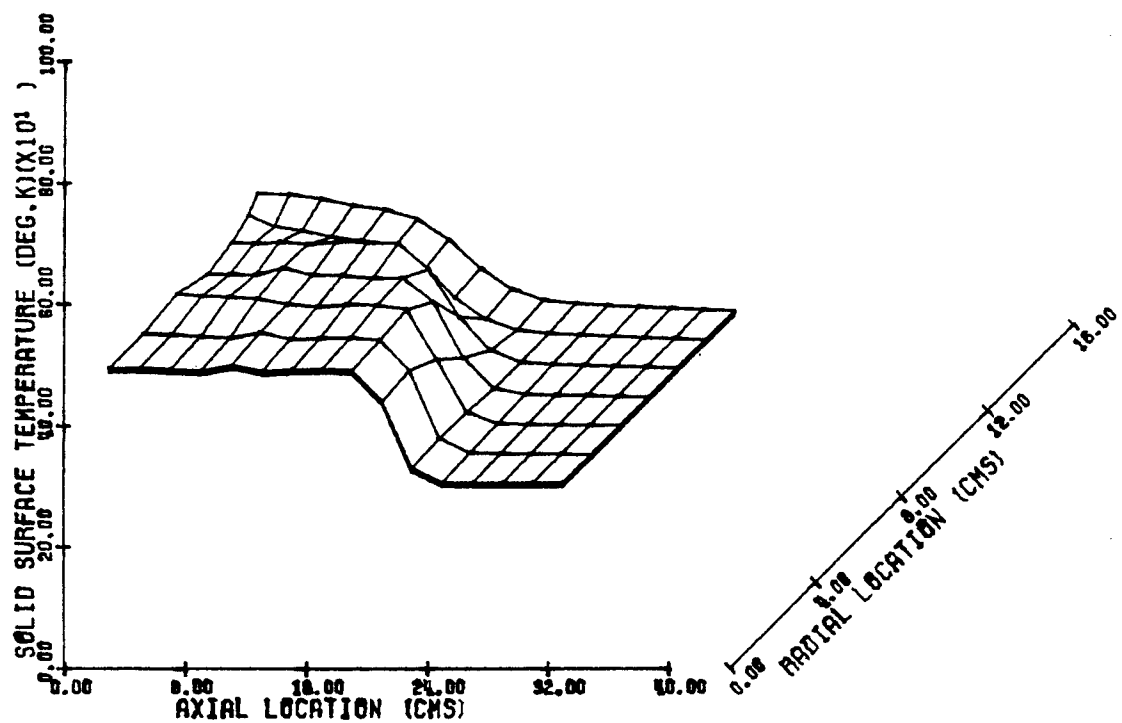


Fig. 3.2.3.9 Distribution of solid phase surface temperature at 0.3 msec in case of zero intrusion projectile with irreversible granular stress law

ZERO INTRUSION PROJECTILE
 IRREVERSIBLE STRESS LAW
 STEP 57

TIME (MSEC) 0.400

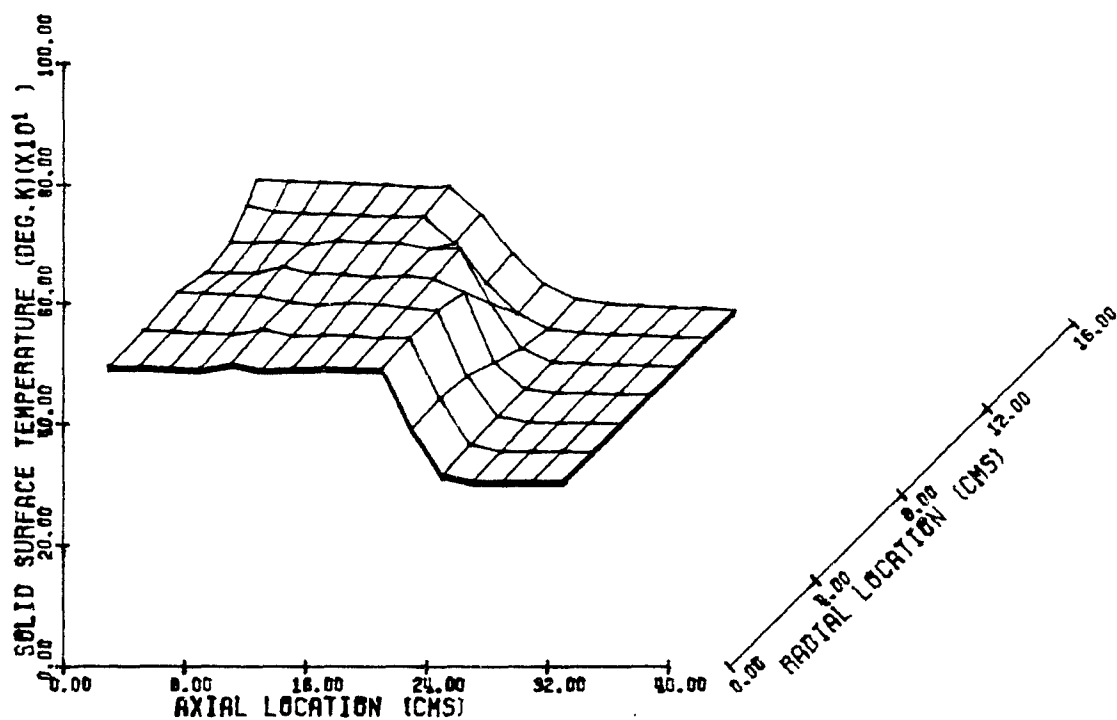


Fig. 3.2.3.10 Distribution of solid phase surface temperature at 0.4 msec in case of zero intrusion projectile with irreversible granular stress law

ZERO INTRUSION PROJECTILE
 IRREVERSIBLE STRESS LAW
 STEP 148

TIME (MSEC) 1.000

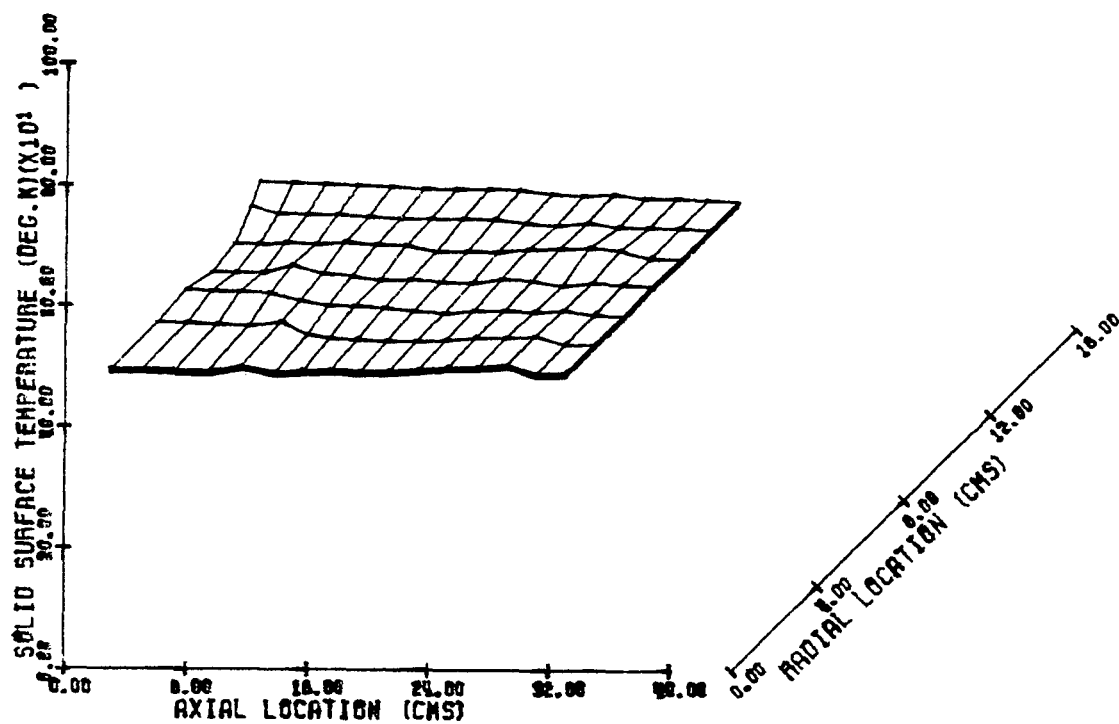


Fig. 3.2.3.11 Distribution of solid phase surface temperature at 1.0 msec in case of zero intrusion projectile with irreversible granular stress law

ZERO INTRUSION PROJECTILE
 IRREVERSIBLE STRESS LAW
 STEP 20

TIME (MSEC) 0.200

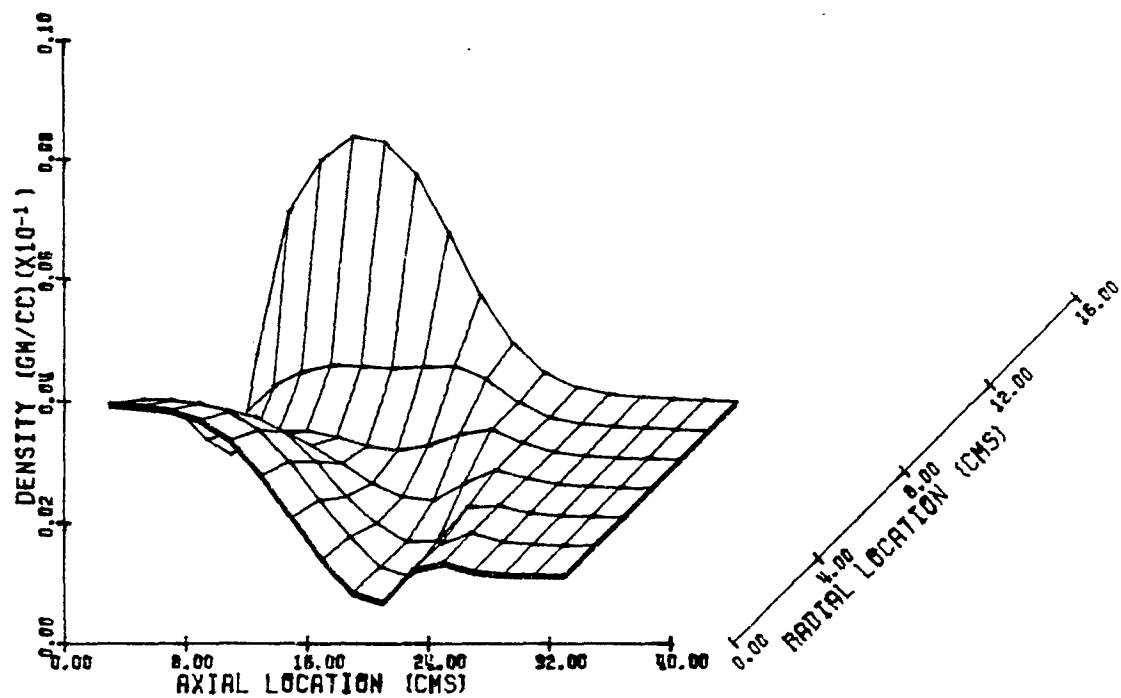


Fig. 3.2.3.12 Distribution of density of gas at 0.2 msec in case of zero intrusion projectile with irreversible granular stress law

ZERO INTRUSION PROJECTILE
 IRREVERSIBLE STRESS LAW
 STEP 57

TIME (MSEC) 0.400

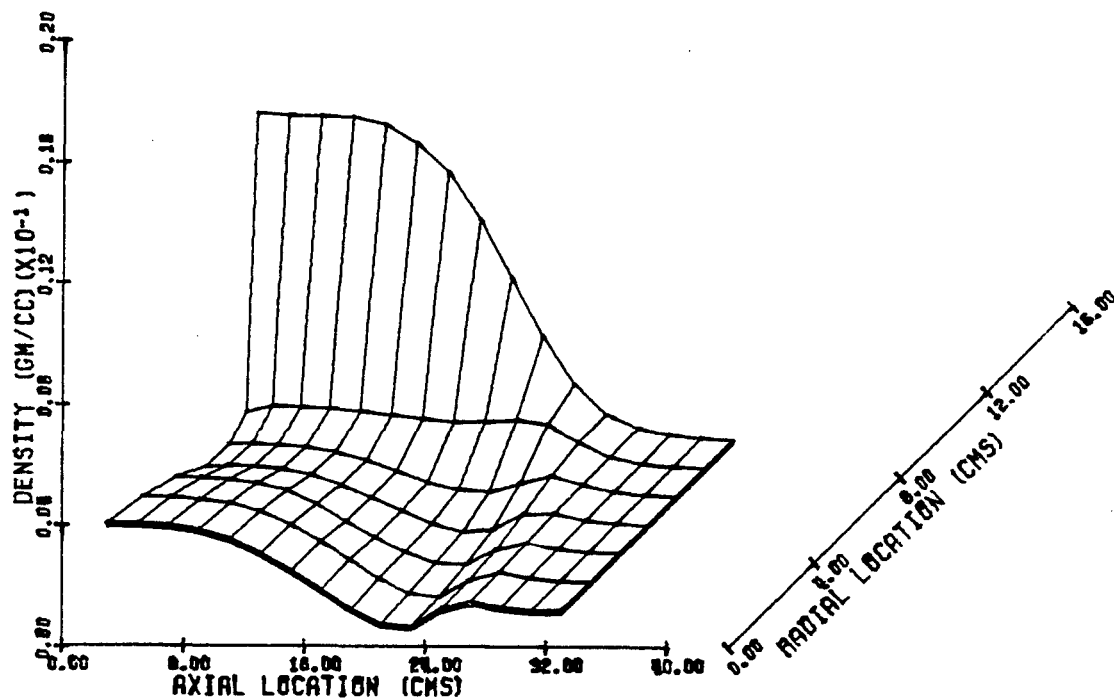


Fig. 3.2.3.13 Distribution of density of gas at 0.4 msec in case of zero intrusion projectile with irreversible granular stress law

ZERO INTRUSION PROJECTILE
 IRREVERSIBLE STRESS LAW
 STEP 148

TIME (MSEC) 1.000

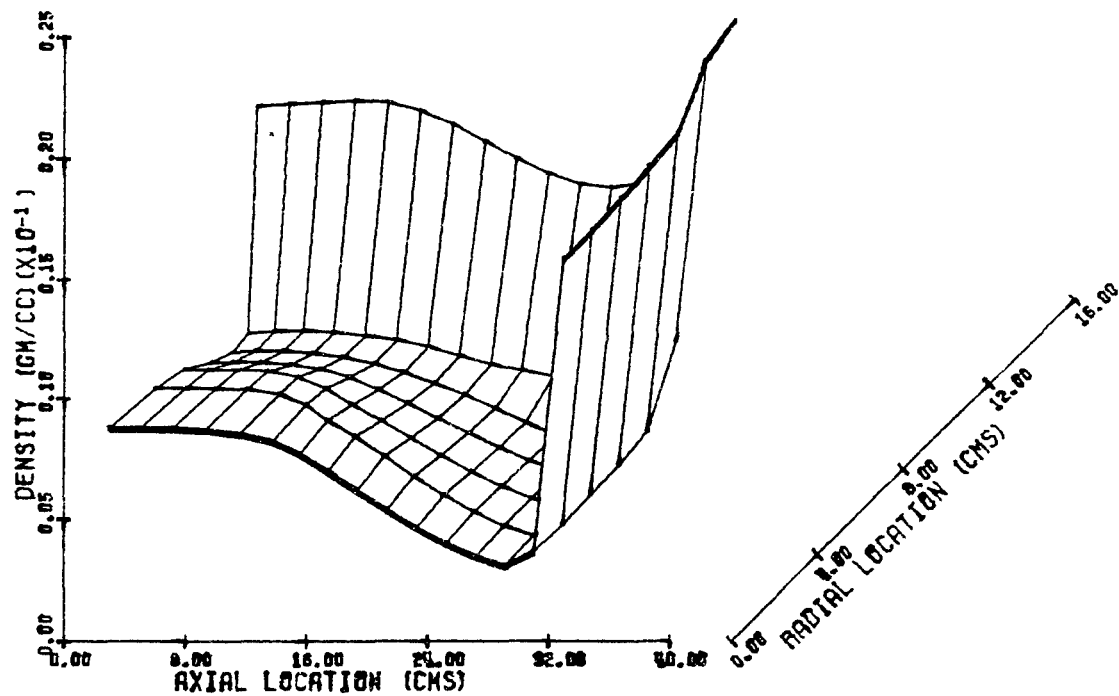


Fig. 3.2.3.14 Distribution of density of gas at 1.0 msec in case of zero intrusion projectile with irreversible granular stress law

ZERO INTRUSION PROJECTILE
 IRREVERSIBLE STRESS LAW
 STEP 194

TIME (MSEC) 1.300

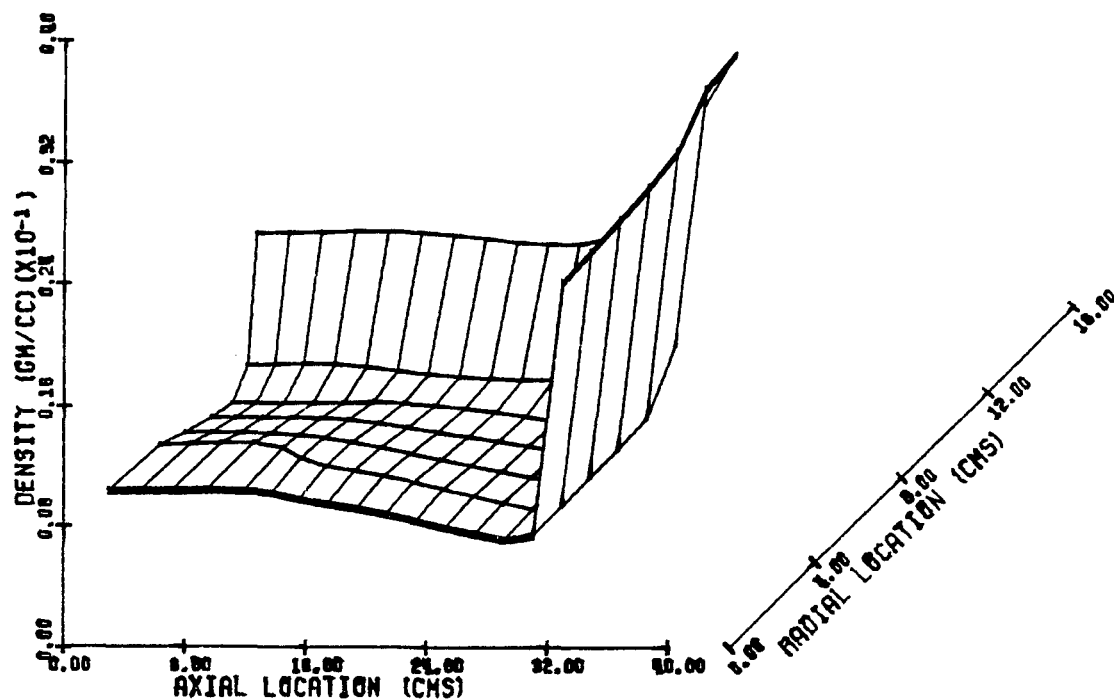


Fig. 3.2.3.15 Distribution of density of gas at 1.3 msec in case of zero intrusion projectile with irreversible granular stress law

ZERO INTRUSION PROJECTILE
 IRREVERSIBLE STRESS LAW
 STEP 194

TIME (MSEC) 1.300

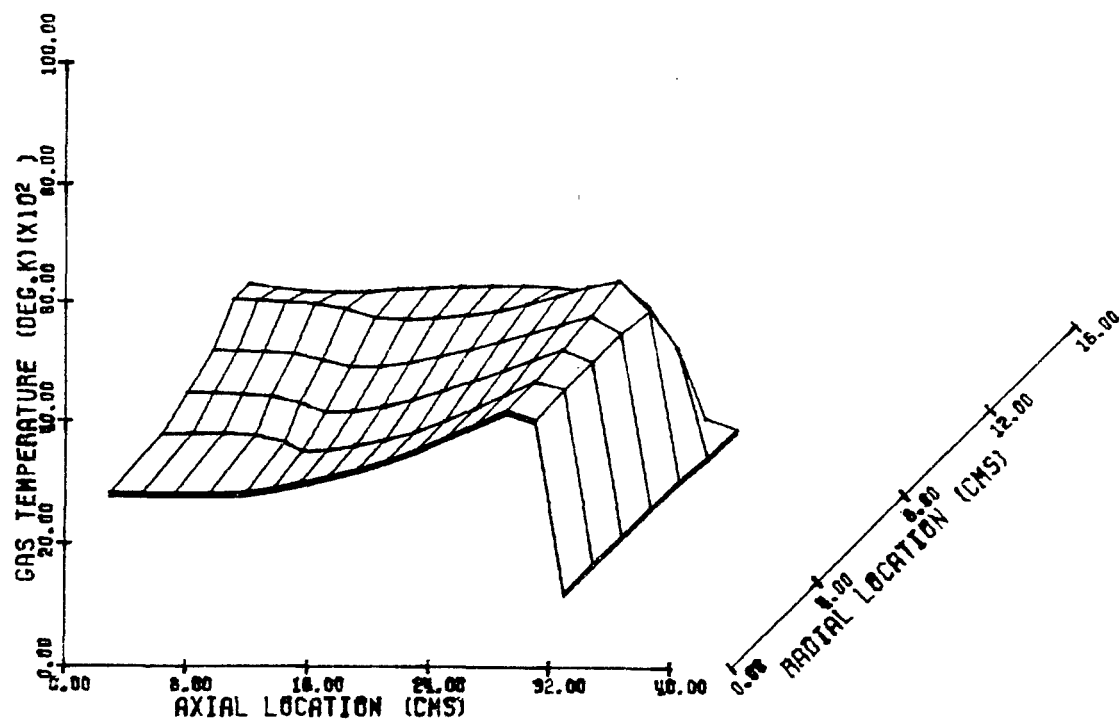


Fig. 3.2.3.16 Distribution of temperature of gas at 1.3 msec in case of zero intrusion projectile with irreversible granular stress law

ZERO INTRUSION PROJECTILE
 IRREVERSIBLE STRESS LAW
 STEP 14

TIME (MSEC) 0.100

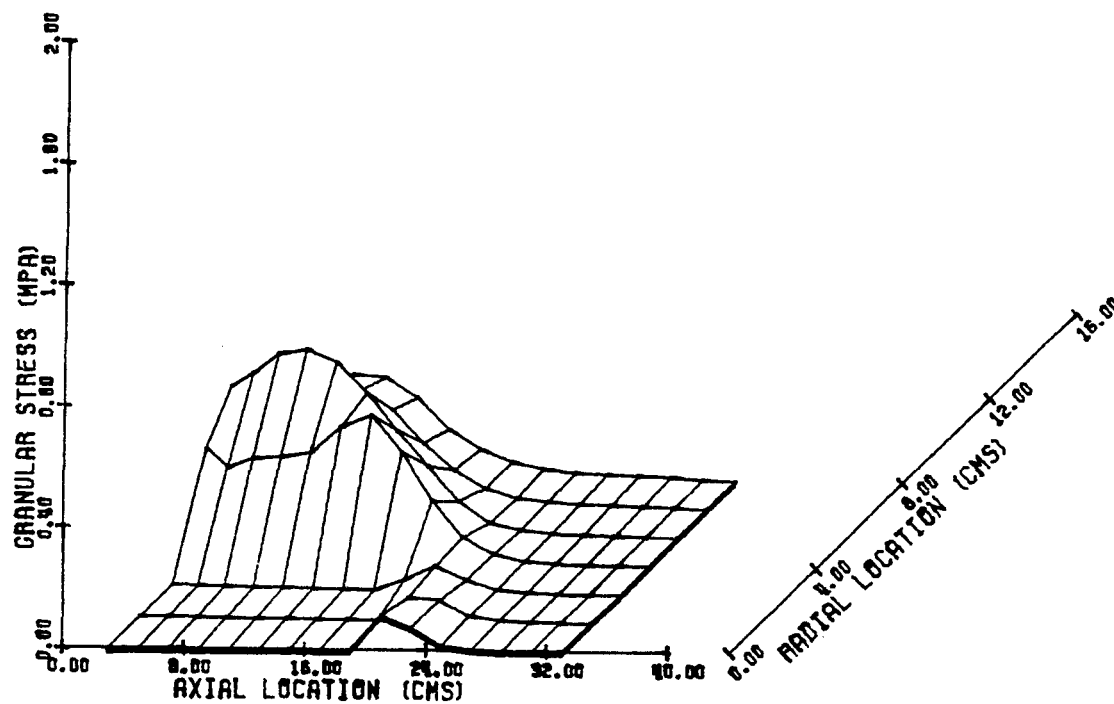


Fig. 3.2.3.17 Distribution of granular stress at 0.1 msec in case of zero intrusion projectile with irreversible granular stress law

ZERO INTRUSION PROJECTILE
IRREVERSIBLE STRESS LAW
STEP 28

TIME (MSEC) 0.200

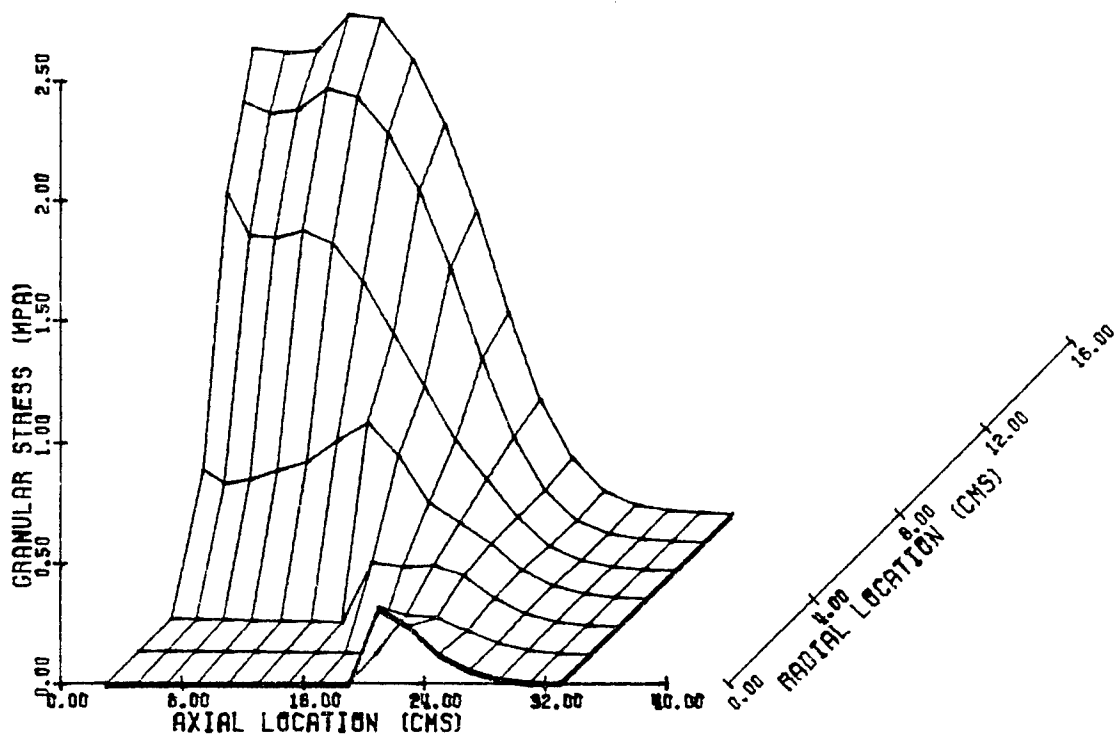


Fig. 3.2.3.18 Distribution of granular stress at 0.2 msec in case of zero intrusion projectile with irreversible granular stress law

ZERO INTRUSION PROJECTILE
 IRREVERSIBLE STRESS LAW
 STEP 42

TIME (MSEC) 0.300

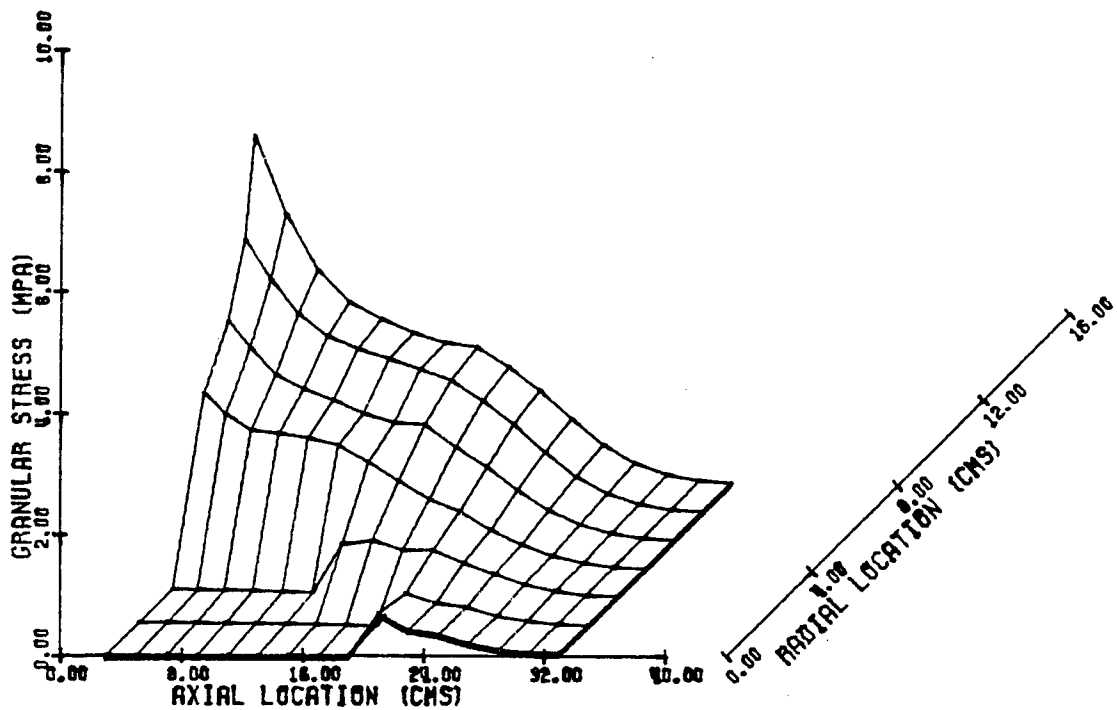


Fig. 3.2.3.19 Distribution of granular stress at 0.3 msec in case of zero intrusion projectile with irreversible granular stress law

ZERO INTRUSION PROJECTILE
 IRREVERSIBLE STRESS LAW
 STEP 87

TIME (MSEC) 0.600

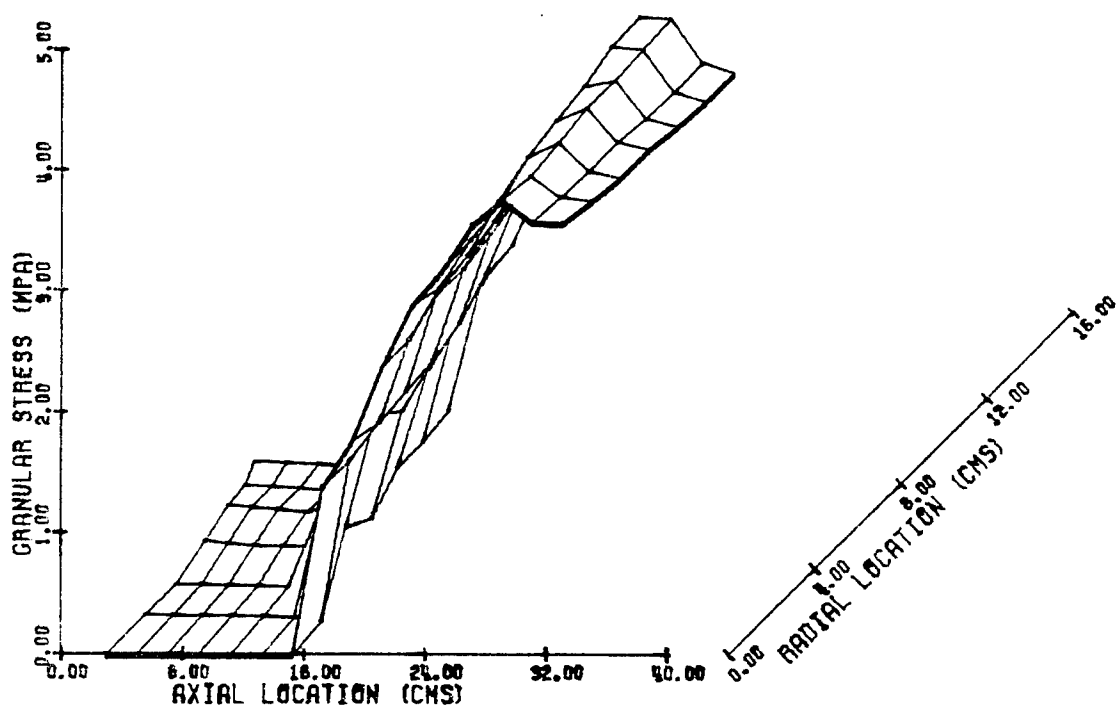


Fig. 3.2.3.20 Distribution of granular stress at 0.6 msec in case of zero intrusion projectile with irreversible granular stress law

ZERO INTRUSION PROJECTILE
 IRREVERSIBLE STRESS LAW
 STEP 140

TIME (MSEC) 1.000

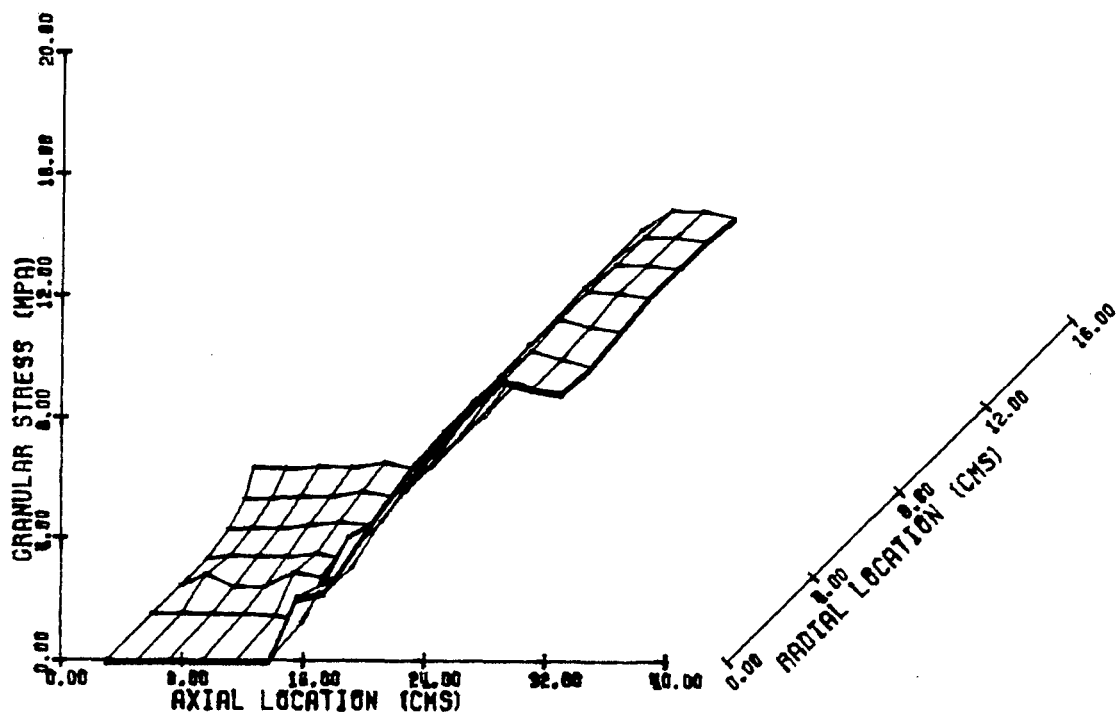


Fig. 3.2.3.21 Distribution of granular stress at 1.0 msec in case of zero intrusion projectile with irreversible granular stress law

ZERO INTRUSION PROJECTILE
 IRREVERSIBLE STRESS LAW
 STEP 194

TIME (MSEC) 1.300

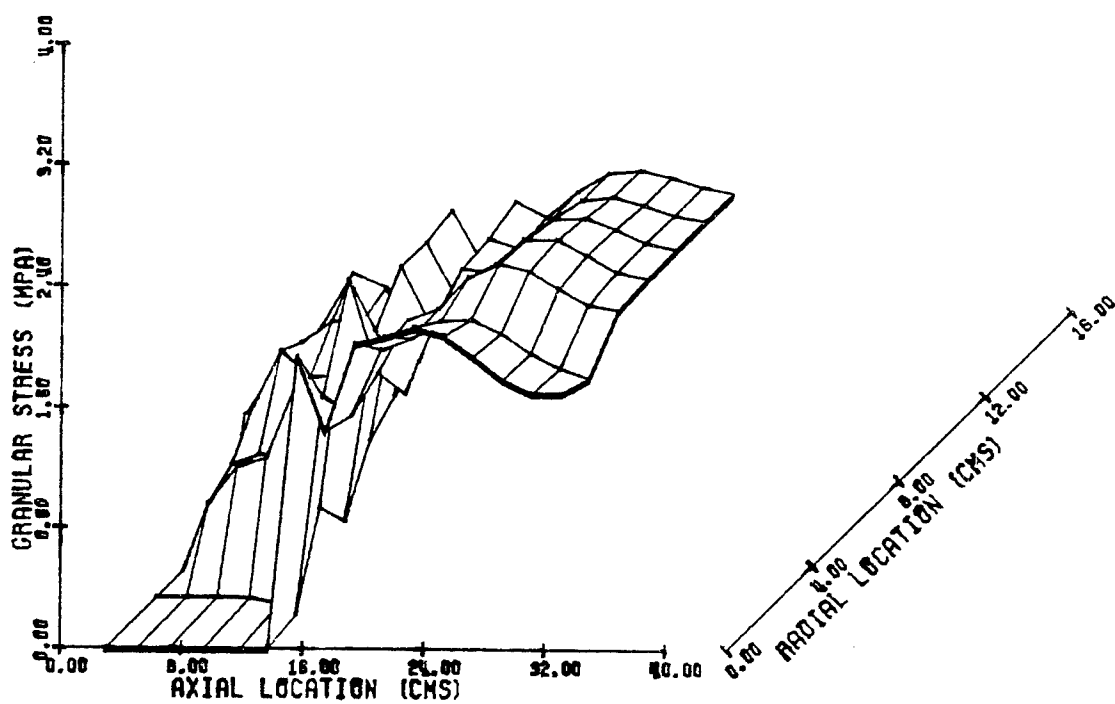


Fig. 3.2.3.22 Distribution of granular stress at 1.3 msec in case of zero intrusion projectile with irreversible granular stress law

ZERO INTRUSION PROJECTILE
 IRREVERSIBLE STRESS LAW
 STEP 87

TIME (MSEC) 0.600

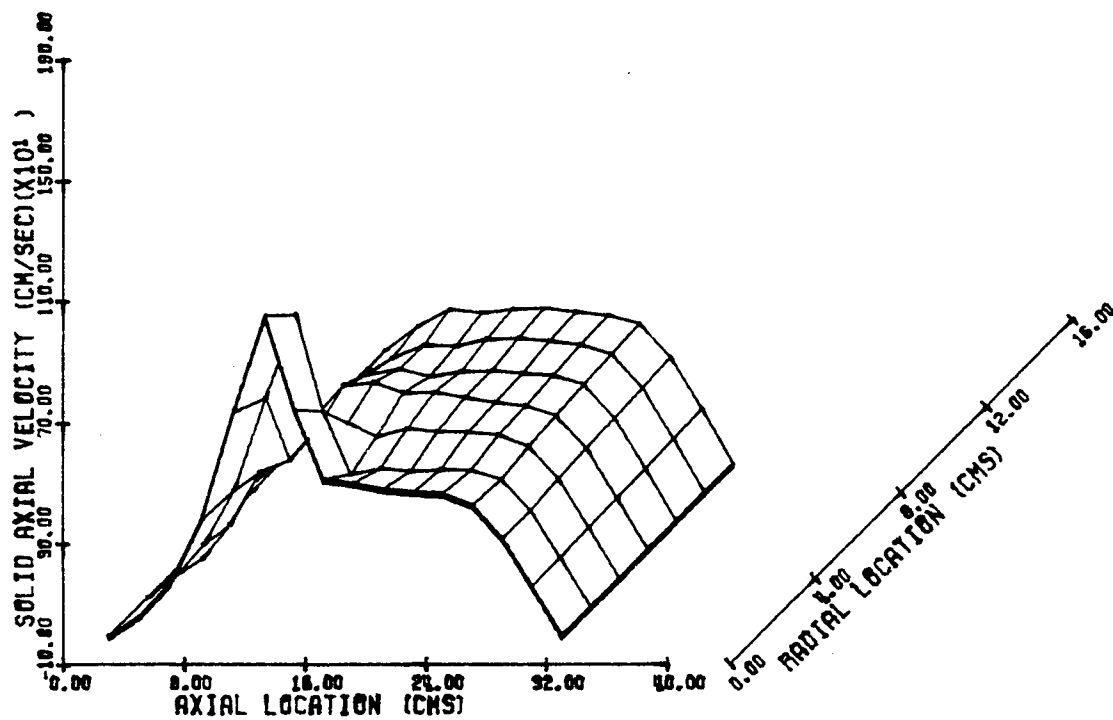


Fig. 3.2.3.23 Distribution of axial component of solid phase velocity at 0.6 msec in case of zero intrusion projectile with irreversible granular stress law

ZERO INTRUSION PROJECTILE
 IRREVERSIBLE STRESS LAW
 STEP 140

TIME (MSEC) 1.000

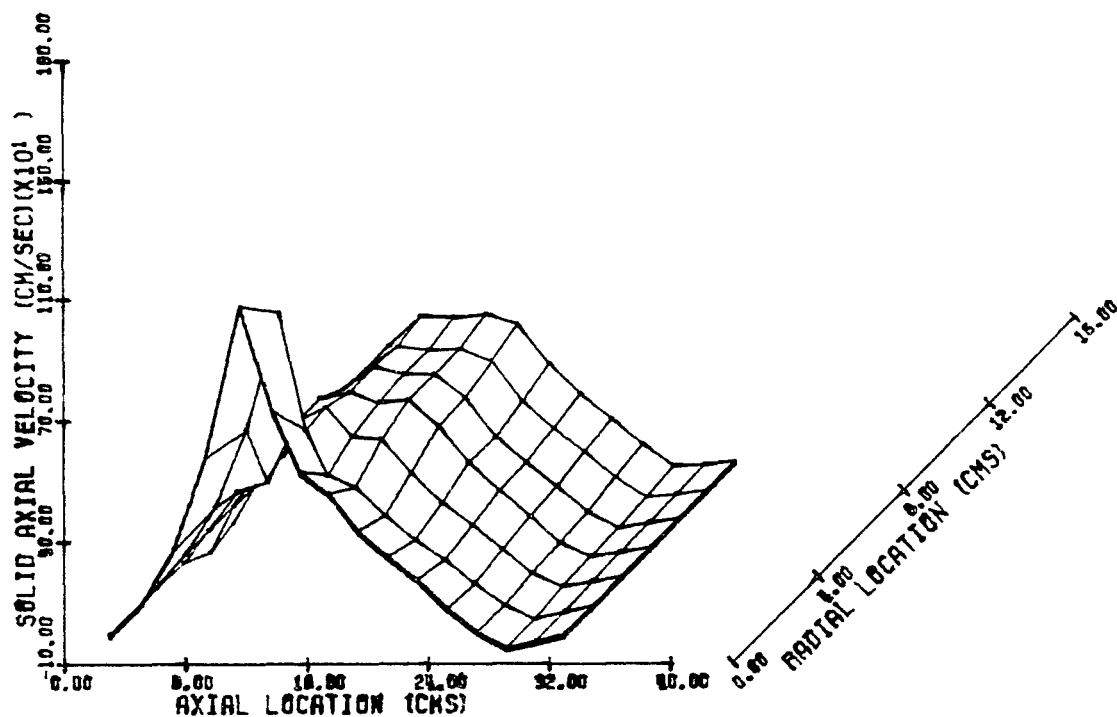


Fig. 3.2.3.24 Distribution of axial component of solid phase
 velocity at 1.0 msec in case of zero intrusion
 projectile with irreversible granular stress law

ZERO INTRUSION PROJECTILE
 IRREVERSIBLE STRESS LAW
 STEP 87

TIME (MSEC) 0.600

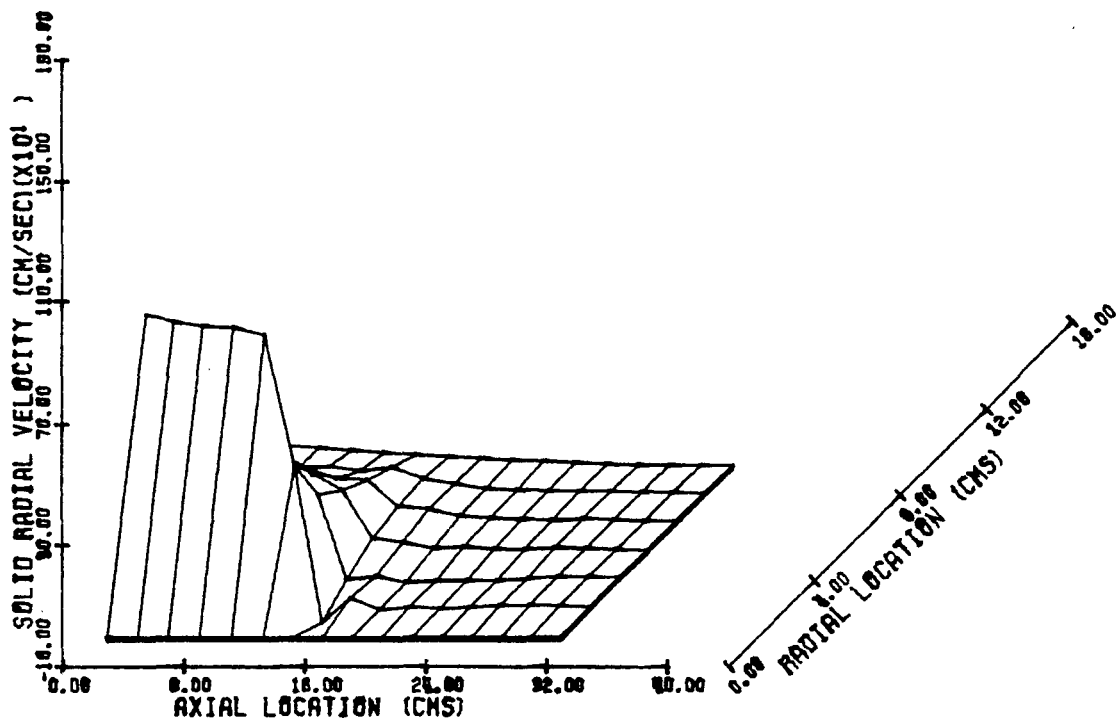


Fig. 3.2.3.25 Distribution of radial component of solid phase
 velocity at 0.6 msec in case of zero intrusion
 projectile with irreversible granular stress law

ZERO INTRUSION PROJECTILE
 IRREVERSIBLE STRESS LAW
 STEP 148

TIME (MSEC) 1.000

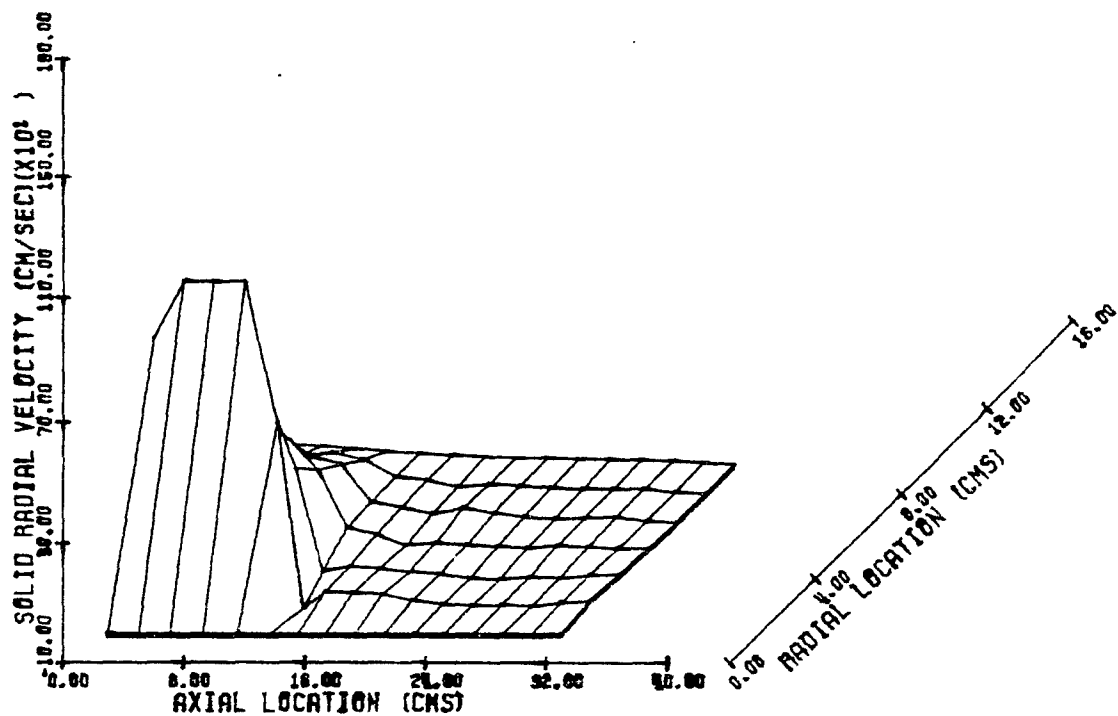


Fig. 3.2.3.26 Distribution of radial component of solid phase velocity at 1.0 msec in case of zero intrusion projectile with irreversible granular stress law

ZERO INTRUSION PROJECTILE
 IRREVERSIBLE STRESS LAW
 STEP 87

TIME (MSEC) 0.600

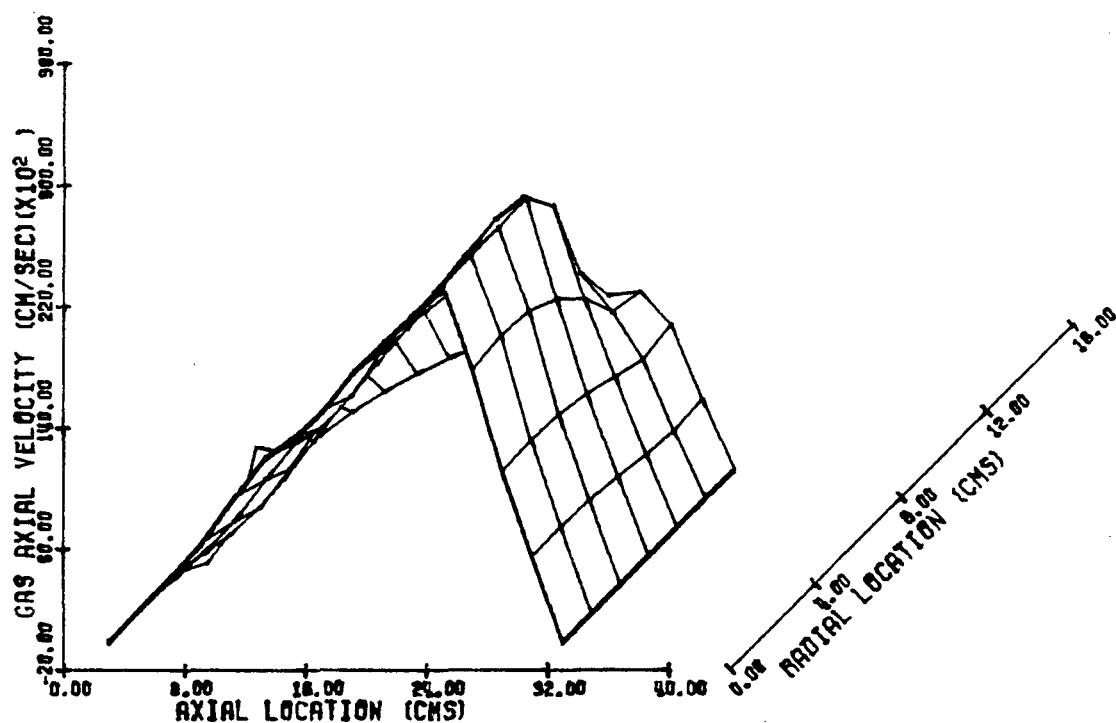


Fig. 3.2.3.27 Distribution of axial component of gas phase velocity at 0.6 msec in case of zero intrusion projectile with irreversible granular stress law

ZERO INTRUSION PROJECTILE
 IRREVERSIBLE STRESS LAW
 STEP 148

TIME (MSEC) 1.000

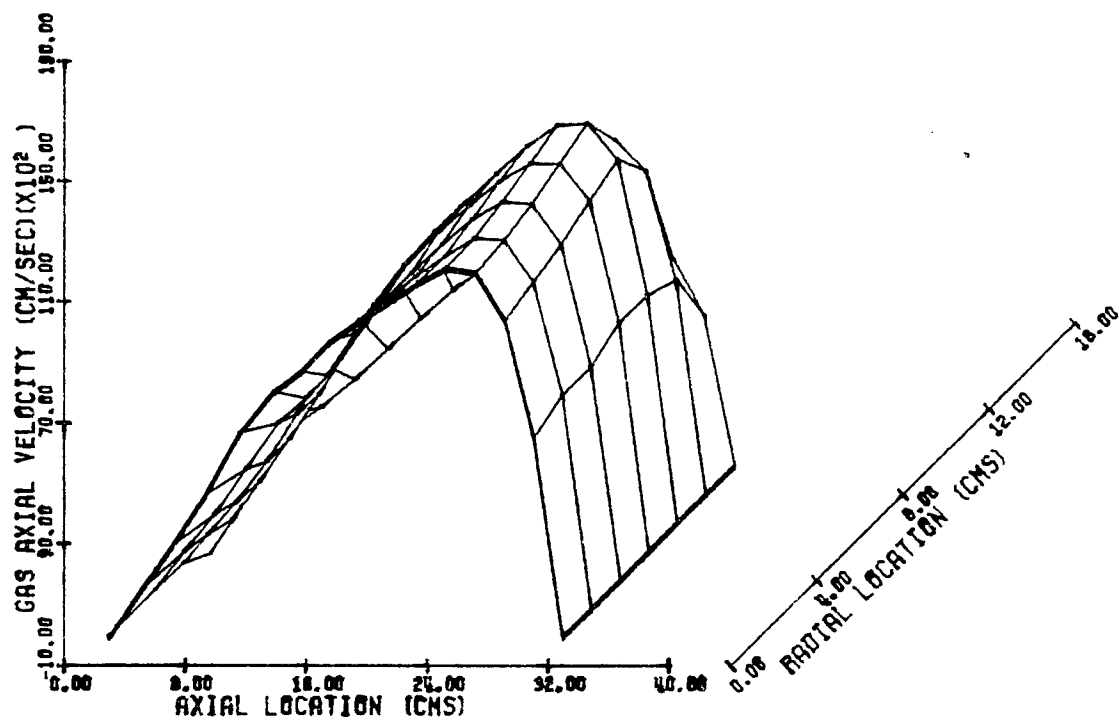


Fig. 3.2.3.28 Distribution of axial component of gas phase velocity at 1.0 msec in case of zero intrusion projectile with irreversible granular stress law

ZERO INTRUSION PROJECTILE
 IRREVERSIBLE STRESS LAW
 STEP 28

TIME (MSEC) 0.200

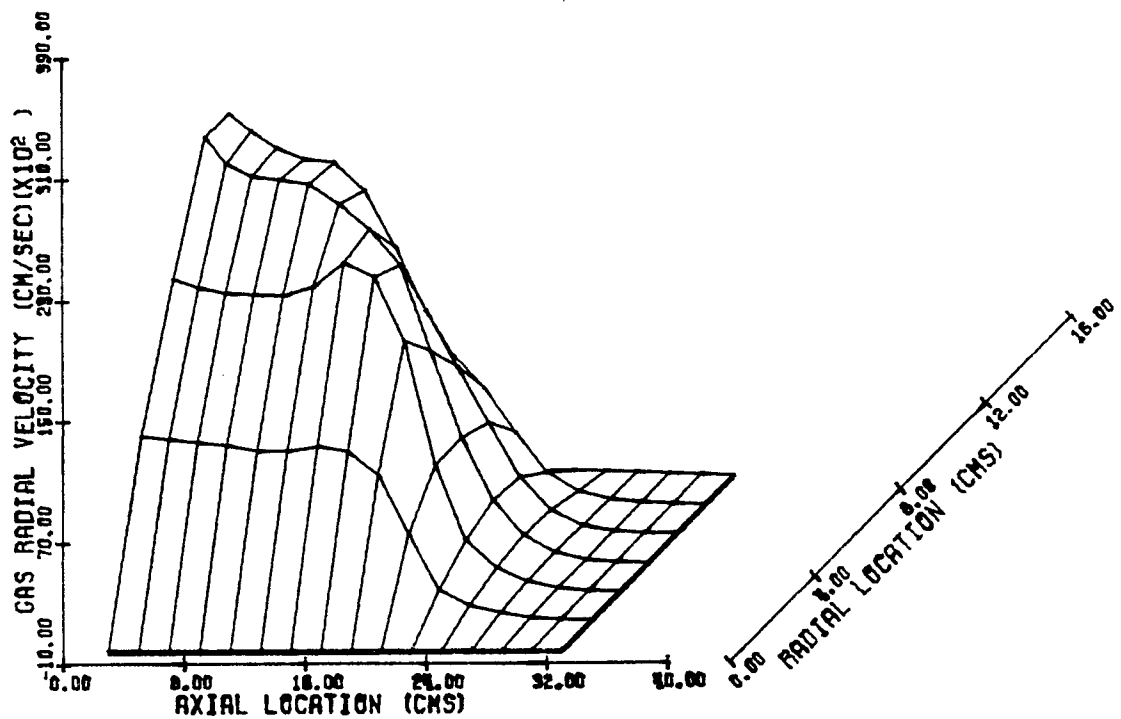


Fig. 3.2.3.29 Distribution of radial component of gas phase velocity at 0.2 msec in case of zero intrusion projectile with irreversible granular stress law

ZERO INTRUSION PROJECTILE
 IRREVERSIBLE STRESS LAW
 STEP 87

TIME (MSEC) 0.600

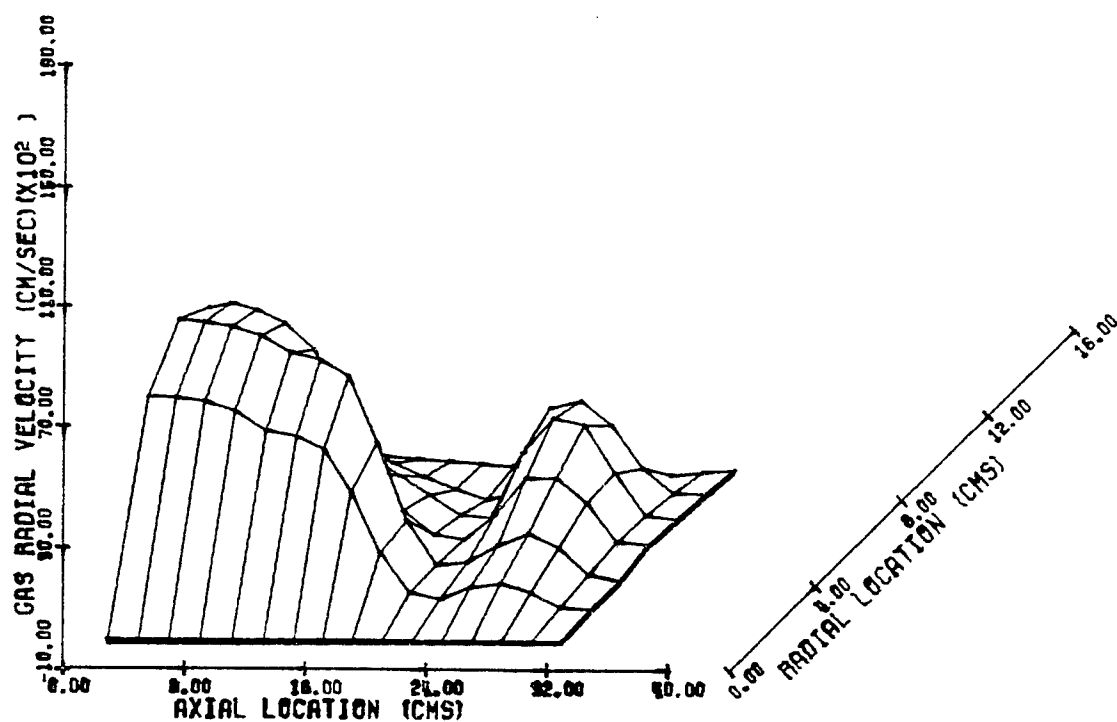


Fig. 3.2.3.30 Distribution of radial component of gas phase velocity at 0.6 msec in case of zero intrusion projectile with irreversible granular stress law

ZERO INTRUSION PROJECTILE
 IRREVERSIBLE STRESS LAW
 STEP 146

TIME (MSEC) 1.000

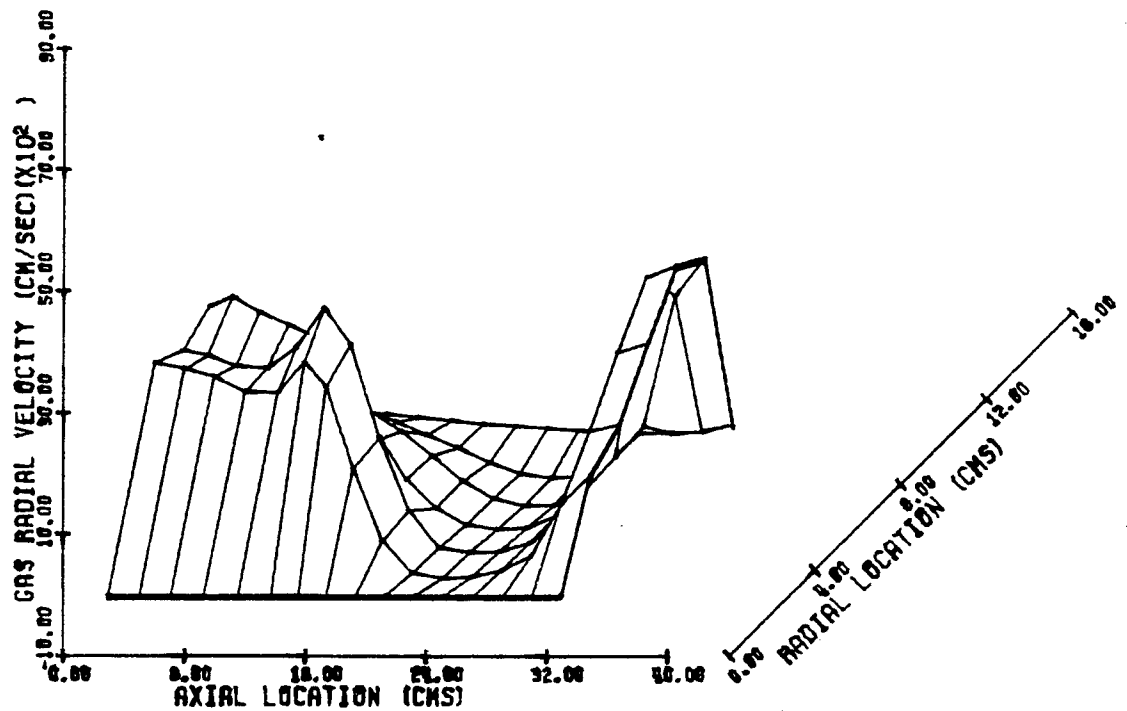


Fig. 3.2.3.31 Distribution of radial component of gas phase velocity at 1.0 msec in case of zero intrusion projectile with irreversible granular stress law

ZERO INTRUSION PROJECTILE
 IRREVERSIBLE STRESS LAW
 STEP 164

TIME (MSEC) 1.100

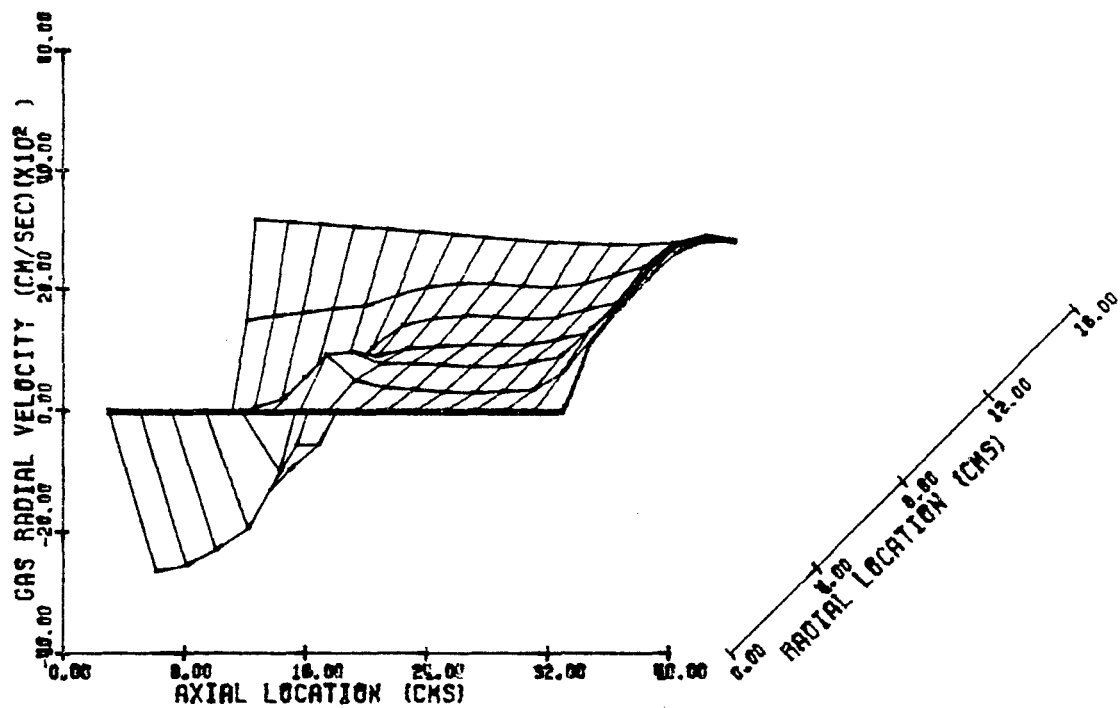


Fig. 3.2.3.32 Distribution of radial component of gas phase velocity at 1.1 msec in case of zero intrusion projectile with irreversible granular stress law

ZERO INTRUSION PROJECTILE
 IRREVERSIBLE STRESS LAW
 STEP 194

TIME (MSEC) 1.300

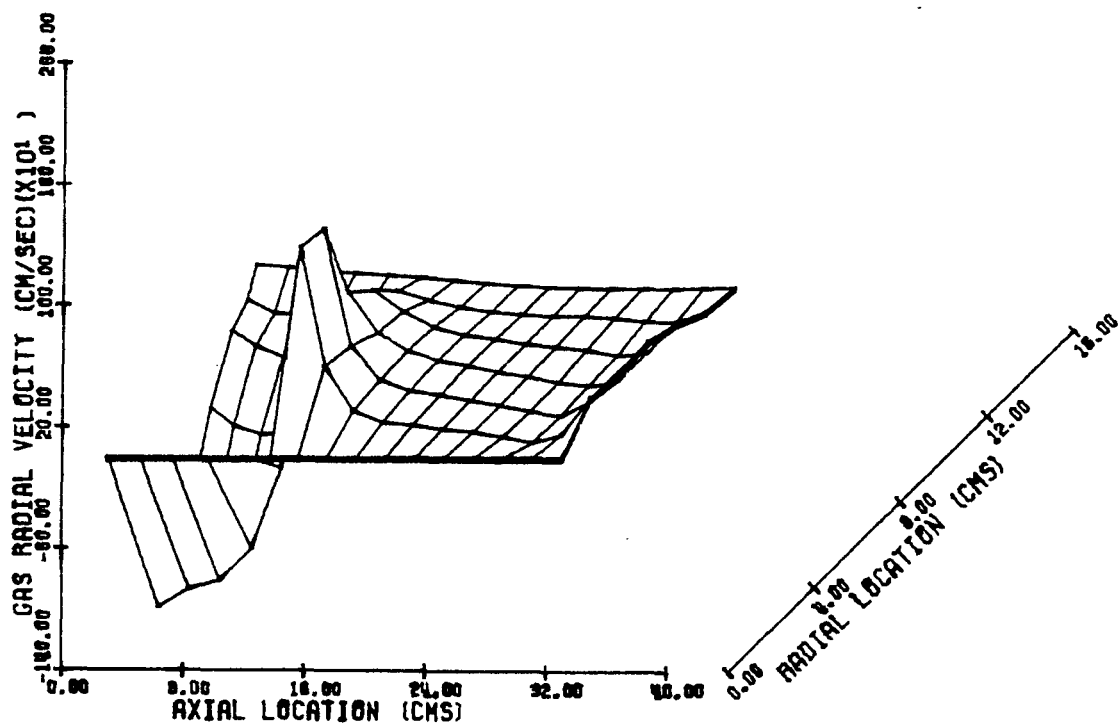


Fig. 3.2.3.33 Distribution of radial component of gas phase velocity at 1.3 msec in case of zero intrusion projectile with irreversible granular stress law

LONG INTRUSION PROJECTILE
 IRREVERSIBLE STRESS LAW
 STEP 406

TIME (MSEC) 1.400

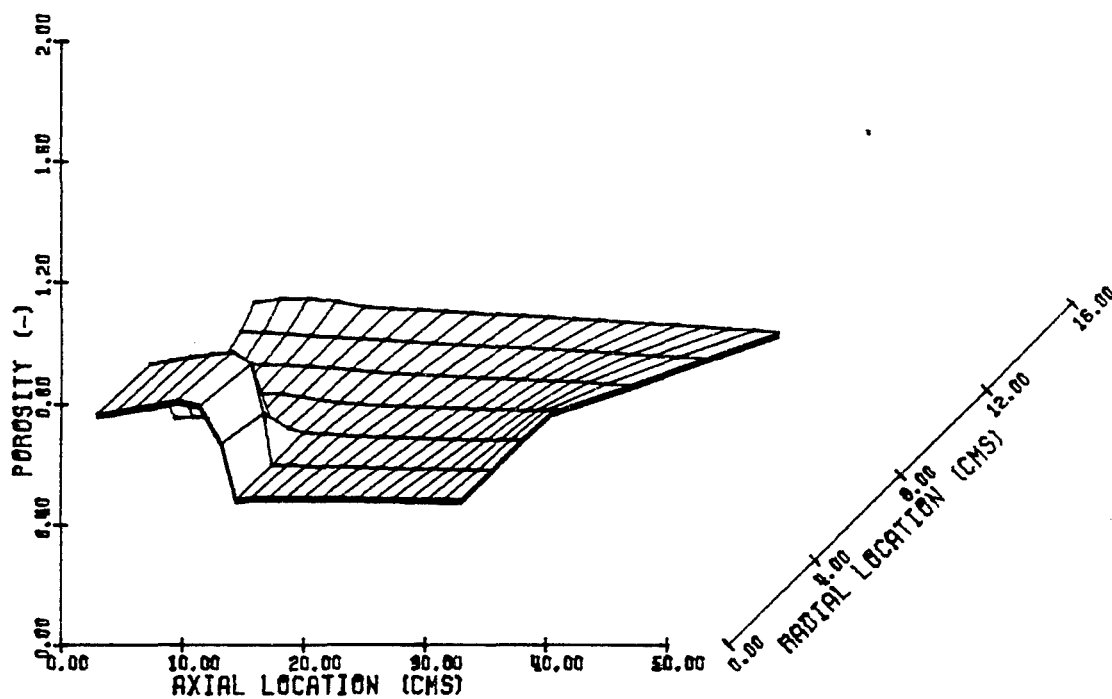


Fig. 3.2.4.1 Distribution of porosity at 1.4 msec in case of long intrusion projectile

LONG INTRUSION PROJECTILE
IRREVERSIBLE STRESS LAW
STEP 58

TIME (MSEC) 0.200

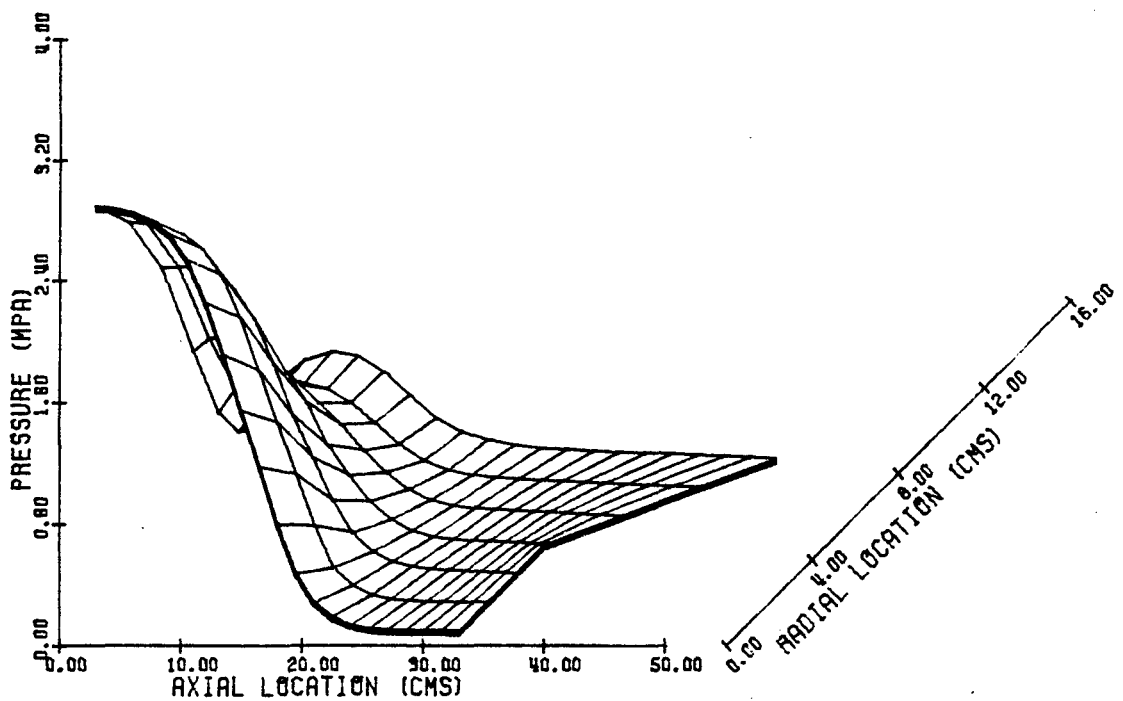


Fig. 3.2.4.2 Distribution of pressure at 0.2 msec in case of long intrusion projectile

LONG INTRUSION PROJECTILE
IRREVERSIBLE STRESS LAW
STEP 127

TIME (MSEC) 0.400

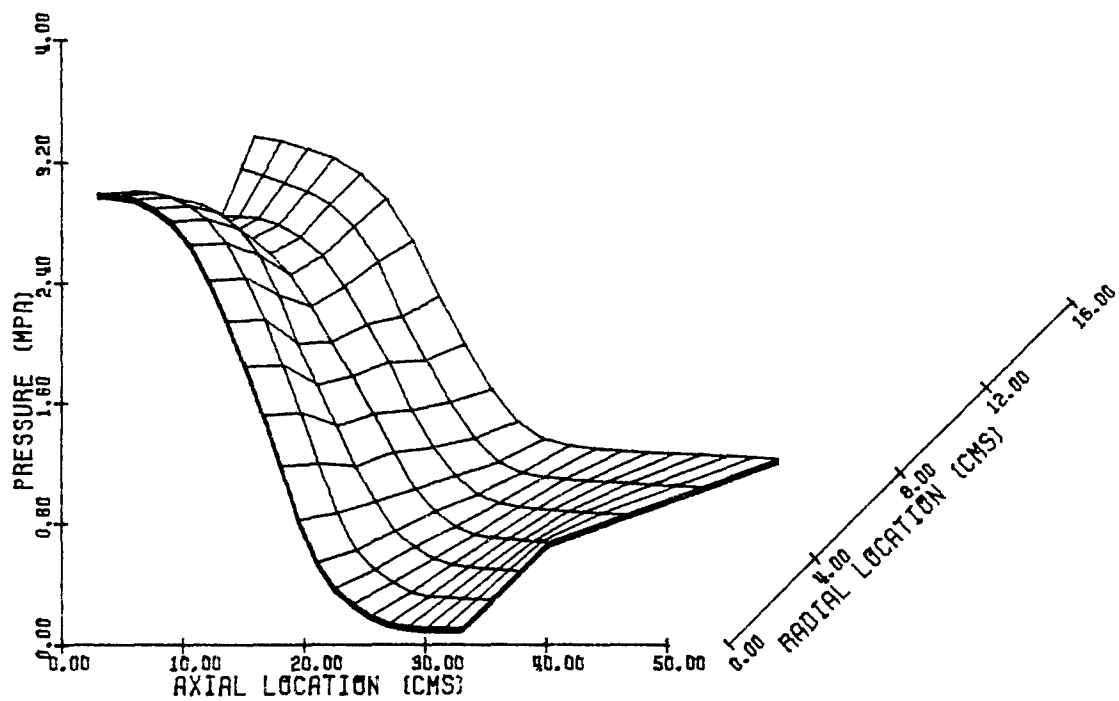


Fig. 3.2.4.3 Distribution of pressure at 0.4 msec in case of long intrusion projectile

LONG INTRUSION PROJECTILE
IRREVERSIBLE STRESS LAW
STEP 314

TIME (MSEC) 1.000

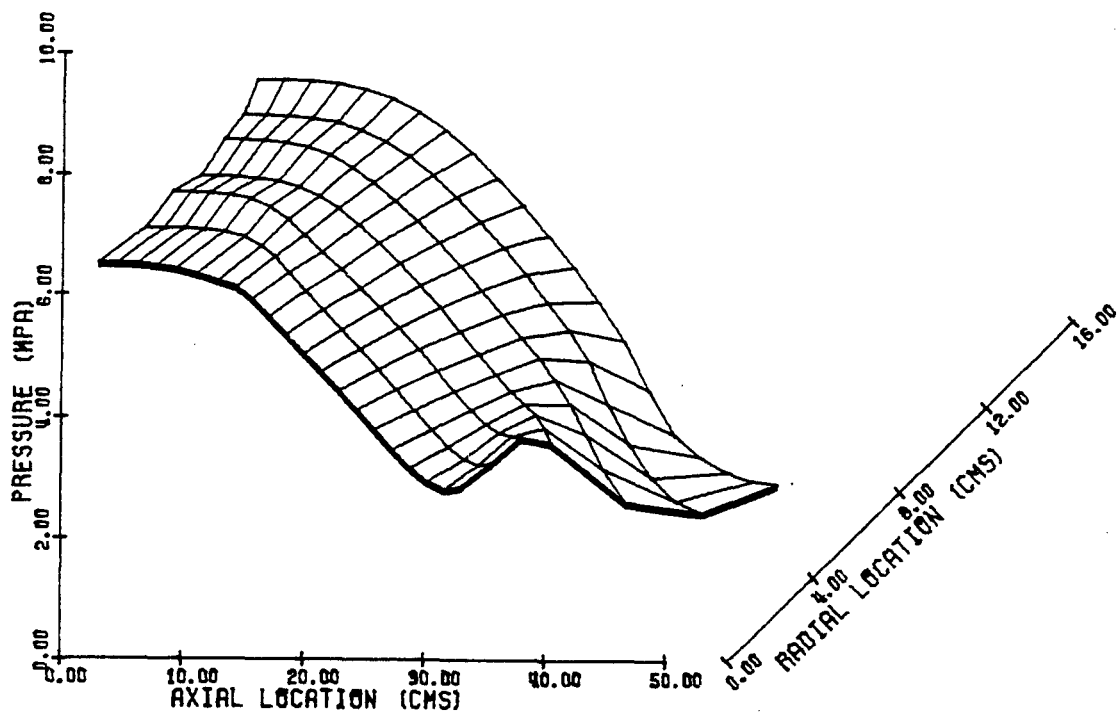


Fig. 3.2.4.4 Distribution of pressure at 1.0 msec in case of long intrusion projectile

LONG INTRUSION PROJECTILE
IRREVERSIBLE STRESS LAW
STEP 486

TIME (MSEC) 1.400

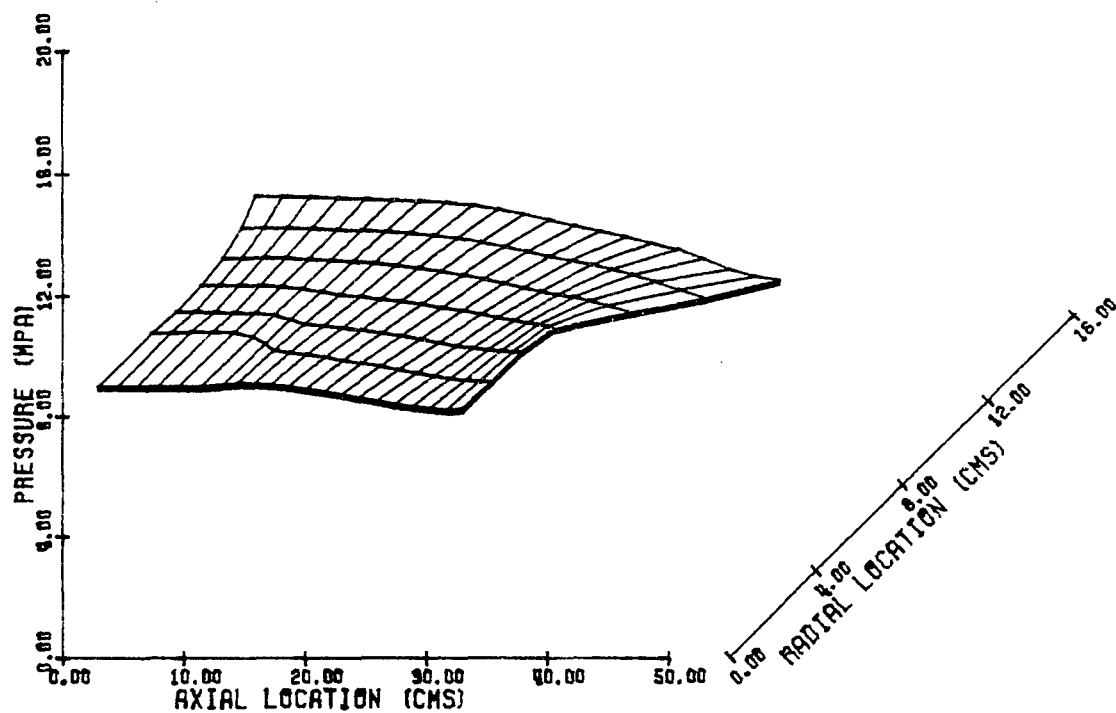


Fig. 3.2.4.5 Distribution of pressure at 1.4 msec in case of long intrusion projectile

LONG INTRUSION PROJECTILE
 IRREVERSIBLE STRESS LAW
 STEP 406

TIME (MSEC) 1.400

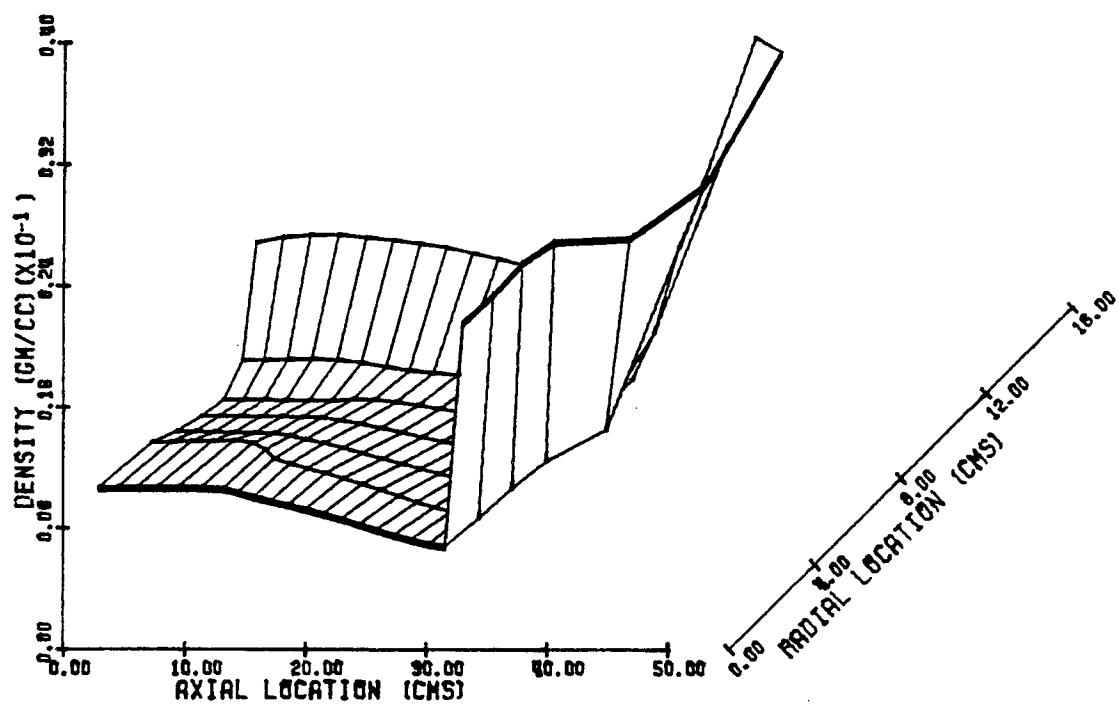


Fig. 3.2.4.6 Distribution of density of gas at 1.4 msec in case of long intrusion projectile

LONG INTRUSION PROJECTILE
 IRREVERSIBLE STRESS LAW
 STEP 486

TIME (MSEC) 1.400

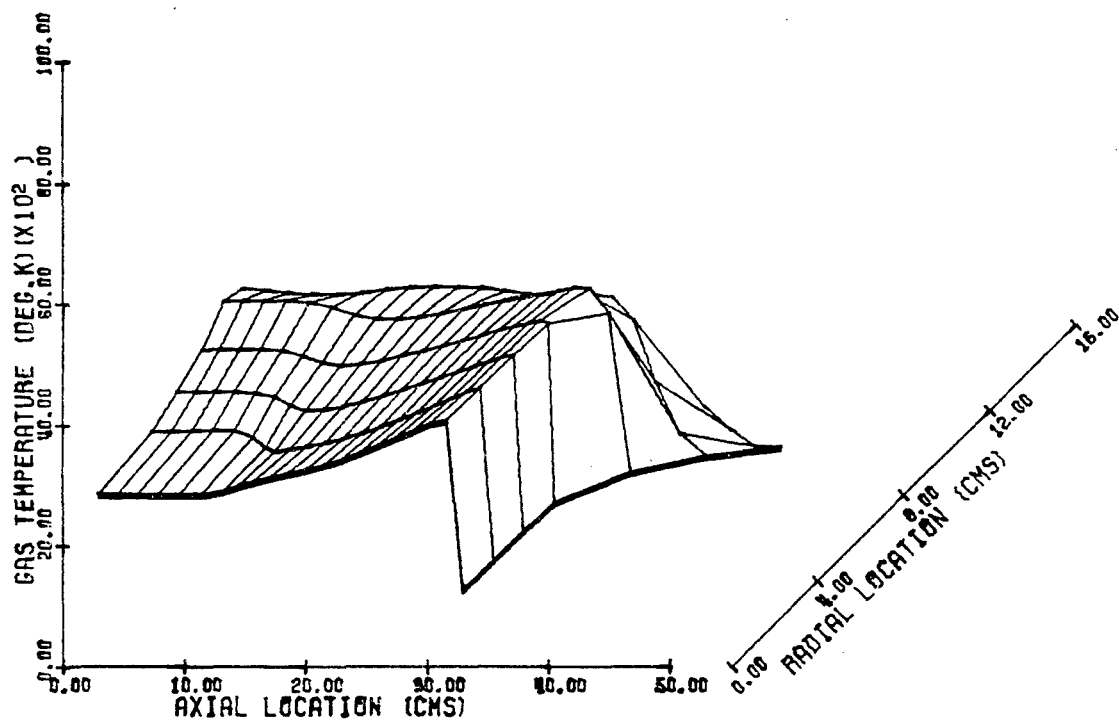


Fig. 3.2.4.7 Distribution of temperature of gas at 1.4 msec in case of long intrusion projectile

LONG INTRUSION PROJECTILE
IRREVERSIBLE STRESS LAW
STEP 58

TIME (MSEC) 0.200

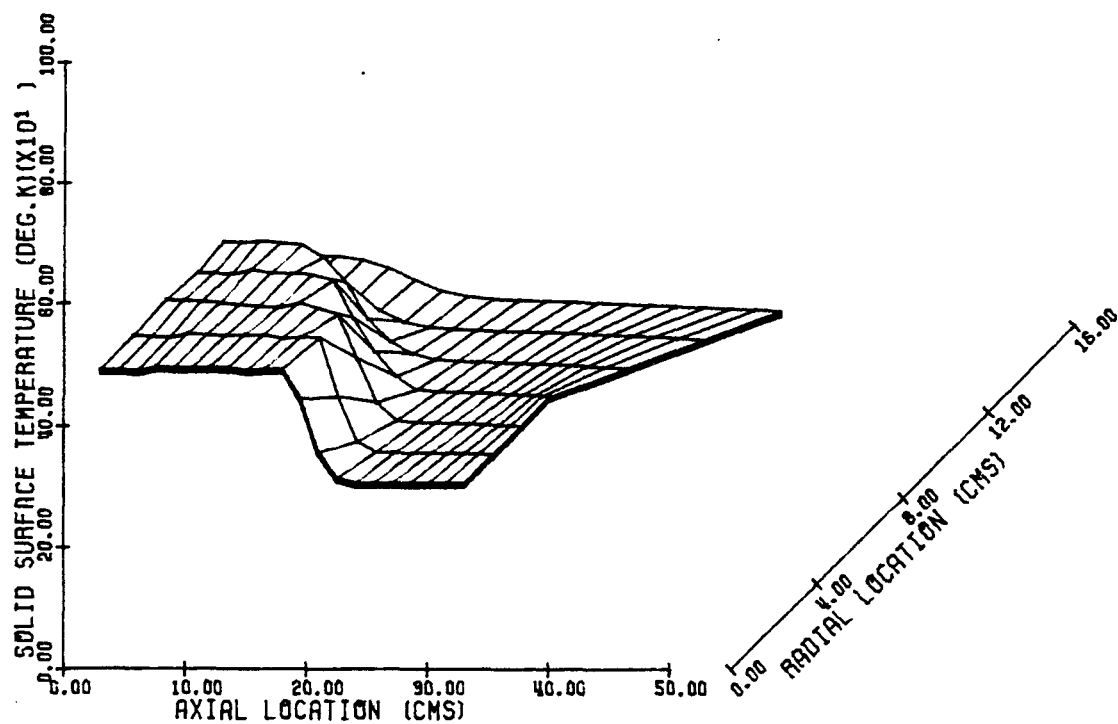


Fig. 3.2.4.8 Distribution of solid phase surface temperature
at 0.2 msec in case of long intrusion projectile

LONG INTRUSION PROJECTILE
 IRREVERSIBLE STRESS LAW
 STEP 127

TIME (MSEC) 0.400

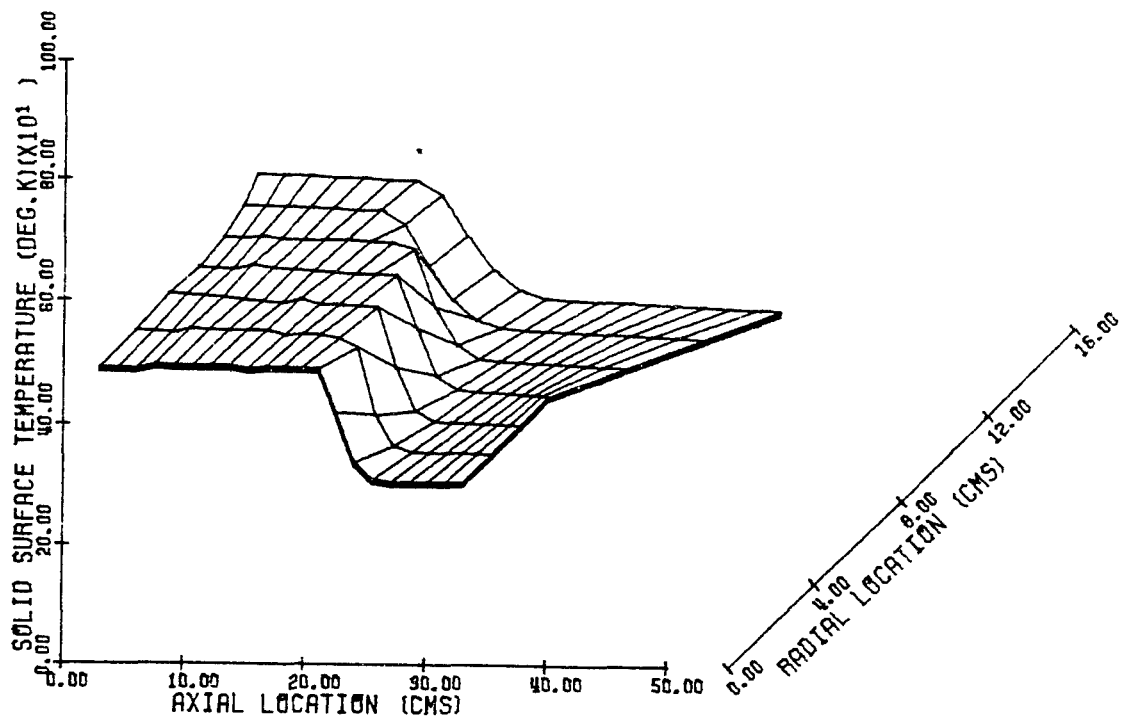


Fig. 3.2.4.9 Distribution of solid phase surface temperature
 at 0.4 msec in case of long intrusion projectile

LONG INTRUSION PROJECTILE
IRREVERSIBLE STRESS LAW
STEP 314

TIME (MSEC) 1.000

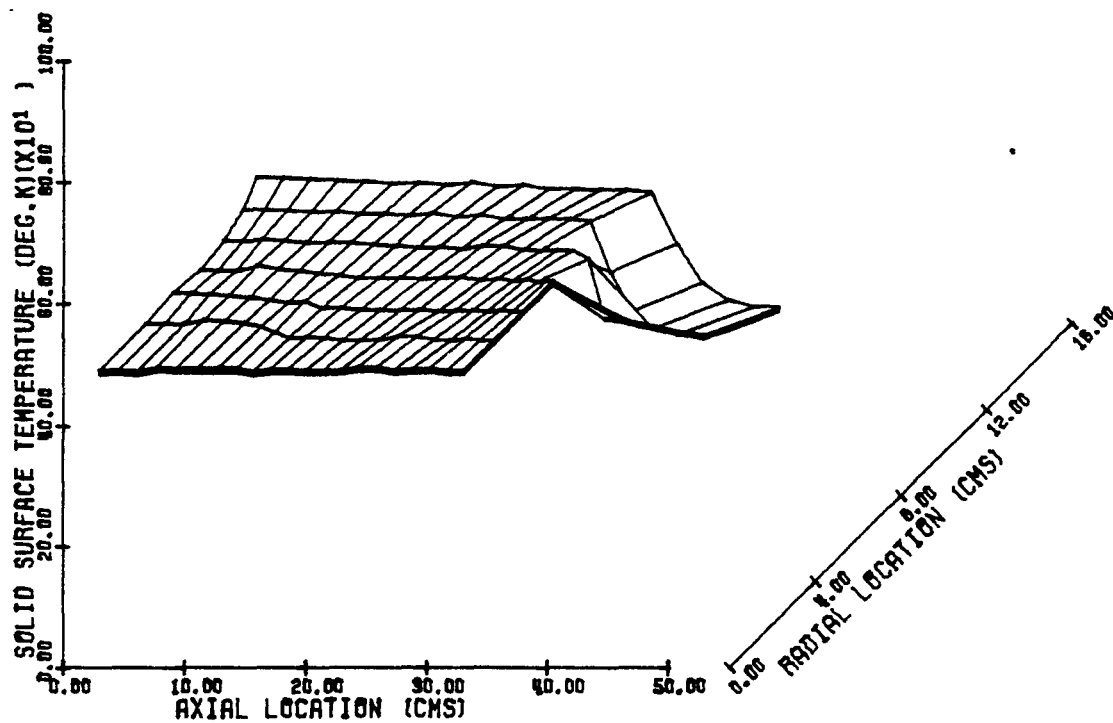


Fig. 3.2.4.10 Distribution of solid phase surface temperature
at 1.0 msec in case of long intrusion projectile

LONG INTRUSION PROJECTILE
IRREVERSIBLE STRESS LAW
STEP 486

TIME (MSEC) 1.400

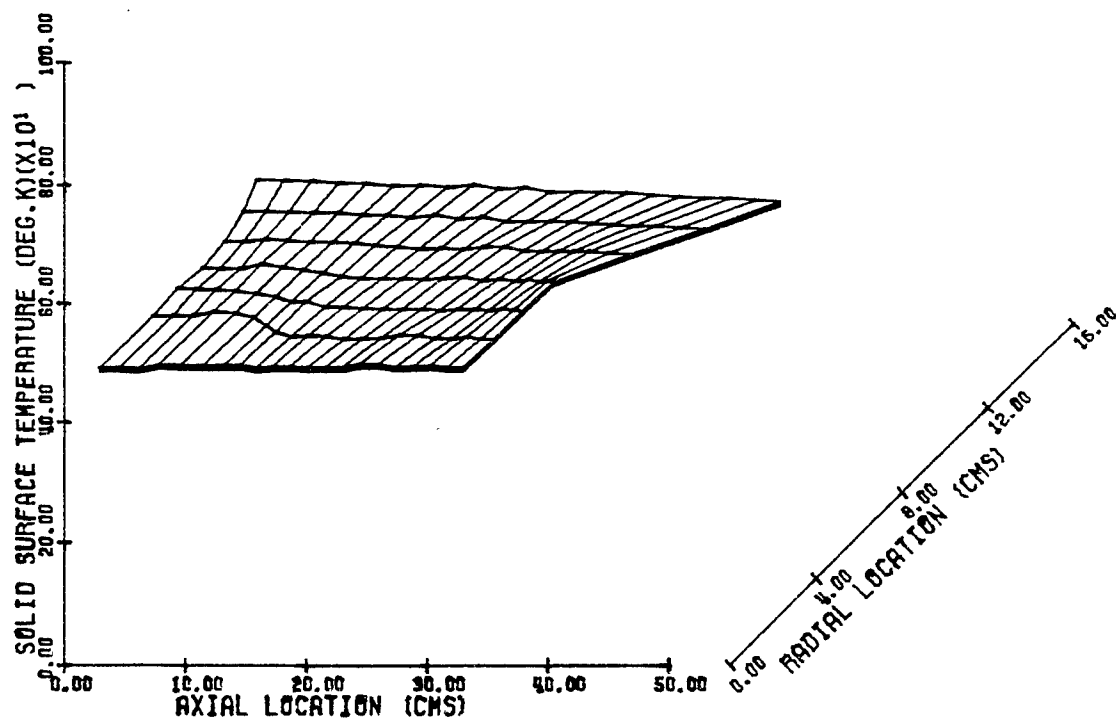


Fig. 3.2.4.11 Distribution of solid phase surface temperature
at 1.4 msec in case of long intrusion projectile

LONG INTRUSION PROJECTILE
IRREVERSIBLE STRESS LAW
STEP 92

TIME (MSEC) 0.300

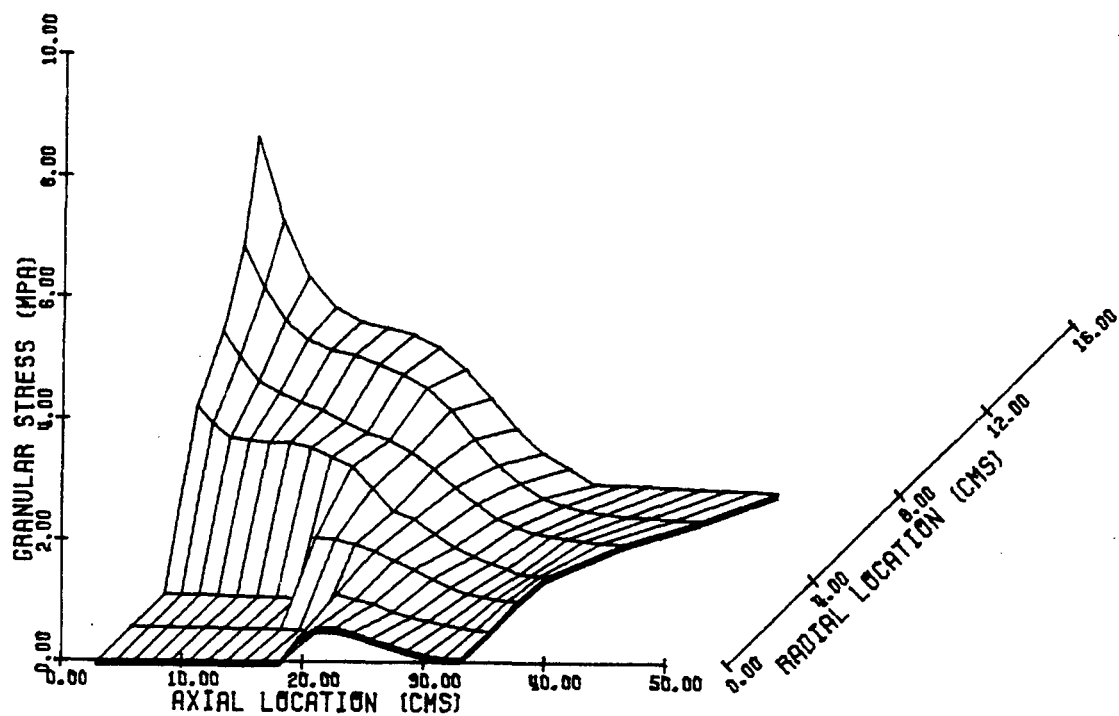


Fig. 3.2.4.12 Distribution of granular stress at 0.3 msec in case of long intrusion projectile

LONG INTRUSION PROJECTILE
 IRREVERSIBLE STRESS LAW
 STEP 314

TIME (MSEC) 1.000

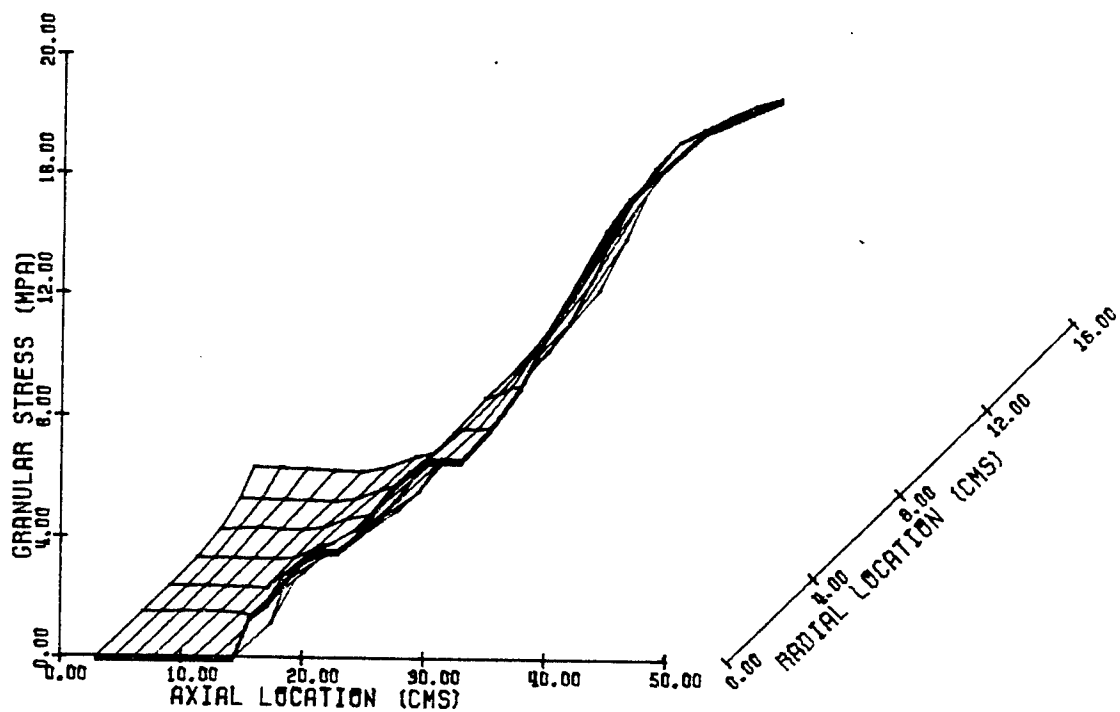


Fig. 3.2.4.13 Distribution of granular stress at 1.0 msec in case of long intrusion projectile

LONG INTRUSION PROJECTILE
IRREVERSIBLE STRESS LAW
STEP 441

TIME (MSEC) 1.300

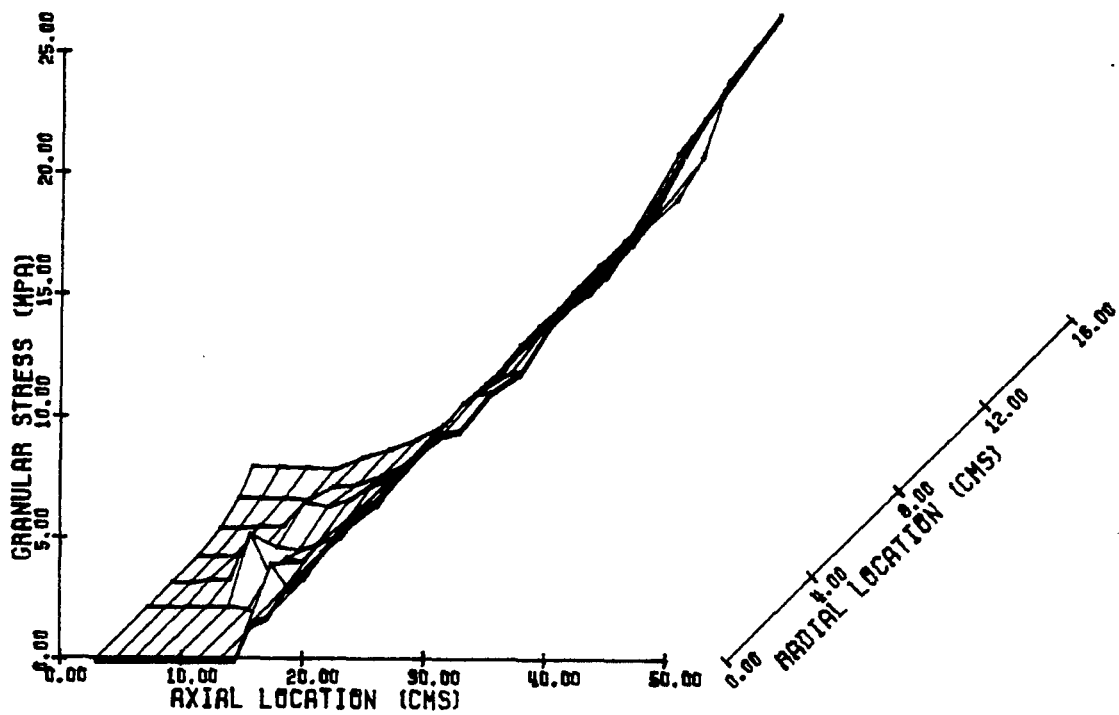


Fig. 3.2.4.14 Distribution of granular stress at 1.3 msec in case of long intrusion projectile

LONG INTRUSION PROJECTILE
 IRREVERSIBLE STRESS LAW
 STEP 175

TIME (MSEC) 0.600

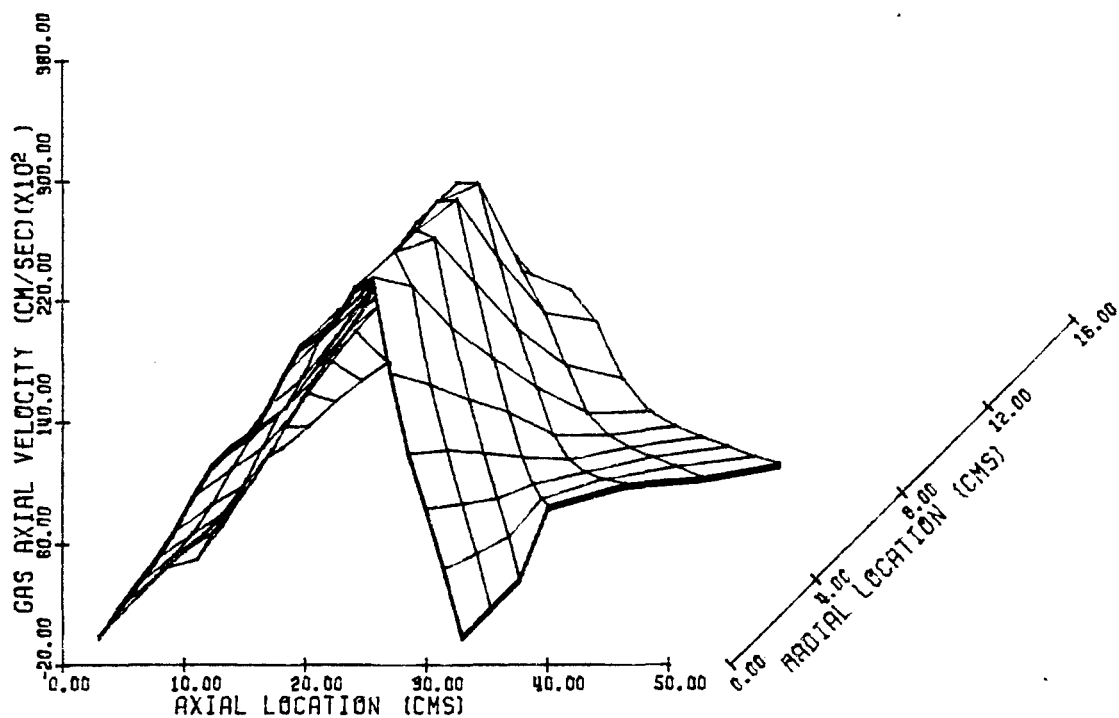


Fig. 3.2.4.15 Distribution of axial component of gas phase velocity at 0.6 msec in case of long intrusion projectile

LONG INTRUSION PROJECTILE
 IRREVERSIBLE STRESS LAW
 STEP 314

TIME (MSEC) 1.000

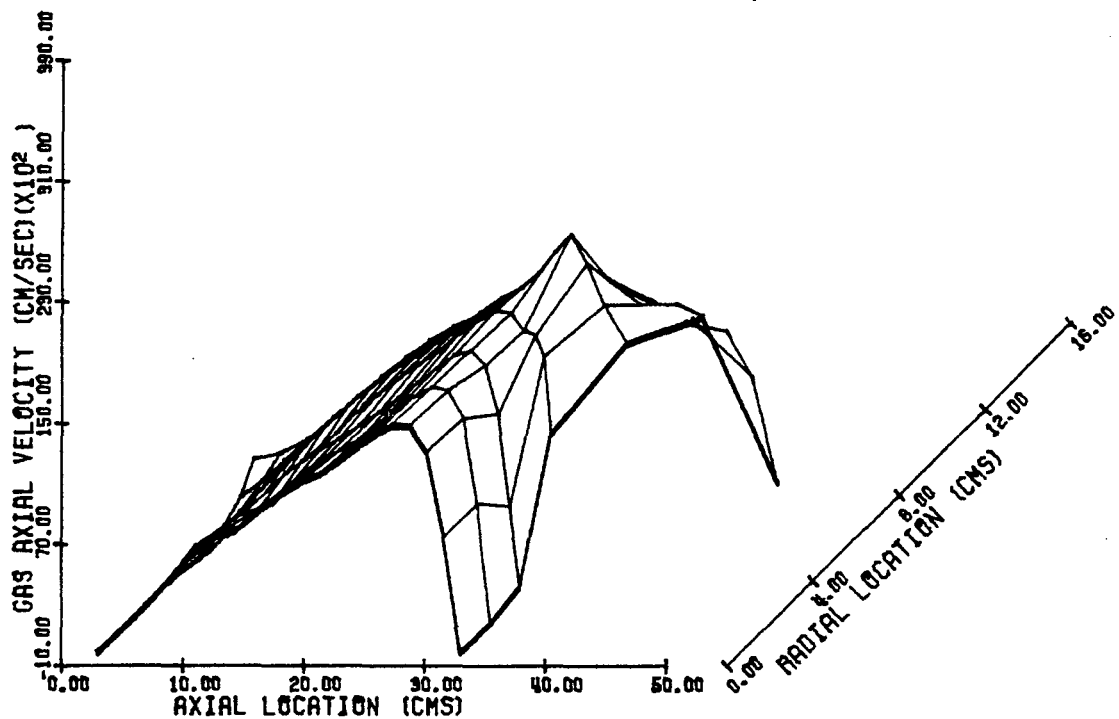


Fig. 3.2.4.16 Distribution of axial component of gas phase velocity at 1.0 msec in case of long intrusion projectile

LONG INTRUSION PROJECTILE
 IRREVERSIBLE STRESS LAW
 STEP 486

TIME (MSEC) 1.400

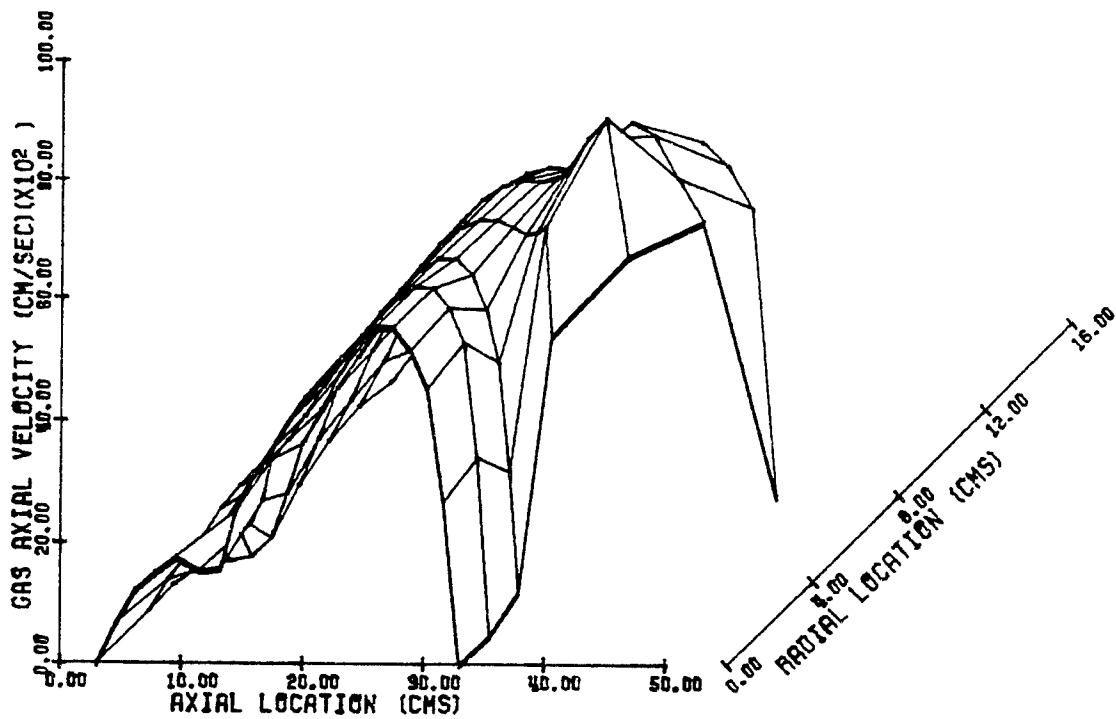


Fig. 3.2.4.17 Distribution of axial component of gas phase velocity
 at 1.4 msec in case of long intrusion projectile

LONG INTRUSION PROJECTILE
 IRREVERSIBLE STRESS LAW
 STEP 175

TIME (MSEC) 0.600

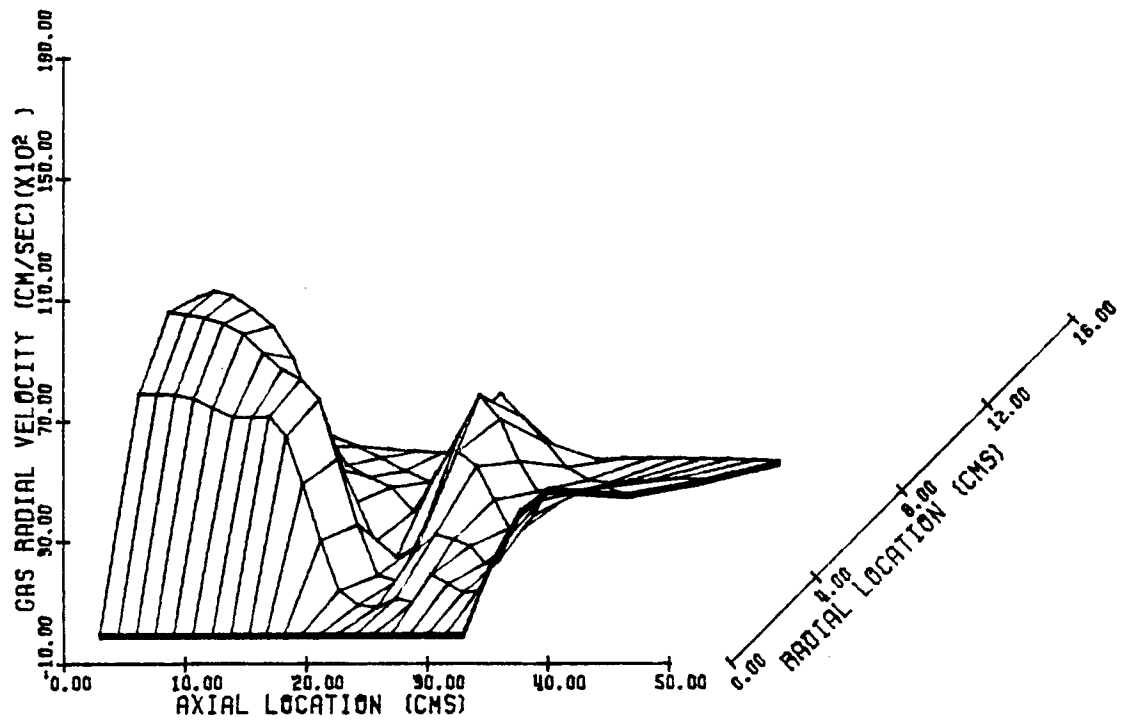


Fig. 3.2.4.18 Distribution of radial component of gas phase velocity at 0.6 msec in case of long intrusion projectile

LONG INTRUSION PROJECTILE
 IRREVERSIBLE STRESS LAW
 STEP 314

TIME (MSEC) 1.000

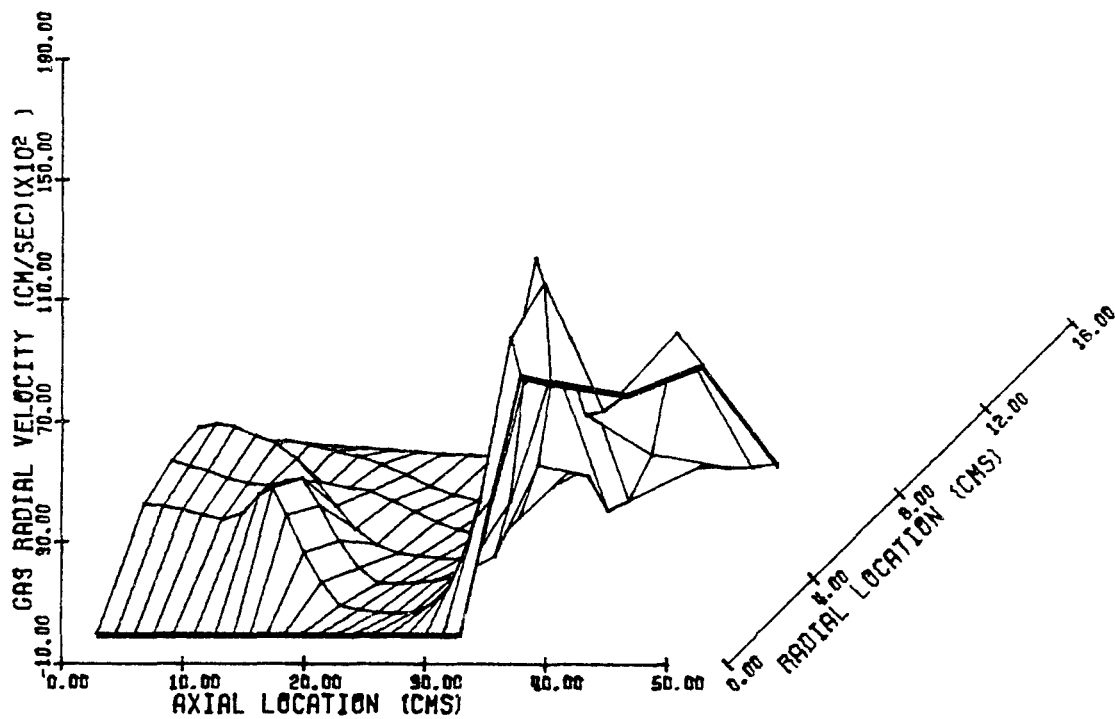


Fig. 3.2.4.19 Distribution of radial component of gas phase velocity at 1.0 msec in case of long intrusion projectile

LONG INTRUSION PROJECTILE
 IRREVERSIBLE STRESS LAW
 STEP 406

TIME (MSEC) 1.400

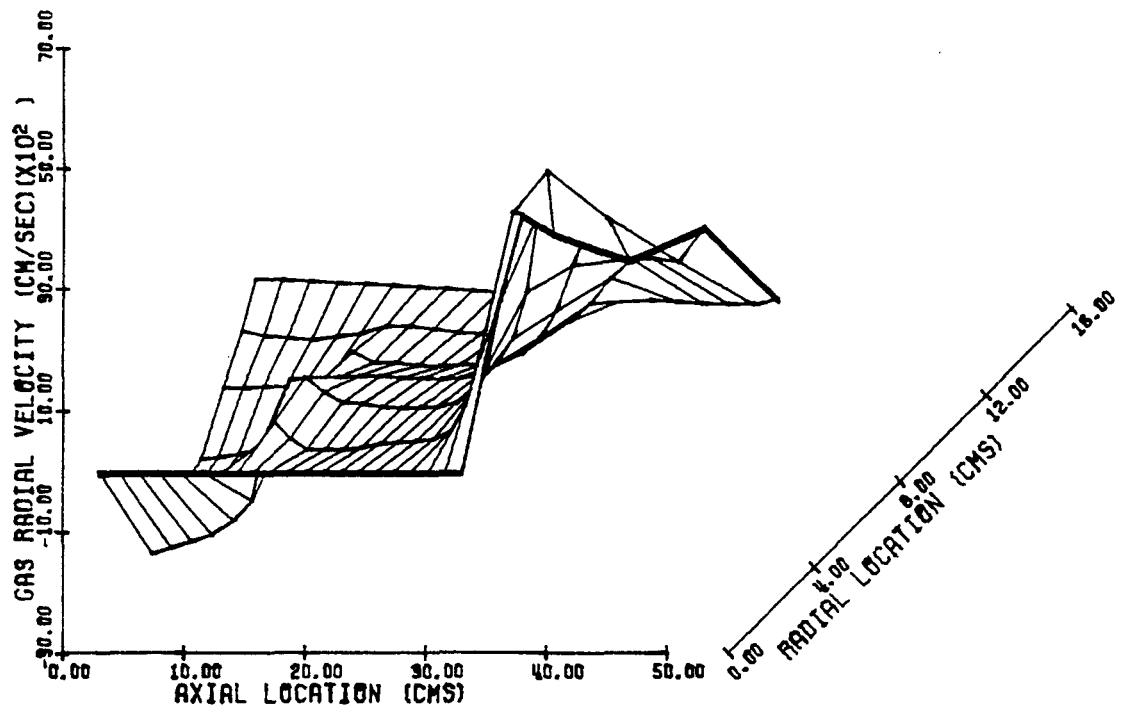


Fig. 3.2.4.20 Distribution of radial component of gas phase velocity at 1.4 msec in case of long intrusion projectile

LONG INTRUSION PROJECTILE
 IRREVERSIBLE STRESS LAW
 STEP 314

TIME (MSEC) 1.000

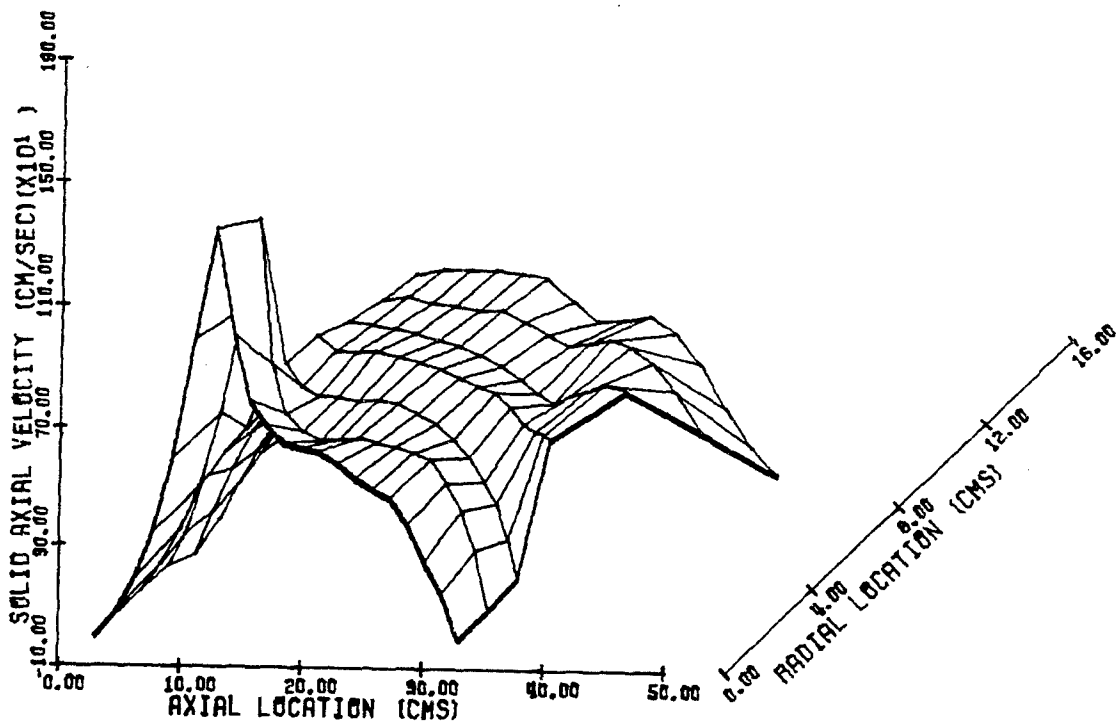


Fig. 3.2.4.21 Distribution of axial component of solid phase velocity at 1.0 msec in case of long intrusion projectile

LONG INTRUSION PROJECTILE
 IRREVERSIBLE STRESS LAW
 STEP 314

TIME (MSEC) 1.000

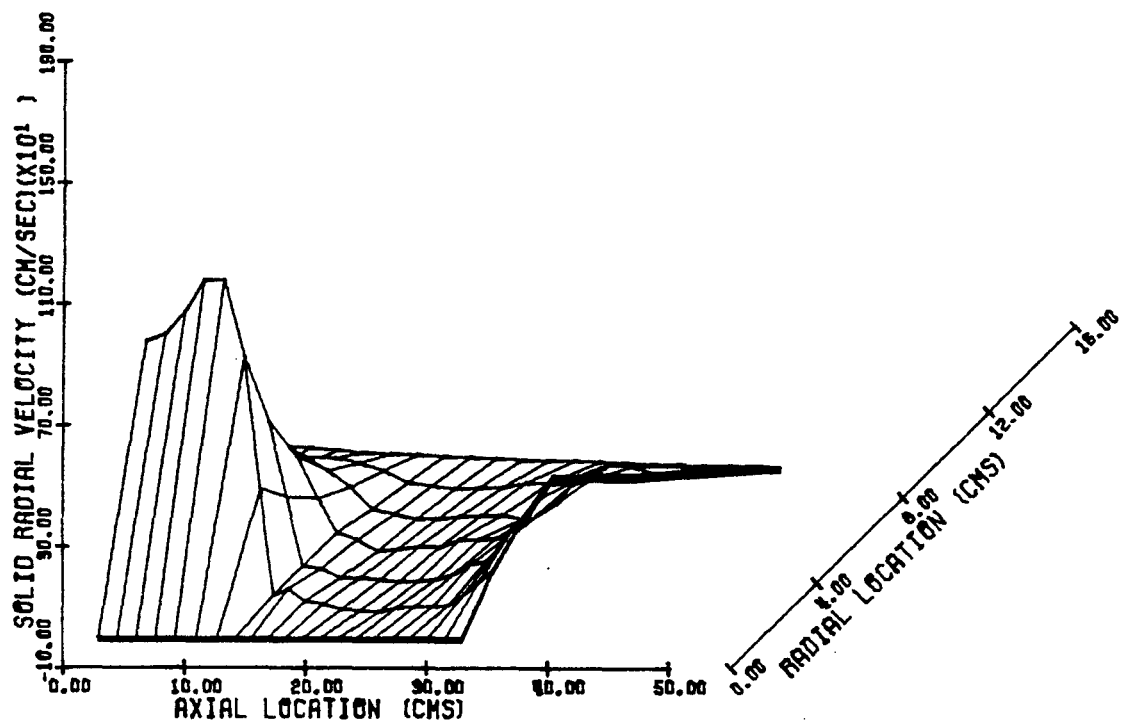


Fig. 3.2.4.22 Distribution of radial component of solid phase velocity at 1.0 msec in case of long intrusion projectile

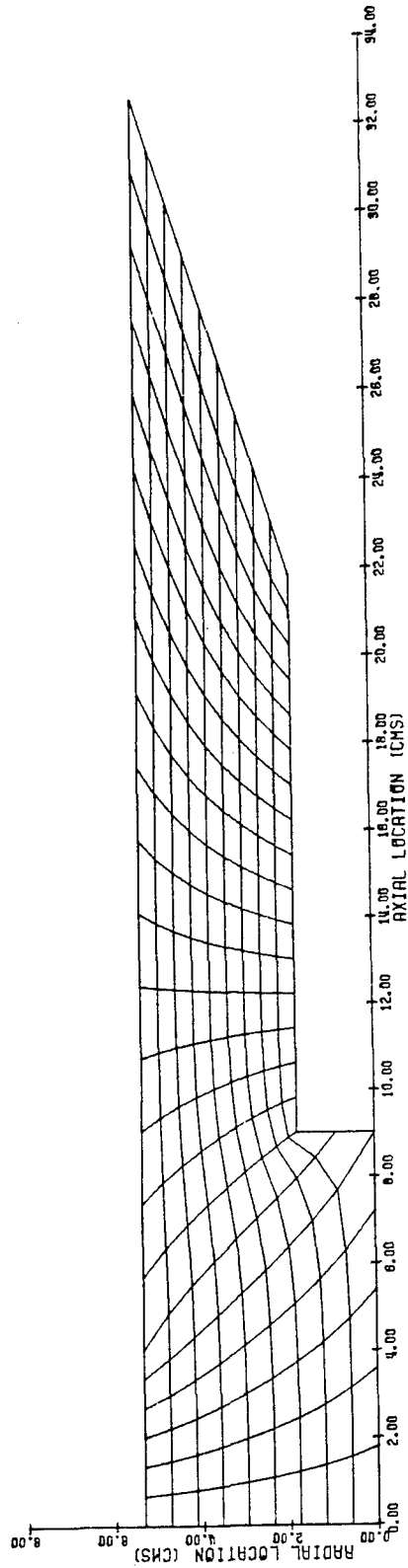
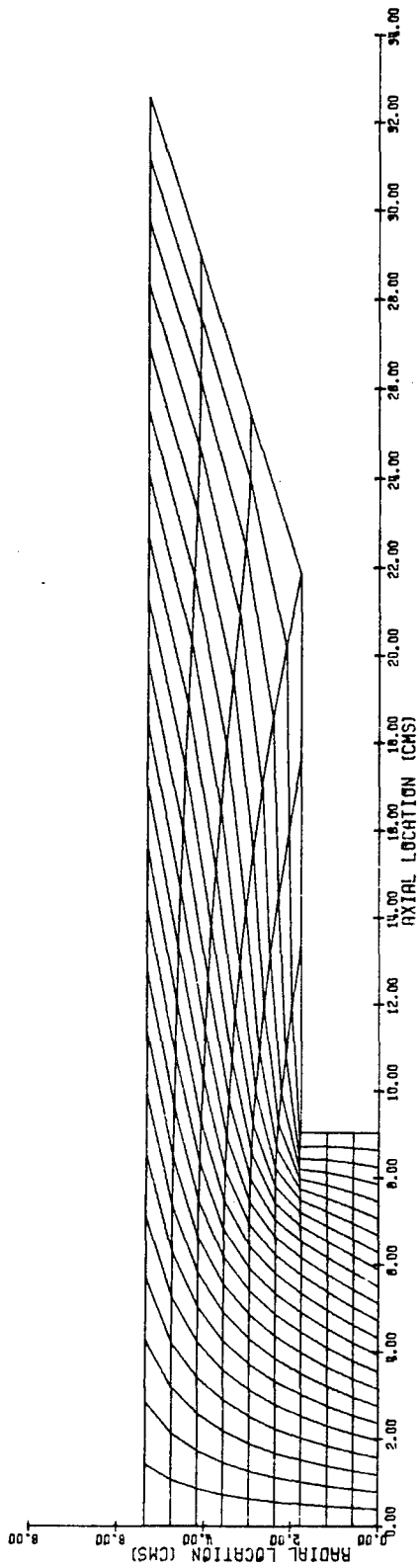


Fig. 4.1 Two Possible Mesh Distributions for 105mm Howitzer with XM622 Projectile.

REFERENCES

1. Corner, J.
 "Theory of the Interior Ballistics of Guns"
 New York, John Wiley and Son, Inc. 1950
2. Baer, P.G. and Frankle, J.M.
 "The Simulation of Interior Ballistics Performance of Guns
 by Digital Computer Program"
 BRL Report 1183 1962
3. Budka, A.J. and Knapton, J.D.
 "Pressure Wave Generation in Gun Systems - A Survey"
 BRL Memorandum Report 2567 1975
4. Kent, R.H.
 "Study of Ignition of 155-mm Gun"
 BRL Report 22 1935
5. Hedden, S.E. and Nance, G.A.
 "An Experimental Study of Pressure Waves in Gun Chambers"
 NPG Report 1534 1957
6. Horst, A.W., Jr. and Smith, T.C.
 "The Influence of Propelling Charge Configuration on Gun
 Environment Pressure-Time Anomalies"
 Proc. 12th Jannaf Combustion Meeting 1975
7. May, I.W., Clarke, E.V. and Hassmann, H.
 "A Case History: Gun Ignition Related Problems and Solutions
 for the XM-198 Howitzer"
 BRL Interim Memorandum Report 150 1973
8. Rocchio, J., Ruth, C. and May, I.
 "Grain Geometry Effects on Wave Dynamics in Large Caliber Guns"
 Proc. 13th Jannaf Combustion Meeting 1976
9. Horst, A.W., Smith, T.C. and Mitchell, S.E.
 "Key Design Parameters in Controlling Gun - Environment
 Pressure Wave Phenomena - Theory versus Experiment"
 Proc. 13th Jannaf Combustion Meeting 1976
10. Horst, A.W., Jr. and Gough, P.S.
 "Influence of Propellant Packaging on Performance of Navy
 Case Gun Ammunition"
 J. Ballistics v. 1 No.3 1977
11. East, J.L. and McClure, D.R.
 "Projectile Motion Predicted by a Solid/Gas Flow Interior
 Ballistic Model"
 Proc. 10th Jannaf Combustion Meeting 1973
12. Krier, H., van Tassel, W.F., Rajan, S. and Vershaw, J.
 "Model of Flame Spreading and Combustion Through Packed Beds
 of Propellant Grains"
 Tech.Rept AAE74-1, University of Illinois at Urbana-Champaign 1974
13. Kuo, K.K., Koo, J.H., Davis, T.R. and Coates, G.R.
 "Transient Combustion in Mobile, Gas-Permeable Propellants"
 Acta Astron. v.3, No.7-8 pp.574-591 1976

14. Gough, P.S. and Zwarts, F.J.
 "Theoretical Model for Ignition of Gun Propellant"
 Final Report, Part II, Contract N00174-72-C-0223 1972
15. Gough, P.S.
 "Fundamental Investigation of the Interior Ballistics of Guns"
 Final Report, Contract N00174-73-C-0501 1974
16. Gough, P.S.
 "The Flow of a Compressible Gas Through an Aggregate of
 Mobile, Reacting Particles"
 Ph.D Thesis McGill University 1974
17. Gough, P.S.
 "Computer Modelling of Interior Ballistics"
 Final Report Contract N00174-75-C-0131 1975
18. Gough, P.S.
 "Numerical Analysis of a Two-Phase Flow with Explicit
 Internal Boundaries"
 Final Report Contract N00174-75-C-0259 1977
19. Fisher, E.B. and Graves, K.W.
 "Mathematical Model of Double Base Propellant Ignition and
 Combustion in the 81mm Mortar"
 CAL Report No. DG-3029-D-1 1972
20. Fisher, E.B. and Trippe, A.P.
 "Mathematical Model of Center Core Ignition in the 175mm Gun"
 Calspan Report No. VQ-5163-D-2 1974
21. Fisher, E.B.
 "Propellant Ignition and Combustion in the 105mm Howitzer"
 Calspan Report No. VQ-5524-D-1 1975
22. Fisher, E.B. and Trippe, A.P.
 "Development of a Basis for Acceptance of Continuously
 Produced Propellant"
 Calspan Report No. VQ-5163-D-1 1973
23. Nelson, C.
 "Comparison of Predictions of Three Two-Phase Flow Codes"
 BRL Memorandum Report 2729 1977
24. Horst, A., Nelson, C. and May I.
 "Flame Spreading in Granular Propellant Beds: A Diagnostic
 Comparison of Theory to Experiment"
 Proc. AIAA/SAE 13th Joint Propulsion Conference 1977
25. Horst, A.W., May, I.W. and Clarke, E.V., Jr.
 "The Missing Link Between Pressure Waves and Breechblows"
 Proc. 14th Jannaf Combustion Meeting 1977
26. Gough, P.S.
 "Theoretical Study of Two-Phase Flow Associated with Granular
 Bag Charges"
 Final Report, Contract DAAK11-77-C-0028 1978
27. Clarke, E.V. Jr. and May, I.W.
 "Subtle Effects of Low-Amplitude Pressure Wave Dynamics
 on the Ballistic Performance of Guns"
 Proc. 11th Jannaf Combustion Meeting 1974

28. Olenick, P.J. Jr.
 "Investigation of the 76mm/62 Caliber Mark 75 Gun Mount
 Malfunction"
 NSWC/DL TR-31441975
29. Thompson, J.F., Thames, F.C. and Mastin, C.W.
 "Automatic Numerical Generation of Body-Fitted Curvilinear
 Coordinate System for Field Containing Any Number of Arbitrary
 Two-Dimensional Bodies"
 J. Comp. Phys. 15 299-3191974
30. MacCormack, R.W.
 "The Effect of Viscosity in Hypervelocity Impact Cratering"
 AIAA Paper No. 69-3541969
31. Moretti, G.
 "Calculation of the Three-Dimensional, Supersonic, Inviscid,
 Steady Flow Past an Arrow-Winged Airframe"
 POLY-AE/AM Report No. 76-81976
32. Kentzer, C.P.
 "Discretization of Boundary Conditions on Moving Discontinuities"
 Proc. 2nd Int. Conf. on Num. Meth in Fluid Dynamics
 Berkeley, Calif. Sept. 15-191970
33. Shelton, S., Bergles, A. and Saha, P.
 "Study of Heat Transfer and Erosion in Gun Barrels"
 AFATL-TR-73-691973
34. Gough, P.S. and Zwarts, F.J.
 "Modeling Heterogeneous Two-Phase Reacting Flow"
 AIAA J v.17 n.1 pp.17-25 January1979
35. Harlow, F.H. and Amsden, A.A.
 "Numerical Calculation of Multi phase Fluid Flow"
 J. Comp. Phys. 17 19-521975
36. Harlow, F.H. and Amsden, A.A.
 "Flow of Interpenetrating Material Phases"
 J. Comp. Phys. 18 440-4641975
37. Harlow, F.H. and Amsden, A.A.
 "K-TIF: A Two-Fluid Computer Program for Downcomer Flow
 Dynamics"
 Los Alamos Scientific Laboratory, LA 69941978
38. Rivard, W.C. and Torrey, M.D.
 "K-FIX: A Computer Program for Transient, Two-Dimensional,
 Two-Fluid Flow"
 Los Alamos Scientific Laboratory, LA-NUREG-66231977
39. Amsden, A.A. and Harlow, F.H.
 "KACHINA: An Eulerian Computer Program for Multifield
 Fluid Flows"
 Los Alamos Scientific Laboratory, LA-56801974
40. Lee, W.H. and Lyczkowski, R.W.
 "Development of a State-of-the-Art Reactor Containment Program"
 Proc. 17th National Heat Transfer Conference1977

41. Moretti, G.
 "The Importance of Boundary Conditions in the Numerical
 Treatment of Hyperbolic Equations"
 PIBAL Report No. 68-34 1968
42. Kuo, K.K., Vichnevetsky, R. and Summerfield, M.
 "Theory of Flame Front Propagation in Porous Propellant
 Charges Under Confinement"
 AIAA J. v.11 No.4 1973
43. Krier, H., Shimpi, S.A. and Adams, M.J.
 "Interior Ballistic Predictions Using Data From Closed and
 Variable Volume Simulators"
 Tech. Rept. AAE73-6, University of Illinois at Urbana-Champaign 1973
44. Ergun, S.
 "Fluid Flow Through Packed Columns"
 Chem. Eng. Progr. v.48 p.89 1952
45. Anderssen, K.E.B.
 "Pressure Drop in Ideal Fluidization"
 Chem. Eng. Sci. v.15 1961
46. Stanek, V. and Szekely, J.
 "The Effect of Non-Uniform Porosity in Causing Flow
 Maldistributions in Isothermal Packed Beds"
 Can. J. Chem. Eng. v.50 1972
47. Kuo, K.K. and Nydegger, C.C.
 "Flow Resistance Measurement and Correlation in a
 Packed Bed of WC-870 Ball Propellants"
 J. Ballistics, v.2, No.1 p.1 1978
48. Robbins, F. and Gough, P.S.
 "An Experimental Determination of Flow Resistance in
 Packed Beds of Gun Propellant"
 Proc. 15th Jannaf Combustion Meeting September 1978
49. van der Merwe, D.F. and Gauvin, W.H.
 "Pressure Drag Measurements for Turbulent Air Flow
 Through a Packed Bed"
 A.I.Ch.E.J 1971
50. Denton, W.H.
 "General Discussion on Heat Transfer"
 Inst. Mech. Eng. and Am. Soc. Mech. Eng. 1951
51. Gelperin, N.I. and Einstein, V.G.
 "Heat Transfer in Fluidized Beds"
 Fluidization, edited by J.F. Davidson and D. Harrison
 Academic Press 1971
52. Jakus, K.
 "Study of Flame Spreading Through Single Base Propellant Beds"
 Proc. 11th Jannaf Combustion Meeting 1974
53. Kraiko, A.N. and Sternin, L.E.
 "Theory of Flow of a Two-Velocity Continuous Medium Containing
 Solid or Liquid Particles"
 PMM, v.29, n.3 1965

54. Prandtl, L. and Tietjens, O.G.
"Fundamentals of Hydro- and Aeromechanics"
Dover Publications 1957
55. Kaufmann, W.
"Fluid Mechanics"
McGraw-Hill 1963
56. Shapiro, A.H.
"The Dynamics and Thermodynamics of Compressible Fluid Flow"
Ronald Press 1953
57. Hadley, G.
"Linear Algebra"
Addison-Wesley 1961
58. Courant, R. and Hilbert, D.
"Methods of Mathematical Physics"
Interscience 1953
59. Roache, P.J.
"Computational Fluid Dynamics"
Hermosa Publishers 1972
60. Abbett, M.J.
"Boundary Condition Calculation Procedures for Inviscid Supersonic
Flow Fields"
Proc 1st AIAA Comp. Fluid Dynamics Conference 1973

NOMENCLATURE

Certain symbols are used in different contexts with different meanings. It is not expected that confusion will result as the contexts are very different.

English Symbols

A	Cross sectional area of a quasi-one-dimensional flow
a	Rate of propagation of granular disturbances
a_1	Value of a for settled bed during compression
a_2	Value of a for unloading or reloading bed when porosity is less than settling porosity
B_1	Burn rate additive constant
B_2	Burn rate pre-exponential factor
b	Covolume of gas phase
c	Speed of sound in gas phase
c_v, c_p	Specific heats at constant volume and constant pressure
D_p	Effective diameter of a grain of propellant
\dot{d}	Rate of surface regression of burning propellant
E	Sum of internal and kinetic energies
e	Internal energy of gas phase
e_p	Chemical energy released in combustion of solid phase
F_{RES}	Bore resistance
\vec{f}	Interphase drag
g_0	Constant used to reconcile units of measurement
H	Parameter used to deduce propellant surface temperature by cubic profile method
h	Heat transfer coefficient
I	Polar moment of inertia of projectile
k	Thermal conductivity
M	Projectile Mass
M_{eff}	Effective projectile Mass
\dot{m}	Mass production per unit volume per unit time due to propellant combustion
\dot{m}_i, \dot{m}_o	Mass fluxes to and from a region
\vec{n}	Normal vector
n	Burn rate exponent
Pr	Prandtl number
p	Pressure
q	Heat flux
R	Intergranular stress
Re_p	Reynolds number based on effective particle diameter
R_i, R_o	Radii of surfaces of quasi-one-dimensional axial flow across which mass enters and exits, respectively
r	Radial coordinate
S_p	Surface area of a propellant grain
s_p	Surface area of propellant per unit volume
T	Gas temperature
T_p	Surface temperature of solid phase
t	Time
\vec{u}	Gas velocity vector, components (u, v)

\vec{u}_p	Solid phase velocity vector, components (u_p, v_p)
V_p	Volume of a propellant grain
w, w_p	ζ - component of gas, solid velocity in computational plane
x, x_p	η - component of gas, solid velocity in computational plane
z	Axial coordinate

Greek Symbols

α	Characteristic coordinate
α_p	Thermal diffusivity of a grain
β	Virtual mass coefficient; also characteristic coordinate
γ	Ratio of specific heats
ϵ	Porosity
ϵ_0	Settling porosity
ζ	Computational coordinate
η	Computational coordinate
θ	Angle of rifling of tube
λ	Coefficient used to render balance equations pseudo-totally hyperbolic
μ	Viscosity
ρ	Density of gas
ρ_p	Density of solid propellant, a constant
σ	$(1-\epsilon)R$
τ	Time coordinate in computational frame
ψ	Rate of production of gas per unit volume due to igniter; also used to represent a column vector of state variables

Special symbols and subscripts

D/Dt	Convective derivative along average gas phase streamline
D/Dt_p	Convective derivative along average solid phase streamline
$\dot{}$	A dot over a quantity indicates differentiation with respect to time along a material path line
IG, p	The subscript IG is used to denote properties of the igniter and p is used to denote properties of the solid phase. Gas phase properties are unsubscripted

DISTRIBUTION LIST

<u>No. of</u> <u>Copies</u>	<u>Organization</u>	<u>No. of</u> <u>Copies</u>	<u>Organization</u>
12	Commander Defense Documentation Center ATTN: DDC-DDA Cameron Station Alexandria, VA 22314	1	Director US Army Air Mobility Research and Development Laboratory Ames Research Center Moffett Field, CA 94035
1	Director Defense Advanced Research Projects Agency ATTN: E. F. Blase 1400 Wilson Boulevard Arlington, VA 22209	1	Commander US Army Electronics Research and Development Command Technical Support Activity ATTN: DELSD-L Fort Monmouth, NJ 07703
1	Director Institute for Defense Analyses ATTN: R. C. Oliver 400 Army-Navy Drive Arlington, VA 22202	1	Commander US Army Communications Rsch and Development Command ATTN: DRDCO-PPA-SA Fort Monmouth, NJ 07703
1	Commander US Army Materiel Development and Readiness Command ATTN: DRCDMD-ST 5001 Eisenhower Avenue Alexandria, VA 22333	2	Commander US Army Missile Research and Development Command ATTN: DRDMI-R DRDMI-YDL Redstone Arsenal, AL 35809
1	Commander US Army Materiel Development and Readiness Command ATTN: DRCDE-DW, S.R. Matos 5001 Eisenhower Avenue Alexandria, VA 22333	1	Commander US Army Missile Research and Development Command ATTN: DRDMI-RK, R.G. Rhoades Redstone Arsenal, AL 35809
1	Commander US Army Aviation Research and Development Command ATTN: DRSAV-E P. O. Box 209 St. Louis, MO 63166	1	Commander US Army Tank Automotive Rsch and Development Command ATTN: DRDTA-UL Warren, MI 48090

DISTRIBUTION LIST

<u>No. of</u> <u>Copies</u>	<u>Organization</u>	<u>No. of</u> <u>Copies</u>	<u>Organization</u>
10	Commander US Army Armament R&D Command ATTN: DRDAR-TSS (2 cys) H. Fair E. Wurzel S. Bernstein S. Einstein P. Kemmey DRDAR-LCE, R. Walker DRDAR-LCE, C. Lenchitz DRDAR-SCA, L. Stiefel Dover, NJ 07801	1	Commander US Army Research Office ATTN: Tech Lib P.O. Box 12211 Research Triangle Park, NC 27706
		1	Chief Naval Research ATTN: Code 473, R.S. Miller 800 N. Quincy Street Arlington, VA 22217
1	Commander US Army Materials and Mechanics Research Center ATTN: DRXMR-ATL Watertown, MA 02172	1	Commander US Naval Sea Systems Command ATTN: NAVSEA-0331, J.W. Murrin National Center, Bldg. 2, Rm 6E08 Washington, DC 20360
1	Commander US Army Natick Research and Development Command ATTN: DRXRE, D. Sieling Natick, MA 01762	2	Commander US Naval Surface Weapons Center ATTN: Code G33, J.L. East Code DX-21 Tech Library Dahlgren, VA 22448
1	Commander US Army Armament Materiel Readiness Command ATTN: DRDAR-LEP-L, Tech Lib Rock Island, IL 61299	2	Commander US Naval Surface Weapons Center ATTN: S.J. Jacobs/Code 240 Code 730 Silver Spring, MD 20910
1	Commander US Army Watervliet Arsenal ATTN: SARWV-RD, R. Thierry Watervliet, NY 12189	1	Commanding Officer US Naval Underwater Systems Center Energy Conversion Dept. ATTN: Code 5B331, R.S. Lazar Newport, RI 02840
1	Director US Army TRADOC Systems Analysis Activity ATTN: ATAA-SL, Tech Lib White Sands Missile Range NM 88002	2	Commander US Naval Weapons Center ATTN: Code 388, R.L. Derr C.F. Price China Lake, CA 93555

DISTRIBUTION LIST

<u>No. of</u> <u>Copies</u>	<u>Organization</u>	<u>No. of</u> <u>Copies</u>	<u>Organization</u>
1	Superintendent US Naval Postgraduate School Dept. of Mechanical Engineering ATTN: A.E. Fuhs Monterey, CA 93940	1	Calspan Corporation ATTN: E.B. Fisher P.O. Box 235 Buffalo, NY 14221
2	Commanding Officer US Naval Ordnance Station ATTN: P.L. Stang F.W. Robbins Indian Head, MD 20640	1	ENKI Corporation ATTN: M.I. Madison 9015 Fullbright Avenue Chatsworth, CA 91311
1	AFOSR ATTN: J.F. Masi, NA Bolling Air Force Base Washington, DC 20332	1	Foster Miller Associates, Inc. ATTN: A.J. Erickson 135 Second Avenue Waltham, MA 02154
1	AFATL/DLDDL ATTN: O.K. Heiney Eglin AFB, FL 32542	1	General Applied Sciences Labs ATTN: J. Erdos Merrick & Stewart Avenues Westbury Long Island, NY 11590
2	AFRPL (DYSC) ATTN: D. George J.N. Levine Edwards AFB, CA 93523	1	General Electric Company Armament Systems Dept. ATTN: M.J. Bulman, Rm. 1311 Lakeside Avenue Burlington, VT 05402
1	Aerojet Solid Propulsion Co. ATTN: P. Micheli Sacramento, CA 95813	1	Hercules, Inc. Allegany Ballistics Laboratory ATTN: R.B. Miller P.O. Box 210 Cumberland, MD 21502
1	ARO Incorporated ATTN: N. Dougherty Arnold AFS, TN 37389	1	Hercules, Inc. Bacchus Works ATTN: K.P. McCarty P.O. Box 98 Magna, UT 84044
1	Atlantic Research Corporation ATTN: M.K. King 5390 Cherokee Avenue Alexandria, VA 22314	1	Hercules, Inc. Eglin Operations AFATL/DLDDL ATTN: R.L. Simmons Eglin AFB, FL 32542
1	AVCO Corporation AVCO Everett Rsch Lab Div ATTN: D. Stickler 2385 Revere Beach Parkway Everett, MA 02149		

DISTRIBUTION LIST

<u>No. of</u> <u>Copies</u>	<u>Organization</u>	<u>No. of</u> <u>Copies</u>	<u>Organization</u>
1	IITRI ATTN: M.J. Klein 10 W. 35th Street Chicago, IL 60615	1	Scientific Research Assoc., Inc. ATTN: H. McDonald P.O. Box 498 Glastonbury, CT 06033
1	Lawrence Livermore Laboratory ATTN: M.S. L-355, A. Buckingham P.O. Box 808 Livermore, CA 94550	1	Shock Hydrodynamics, Inc. ATTN: W.H. Anderson 4710-16 Vineland Avenue North Hollywood, CA 91602
1	Olin Corporation Badger Army Ammunition Plant ATTN: R.J. Thiede Baraboo, WI 53913	3	Thiokol Corporation Huntsville Division ATTN: D. Flanigan R. Glick Tech Lib Huntsville, AL 35807
1	Olin Corporation Smokeless Powder Operations ATTN: R.L. Cook P.O. Box 222 St. Marks, FL 32355	2	Thiokol Corporation Wasatch Division ATTN: John Peterson Tech Lib P.O. Box 524 Brigham City, UT 84302
1	Paul Gough Associates, Inc. ATTN: P.S. Gough P.O. Box 1614 Portsmouth, NH 03801	2	United Technology Center ATTN: R. Brown Tech Lib P.O. Box 358 Sunnyvale, CA 94088
1	Physics International Company 2700 Merced Street Leandro, CA 94577	1	Universal Propulsion Company ATTN: H.J. McSpadden P.O. Box 546 Riverside, CA 92502
1	Pulsepower Systems, Inc. ATTN: L.C. Elmore 815 American Street San Carlos, CA 94070	1	Battelle Memorial Institute ATTN: Tech Lib 505 King Avenue Columbus, OH 43201
1	Rockwell International Corp. Rocketdyne Division ATTN: BA08, J.E. Flanagan 6633 Canoga Avenue Canoga Park, CA 91304	1	Brigham Young University Dept of Chemical Engineering ATTN: R. Coates Provo, UT 84601
1	Science Applications, Inc. ATTN: R.B. Edelman 32146 Cumorah Crest Woodland Hills, CA 91364		

DISTRIBUTION LIST

<u>No. of</u> <u>Copies</u>	<u>Organization</u>	<u>No. of</u> <u>Copies</u>	<u>Organization</u>
1	California Institute of Tech 204 Karman Lab Mail Stop 301-46 ATTN: F.E.C. Culick 1201 E. California Street Pasadena, CA 91125	1	Pennsylvania State University Applied Research Lab ATTN: G.M. Faeth P.O. Box 30 State College, PA 16801
1	California Institute of Technology Jet Propulsion Laboratory ATTN: L.D. Strand 4800 Oak Grove Drive Pasadena, CA 91103	1	Pennsylvania State University Dept of Mechanical Engineering ATTN: K. Kuo University Park, PA 16801
1	Case Western Reserve Univ. Division of Aerospace Sciences ATTN: J. Tien Cleveland, OH 44135	1	Princeton University Forrestal Campus Library ATTN: L.H. Caveny P.O. Box 710 Princeton, NJ 08540
3	Georgia Institute of Tech School of Aerospace Eng. ATTN: B.T. Zinn E. Price W.C. Strahle Atlanta, GA 30332	1	Purdue University School of Mechanical Engineering ATTN: J.R. Osborn TSPC Chaffee Hall West Lafayette, IN 47906
1	Institute of Gas Technology ATTN: D. Gidaspow 3424 S. State Street Chicago, IL 60616	1	Rutgers State University Dept of Mechanical and Aerospace Engineering ATTN: S. Temkin University Heights Campus New Brunswick, NJ 08903
1	Johns Hopkins University Applied Physics Laboratory Chemical Propulsion Infor- mation Agency ATTN: T. Christian Johns Hopkins Road Laurel, MD 20810	1	Rensselaer Polytechnic Inst. Department of Mathematics ATTN: Prof. D.A. Drew Troy, NY 12181
1	Massachusetts Institute of Technology Dept of Mechanical Engineering ATTN: T. Toong Cambridge, MA 02139	1	Southwest Research Institute Institute Scientists ATTN: W.H. McLain P.O. Drawer 28510 San Antonio, TX 78228

DISTRIBUTION LIST

<u>No. of</u> <u>Copies</u>	<u>Organization</u>	<u>No. of</u> <u>Copies</u>	<u>Organization</u>
1	SRI International Propulsion Sciences Division ATTN: Tech Lib 333 Ravenswood Avenue Menlo Park, CA 94024	1	University of Massachusetts Dept of Mechanical Engineering ATTN: K. Jakus Amherst, MA 01002
1	Stevens Institute of Technology Davidson Laboratory ATTN: R. McAlevy, III Hoboken, NJ 07030	1	University of Minnesota Dept of Mechanical Engineering ATTN: E. Fletcher Minneapolis, MN 55455
1	University of California Los Alamos Scientific Lab ATTN: T3, D. Butler Los Alamos, NM 87554	2	University of Utah Dept of Chemical Engineering ATTN: A. Baer G. Flandro Salt Lake City, UT 84112
1	University of Southern California Mechanical Engineering Dept. ATTN: OHE200, M. Gerstein Los Angeles, CA 90007	1	Washington State University Dept of Mechanical Engineering ATTN: Prof. C.T. Crowe Pullman, WA 99163
1	University of California, San Diego AMES Department ATTN: F. A. Williams P. O. Box 109 La Jolla, CA 92037		<u>Aberdeen Proving Ground</u> Dir, USAMSAA ATTN: Dr. J. Sperrazza DRXSY-MP, H. Cohen Cdr, USATECOM ATTN: DRSTE-TO-F Dir, Wpns Sys Concepts Team, Bldg. E3516, EA ATTN: DRDAR-ACW
1	University of Illinois AAE Department ATTN: H. Krier Transportation Bldg. Rm 105 Urbana, IL 61801		

USER EVALUATION OF REPORT

Please take a few minutes to answer the questions below; tear out this sheet and return it to Director, US Army Ballistic Research Laboratory, ARRADCOM, ATTN: DRDAR-TSB, Aberdeen Proving Ground, Maryland 21005. Your comments will provide us with information for improving future reports.

1. BRL Report Number _____

2. Does this report satisfy a need? (Comment on purpose, related project, or other area of interest for which report will be used.)

3. How, specifically, is the report being used? (Information source, design data or procedure, management procedure, source of ideas, etc.) _____

4. Has the information in this report led to any quantitative savings as far as man-hours/contract dollars saved, operating costs avoided, efficiencies achieved, etc.? If so, please elaborate.

5. General Comments (Indicate what you think should be changed to make this report and future reports of this type more responsive to your needs, more usable, improve readability, etc.) _____

6. If you would like to be contacted by the personnel who prepared this report to raise specific questions or discuss the topic, please fill in the following information.

Name: _____

Telephone Number: _____

Organization Address: _____

